Gene expression stochasticity, protein synthesis and the ageing process in the budding yeast *Saccharomyces cerevisiae*.

Tailise Carolina de Souza Guerreiro, BSc

A thesis submitted for the degree of
Doctor of Philosophy

School of Life Sciences
University of Warwick

Supervisor: Prof. John E. G. McCarthy

April 2019

Summary

Declaration

I declare that I performed the work submitted in this thesis to the University of Warwick, in support of my application for the degree of Doctor of Philosophy. This work was performed by myself under the supervision of Prof John McCarthy. Where this research was benefited from contribution from others, it is specifically stated in the text.

No part of this work has been submitted in any previous application for a degree. The research presented here was carried out by the author.

To my mom, Elisabeth, my
Grandma Nilce (in memoriam),
and my husband, Fábio

Acknowledgements

First and foremost, I would like to thank God for giving me this opportunity and for helping me achieve this goal (and dream).

I would like to thank my supervisor, Prof. John McCarthy for giving me the opportunity to work in his lab and for his support. I would also like to thank Dr Maja Firczuk, Dr Xiang Meng and Dr Estelle Dacheux for the help, support with my project and friendship! Your help was essential to my project! I am also grateful to my current and former lab colleagues, Fábio, Gurd, Byron, Ollie and Paola, for their help in the lab, with equipment and for the good times!

Also, thanks to Dr. Sarah Bennet, Dr Mehrnaz Shamalnasab, Dr. Graham Jones and Dr. Corinne Hanlon for the helpful discussions and help with WISB facilities.

I would also like to thanks my Advisory panel, Dr Andre Pires da Silva and Prof Alfonso Jaramillo for the help and suggestions during my PhD.

I am also grateful to my husband, Fábio, for his help, support and love. You know this thesis is also yours! Your support, dedication and love were (and are) essential in my life! I am extremely grateful to have you by my side! Love you a lot! Te amo muito!
I am very grateful to my mom, Elisabeth Souza, who loved and supported me my entire life, making it possible for me to be here. You are fundamental in my life and this thesis is also yours! Thank you for being my mother, and doing the job of a mother and father in supporting me. You always push me forwards and your example teaches me the most precious principles in life! Love you very, very much! Te amo muito!
I would also like to thank my aunt Lucy, uncle Jarbas, my uncle Carlos (*in memoriam*) and my grandma Nilce (*in memoriam*) for their love and support! You are amazing and essential in my life! Love you very, very much! Thanks as well to my mother and father in law Márcia and Gisberto! Love you all!

Finally, thanks to University of Warwick, School of Life Sciences, WISB and my funding agency, CAPES - Brazil.

Abstract

Analysis of the biological processes that influence ageing is crucial to developing a full understanding of the mechanisms underpinning it. *Saccharomyces cerevisiae* has been shown to be a key model for ageing research since the pathways for the ageing process are highly conserved between eukaryotes, from yeast to man. Previous reports have demonstrated the role of translational control in life span modulation. Calorie restriction increases life span by a mechanism mediated by Target of Rapamycin (TOR) signalling, which in turn reduces synthesis and activity of ribosome subunits as well as global translation activity. Consistently, a system-level transcriptome and proteome analysis demonstrated that, as the cells age, the proteome increasingly uncouples from the transcriptome, with this protein overrepresentation being linked to ageing. In this study, we have applied an innovative approach combining cell wall staining, flow cytometry and microfluidics, to investigate at a single-cell level whether the noise characteristics of yeast cells change with increasing age and to what extent individual components of the translation machinery contribute to the relationship between ageing and noise. We find that gene expression noise generally increases as cells age, but that deletion of eIF4G1 (translation initiation factor 4G1) both restricts age-dependent increases in noise and extends life span, thus indicating that translation machinery activity and gene expression noise are inversely related to replicative lifespan.

Abbreviations

40S	Small ribosome subunit 40S
5'UTR	5' untranslated region
80S	Small ribosome subunit 80S
A-site	Acceptor site
aa-tRNA	aminoacyl tRNA
ABC	ATP-Binding Cassette
ADP	Adenosine Diphosphate
Akt	Protein kinase B (PKB is also known as Akt)
AMP	Adenosine Monophosphate
AMPK	AMP-activated protein kinase
ATP	Adenosine Triphosphate
bp	Base Pairs
$CaCl_2$	Calcium chloride
CFP	Cyan Fluorescent Protein
CLS	Chronological Lifespan
CV	Coefficient of Variation
dATP	Deoxyadenosine triphosphate
dCTP	Deoxycytidine triphosphate
ddH_2O	Double-distilled water
DDR	DNA damage response
dGTP	Deoxyguanosine triphosphate
DNA	Deoxyribonucleic acid
dNTP	Deoxynucleotide triphosphates
DR	Dietary Restriction
DTT	Dithiothreitol
dTTP	Deoxythymidine triphosphate
E-site	Exit site

EDTA	Ethylenediaminetetraacetic acid
eEF1A	Eukaryotic Translation Elongation Factor 1A
eEF1B	Eukaryotic Translation Elongation Factor 1B
eEF2	Eukaryotic Translation Elongation Factor 2
eEF2K	Eukaryotic Translation Elongation Factor 2 kinase
eEF3	Eukaryotic Translation Elongation Factor 3
eIF	Eukaryotic Translation Initiation Factors
eIF1	Eukaryotic Translation Initiation Factor 1
eIF1A	Eukaryotic Translation Initiation Factor 1A
eIF2	Eukaryotic Translation Initiation Factor 2
eIF2B	Eukaryotic Translation Initiation Factor 2B
eIF3	Eukaryotic Translation Initiation Factor 3
eIF4A	Eukaryotic Translation Initiation Factor 4A
eIF4B	Eukaryotic Translation Initiation Factor 4B
eIF4E	Eukaryotic Translation Initiation Factor 4E
eIF4G	Eukaryotic Translation Initiation Factor 4G
eIF4H	Eukaryotic Translation Initiation Factor H
eIF5	Eukaryotic Translation Initiation Factor 5
eIF5B	Eukaryotic Translation Initiation Factor 5B
eRF1	Eukaryotic Release Factor 1
eRF3	Eukaryotic Release Factor 3
4E-BP	eIF4E-Binding Protein
ERK	Extracellular signal-Regulated Kinases
EtOH	Ethanol
FOXO	Forkhead Box O
FSC	Forward Scatter
g	Gram
GAP	GTPase-activating protein
GDP	Guanosine Diphosphate
GFP	Green Fluorescent Protein
GTP	Guanosine Triphosphate

HIV	Human Immunodeficiency Virus
HSC	Haematopoietic Stem Cells
HSF-1	Heat Shock Factor 1
HSP	Heat Shock Proteins
IGF1	Insulin-like Growth Factor 1
IIS	Insulin and Insulin-like growth factor 1 pathway
IRS	Insulin Receptors
ISC	Intestinal Stem Cells
KCl	Potassium chloride
KH_2PO_4	Potassium dihydrogen phosphate
L	Litre
LB	Lysogeny Broth
LiAc	Lithium Acetate
M	Molar, *i.e.*, mol/L
Met-tRNA	Methionyl transfer RNA
mg	Milligram
Mg^{2+}	Magnesium cation
$MgCl_2$	Magnesium chloride
$MgSO_4$	Magnesium sulphate
mL	Millilitre
mM	Milli molar
Mnk1	Mitogen-activated protein kinase-interacting kinase
mRNA	Messenger Ribonucleic Acid
mRNP	Messenger Ribonucleoprotein
mtDNA	Mitochondrial DNA
mTOR	Mechanistic Target of Rapamycin
Na_2HPO_4	Disodium hydrogen phosphate
NaCl	Sodium chloride
NAD^+	Nicotinamide Adenine Dinucleotide
ng	Nanogram
nm	Nanometre

NSC	Neural Stem Cells
°C	Degree Celsius
OD_{600}	Optical Density at 600 nm
ORF	Open-Reading-Frame
P-site	Peptidyl site
PABP	Poly(A) Binding Protein
PBS	Phosphate Buffer Saline
PCR	Polymerase chain reaction
PDMS	Polydimethylsiloxane
PEG8000	Polyethylene glycol 8000
pH	$\log_{10}[H^+]$
Pi	Inorganic phosphate
PI3K	Phosphatidylinositol 3 kinase
PIC	Pre-initiation Complex
PIP2	Phosphatidylinositol (4,5)-bisphosphate
PIP3	Phosphatidylinositol (1,4,5)-trisphosphate
PKA	Protein Kinase A
PTC	Peptidyl Transferase Centre
RF	Radio frequency
RLS	Replicative Lifespan
RNA	Ribonucleic Acid
ROS	Reactive Oxygen Species
rpm	Rotations per minute
rRNA	Ribosomal Ribonucleic Acid
S6K	S6 protein kinase
S6K1	S6 protein kinase 1
S6K2	S6 protein kinase 2
SD	Standard Deviation
SDS	Sodium Dodecyl Sulphate
SOC	Super Optimal broth with Catabolite repression
SSC	Side Scatter

TAE	Tris-acetate-EDTA
TBE	Tris-borate-EDTA
TE	Tris-EDTA buffer
Tris-HCl	Tris(hydroxymethyl)aminomethane Hydrochloride
tRNA	Transfer RNA
UPS	Ubiquitin-Proteasome System
UTR	RNA Untranslated Region
UV	Ultra violet
V	Volts
V	Volume
v/v	Volume by volume
w/v	Weight by volume
WGA	Wheat Germ Agglutinin
YFP	Yellow Fluorescent Protein
YPD	Yeast extract Peptone Dextrose
µg	Microgram
µL	Micro litre
µM	Micro molar
µm	Micrometre
yEGFP	Yeast-enhanced green fluorescent protein
HYAA	High-throughput Yeast Ageing Analysis
CLiC	Cell Loaded into a Cavity
psi	Pounds per square inch
CTCF	Corrected Total Cell Fluorescence
NHS	N-Hydroxy-Succinamide
FACS	Fluorescence-Activated Cell Sorting
PMT	Photomultiplier
a.u.	Arbitrary units
ANOVA	Analysis of variance
λ_{ex}	Excitation wavelength

List of Figures

List of Tables

Chapter 1 - Introduction

1.1. Translation – a vital biological process

Translation is an essential biological process in which information contained in a messenger ribonucleic acid (mRNA) molecule is decoded into a specific amino acid sequence that then folds to form an active protein. Translation can be divided into four phases: initiation, elongation, termination, and recycling (reviewed in Kapp and Lorsch, 2004). Consuming up to 75% of cellular energy (Lane and Martin, 2010), translation is a crucial process for life, and therefore the component phases are conserved between all kingdoms of life. However, the mechanisms underpinning of each phase can vary from kingdom to kingdom (Kapp and Lorsch, 2004). The first phase, initiation, is the part of the translation cycle that is most subjected to regulation (Sonenberg and Hinnebusch, 2009) and is facilitated by a set of translation initiation factors. In this phase, the ribosomal subunits and initiation factors promote recognition of the mRNA start codon, whereby a methionyl transfer RNA (Met-tRNA) becomes localised at the peptidyl site (P-site), forming an elongation-competent 80S (reviewed in Kapp and Lorsch, 2004 and Aitken and Lorsch, 2012). Once the small and large ribosomal subunits have been assembled at the start codon, elongation starts. An aminoacyl tRNA (aa-tRNA) enters the ribosome through the acceptor site (A-site) and if it is correct (cognate), the ribosome catalyses the formation of a peptide bond between the incoming amino acid and the polypeptide chain. After that, translocation takes place and tRNA and mRNA are moved so that the ribosome A-site is placed on the next codon. This phase is facilitated by elongation factors. The process is repeated until a stop codon is found, which triggers termination. Release factors decode the stop codon and help the peptide sequence to be released from the ribosome. The last phase is recycling, when the ribosome subunits are disassembled, mRNA and deacylated tRNA are released, and another round of translation can start (reviewed in Kapp and Lorsch, 2004).

Translation in eukaryotes

1.1.1. Initiation

Initiation is a complex process that comprises many steps, requiring at least 12 eukaryotic translation initiation factors (eIF) (Jackson et al, 2010; Aitken and Lorsch, 2012), orchestrated to assemble the elongation-competent 80S ribosome. A critical step of initiation is ternary complex formation, with the association of eIF2-GTP with Met-tRNA. Prior to this step, an important reaction must have occurred yet in the recycling phase, to convert eIF2-GDP, resulting from a previous round of translation initiation, to eIF2-GTP. eIF2 has significantly higher (100 fold) affinity for GDP than for GTP, so, to be ready for the ternary complex assembly, eIF2-GDP must be recycled to eIF2-GTP by the action of eIF2B. Then, eIF2-GTP binds to the Met-tRNA and a functional ternary complex is formed (reviewed in Kapp and Lorsch, 2004). eIF2 is a heterotrimer formed by α, β and γ subunits, recognizing initiator tRNA structures (Kolitz and Lorsch 2010). The γ subunit binds to both GTP and tRNA and the α and β subunits stabilize the interaction with tRNA (Naveau et al, 2010). Phosphorylation of the α subunit induces a stable interaction with eIF2B, decreasing the rate of GDP-GTP exchange and, consequently, decreasing ternary complex formation and all the downstream assembly processes, providing a regulatory step for translation initiation (Sonenberg and Hinnebusch, 2009).

Under participation of the initiation factors eIF1, 1A, 3 and 5, the ternary complex binds to the 40S ribosomal subunit, resulting in the pre-initiation complex (PIC), also called the 43S complex. eIF1 and eIF1A have an important role in PIC assembly, stabilising an open conformation of the 40S subunit, enabling ternary complex binding (Algire et al, 2002) and later playing a role in the AUG scanning process, otherwise impaired by the absence of these factors (Pestova et al, 1998). eIF3 also plays an important role in ternary complex binding to the 40S ribosomal subunit (Majumdar et al 2003).

Figure 1 shows a schematic of PIC assembly (adapted from Aitken and Lorsch, 2012).

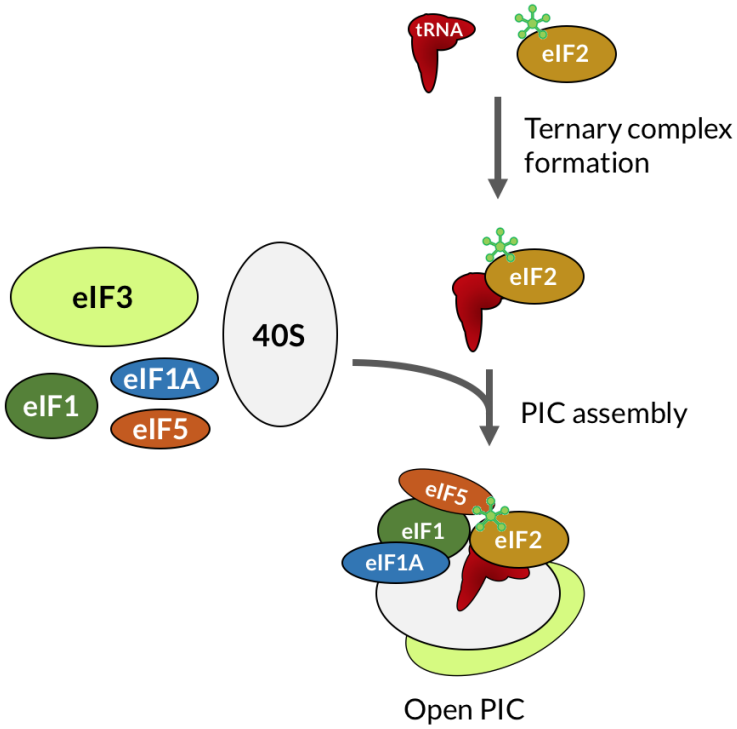

Figure 1: Schematic of pre-initiation complex (PIC) assembly (adapted from Aitken and Lorsch, 2012). eIF2-GTP (represented with a green asterisk) binds to the initiator tRNA to form the ternary complex. With the assistance of the initiation factors eIF1, 1A, 3 and 5, the ternary complex binds to the 40S ribosomal subunit, resulting in the pre-initiation complex (PIC).

In cap-dependent translation, eIF4E binds to the 5'cap of mRNA (7-methylguanosine coupled to mRNA in a 5'-5' triphosphate linkage). The RNA-dependent ATPase eIF4A binds to the mRNA 5' untranslated region (5'UTR) and it is proposed that this initiation factor will act as an RNA helicase to unwind secondary and tertiary structures found near the mRNA 5'cap (Linder, 1992). The RNA binding protein eIF4B is believed to help eIF4A in unwinding these structures (Altmann et al, 1993). Mammals also have eIF4H, another RNA binding protein that plays a similar role to eIF4B in helping the helicase activity of eIF4A (Richter-Cook et al, 1998). The initiation factor Ded1 also has helicase activity, playing a very important role in yeast (Berthelot et al, 2004), substituting eIF4A in the helicase function and

being required for the translation of all mRNAs in this organism (Iost et al., 1999). For more stable secondary structures in the 5'UTR that cannot be removed by eIF4A, mammals have another helicase protein, Dhx29, that is capable of unwinding these structures (Pisareva et al, 2008).

At the 3' end of mRNA, the poly(A) binding protein (PABP) binds to the poly(A) tail and, with the help of eIF4E and eIF4G, the mRNA is circularised (Wells et at, 1998) and loaded into the PIC complex. This closed-loop mRNP is believed to facilitate mRNA loading into the PIC and also to promote another round of translation once translation and recycling are finished (Uchida et al, 2002). eIF4G also interacts with eIF4E, having a scaffolding role. The association of eIF4E, eIF4A, and eIF4G is known as the eIF4F complex (reviewed in Kapp and Lorsch, 2004).

Figure 2 shows a schematic of mRNP activation (adapted from Aitken and Lorsch, 2012).

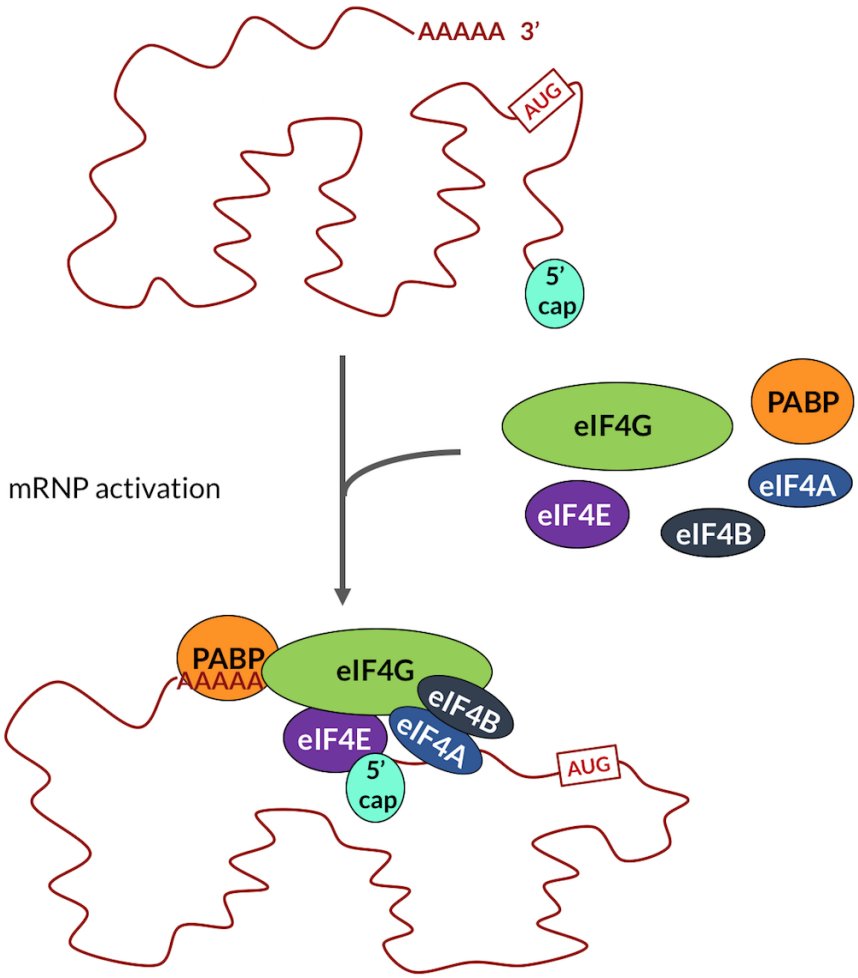

Figure 2: Schematic mRNP activation (adapted from Aitken and Lorsch, 2012). eIF4 factors and PABP bind to the mRNA to form a closed-loop mRNP.

In mammals, there is an interaction between eIF4G and eIF3, and it is thought that this interaction recruits the activated mRNP to the PIC (LeFebvre, 2006). It was shown in yeast that eIF5 interacts with both eIF3 and eIF4G, and it is possible that it might thereby be responsible for bringing the mRNP and PIC together (Asano et al, 2001). eIF4B in both mammals and yeast interacts with eIF3 (Méthot et al, 1996) and thus, eIF3 may play an additional role in loading mRNA onto the PIC in both systems.

mRNA scanning starts in the 5' - 3' direction, looking for the start codon (AUG), with eIF1 and eIF1A also playing a role in this process. Once the start codon is found, codon-anticodon base pairing occurs between the start codon and the initiator

tRNA and eIF1 will leave the complex, inducing PIC closure and promoting GTP hydrolysis by eIF2. eIF5, a GTPase-activating protein (GAP) also plays a role in helping eIF2 catalyze GTP hydrolysis. This releases the Met-tRNA into the P site. Then eIF2 and eIF5 leave the complex. eIF5B-GTP joins the complex at this point, and together with eIF1A, is thought to facilitate 60S subunit joining to the 48S complex accompanied by GTP hydrolysis. Finally, eIF5B-GDP and eIF1A dissociate from the ribosome and the 80S initiation complex is formed. eIF3 may participate in reinitiation events (reviewed in Kapp and Lorsch, 2004 and Aitken and Lorsch, 2012).

Although it is widely accepted that eIF5 plays a role only in the initiation phase of translation, recent studies have demonstrated that eIF5 might play a role in elongation as well. Genetic analysis performed by Saini et al. (2009) and Dias et al. (2012) have shown functional interactions between eIF5 and eEF2. Saini (Saini et al., 2009) and Gregio (Gregio et al., 2009) have also demonstrated that inactivation of eIF5 in yeast causes longer ribosomal transit periods. These data point to a role of eIF5 during elongation, in addition to its role during initiation, although more studies are necessary to confirm this new role of eIF5 in protein synthesis (reviewed in Dever and Green, 2012).

Figure 3 shows a schematic of mRNA loading onto the PIC, scanning and ribosome subunit joining (adapted from Aitken and Lorsch, 2012).

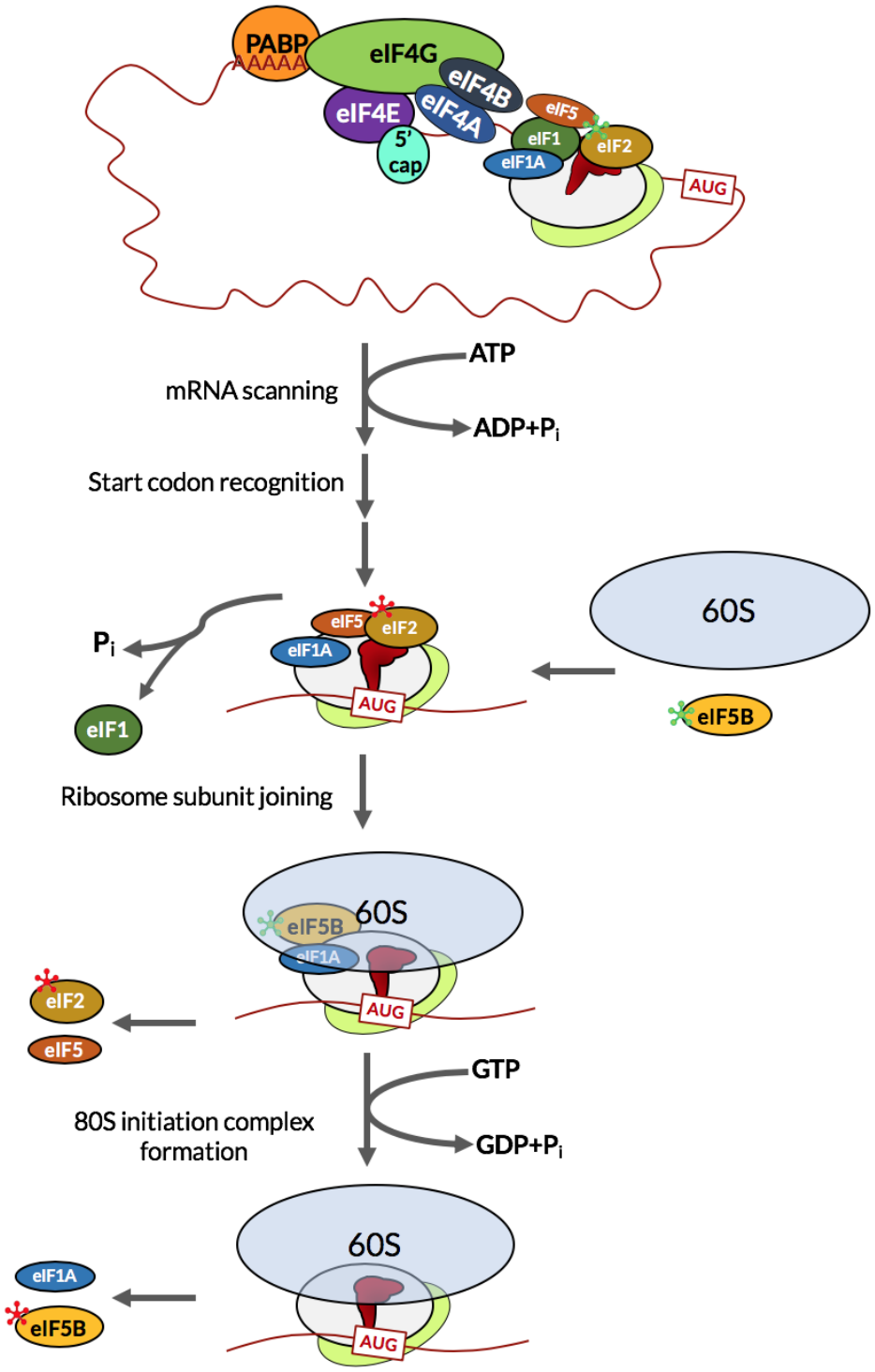

Figure 3: Schematic of mRNA loading onto the PIC, scanning and 80S initiation complex formation (adapted from Aitken and Lorsch, 2012). The mRNP is recruited to the PIC and the scanning process starts. Recognition of the start codon (AUG) triggers eIF1 release, inducing PIC closure and promoting GTP hydrolysis by eIF2. eIF2-GDP and eIF5 dissociate from the complex. eIF5B mediates the joining of the 60S subunit by GTP hydrolysis, and then leaves the assembled 80S initiation complex.

1.1.2. Elongation

Once the 40S and 60S subunits are assembled together and the initiation tRNA is located at the P site of the ribosome, the elongation process begins. The acceptor (A) site contains the subsequent codon of the open-reading-frame (ORF) and receives aminoacyl-tRNAs until the cognate one is found. Delivery of aa-tRNA to the A site of the ribosome requires the elongation factor eEF1A, which binds to the aa-tRNA in a GTP-dependent manner, forming a ternary complex. eEF1A-GTP-aa-tRNA carries different amino acids to the A site, and once cognate aa-tRNA binding takes place, codon-anticodon base pairing occurs, triggering GTP hydrolysis by eEF1A. This releases the aa-tRNA into the A-site and eEF1A dissociates to undergo recycling from eEF1A-GDP to eEF1A-GTP with the assistance of eEF1B (reviewed in Kapp and Lorsch, 2004 and Dever and Green, 2012). Once an aa-tRNA has been released into the A-site, peptide bond formation with peptidyl-tRNA (located on the P-site) occurs. The peptidyl transferase centre (PTC) positions the substrates for catalysis. The PTC is formed by conserved rRNA sequences and is located in the large ribosomal subunit. Recent studies demonstrate that PTC rRNA structures are conserved between eukaryotes and bacteria (Ben-Shem et al., 2011 and Klinge et al. 2011, reviewed in Dever and Green, 2012). After peptide bond formation, deacylated tRNA is in a hybrid position between the P site and the E site and peptidyl-tRNA is in a hybrid position between A site and P site, with acceptor ends located in the P and E sites and anticodon loops located in the A and P sites, respectively. The elongation factor eEF2 assists on the translocation of these tRNAs by GTP hydrolysis and Pi release, which is considered to unlock the ribosome so that both transfer and messenger RNA can move. In addition to that, eEF2 has in its domain IV a region that can mimic the anticodon loop of tRNA, which can be inserted into the decoding site, what also promotes translocation. After GTP hydrolysis, eEF2 is released. In the post-translocation state, the subsequent codon is located in the A-site, which is now free to receive the next aa-tRNAs. The deacylated tRNA is located in the E-site and peptidyl-tRNA is located in the P-site.

Chen et al. (2011) have demonstrated that, in initial elongation cycles, deacylated tRNA release from the E-site occurs allosterically upon aminoacyl-tRNA binding to the A-site, but at later cycles of protein elongation, deacylated tRNA dissociates from the E-site spontaneously. The elongation process is repeated until a stop codon is reached (reviewed in Dever and Green, 2012).

Apart from eEF1A, eEF1B, and eEF2, yeast also has the elongation factor eEF3, which helps on aa-tRNA entry through A site and also on deacylated tRNA exit. In humans, the ribosome can perform this function (Kapp and Lorsch, 2004).

The elongation factor eEF2 undergoes posttranslational modifications. On domain IV of eEF2, a conserved histidine residue is modified to diphthamide (His699 in the yeast factor). Ortiz et al. demonstrated in 2006 that an eEF2-H699N mutant strain, which does not have diphthamide, display -1 ribosomal frameshifting, indicating that diphthamide modification plays a role in translation. Other studies (Liu et al. 2006, Webb et al. 2008) have demonstrated that diphthamide is essential for normal development. However, diphthamide is also the target for diphtheria toxin, which promotes its ADP-ribosylation, inactivating eEF2 and blocking translation. In mammalian cells, eEF2 can also be phosphorylated by the protein kinase eEF2K, which can impair translation by preventing the binding of eEF2 binding to the ribosome (reviewed in Dever and Green, 2012).

Figure 4 illustrates the steps of the eukaryotic elongation pathway (adapted from Dever and Green, 2012).

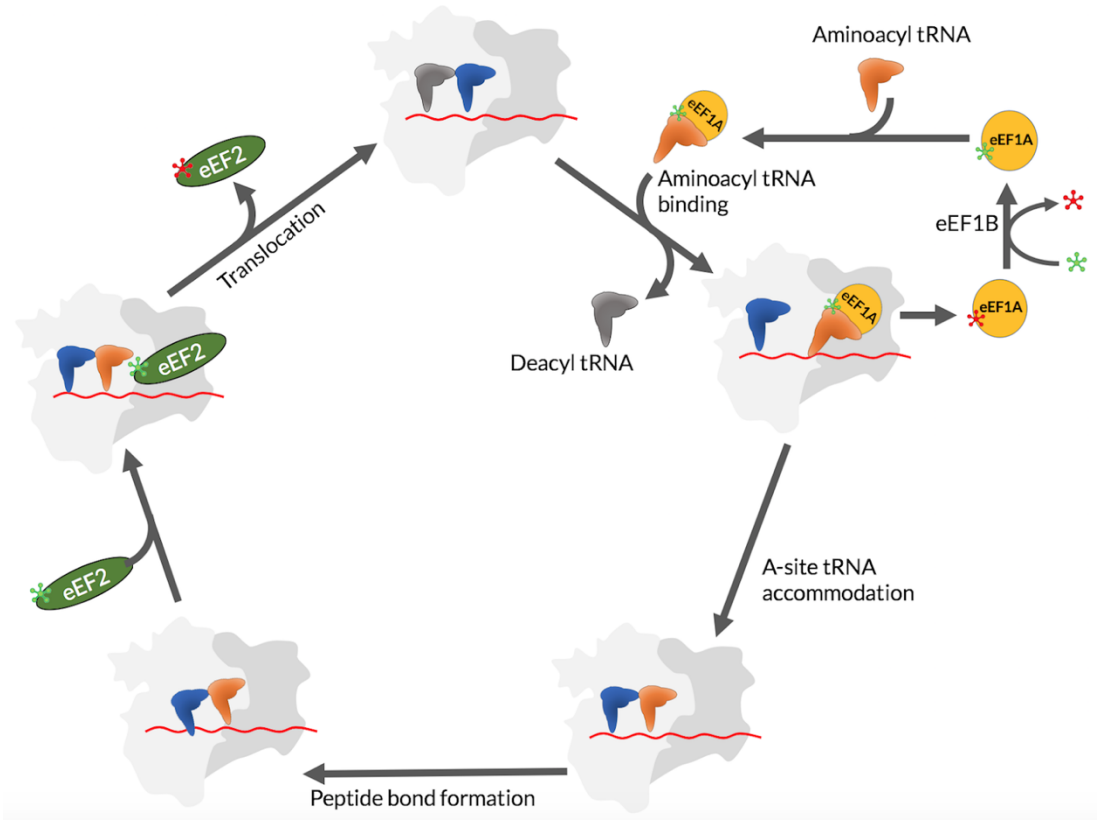

Figure 4: Steps of the eukaryotic elongation pathway (adapted from Dever and Green, 2012). Ribosome subunits are now represented by light and darker grey shapes. The beginning of the elongation cycle is represented at the top, with a ternary complex (eEF1A-GTP-aa-tRNA) binding to the 80S ribosome. After GTP-hydrolysis, the aminoacyl-tRNA is released and accommodated into the A-site, and eEF1A-GDP (represented with a red asterisk) is recycled to eEF1A-GTP (represented with a green asterisk) by the action of the exchange factor eEF1B. Following peptide bond formation, eEF2-GTP (represented with a green asterisk) joins the complex and promotes translocation. eEF2-GDP (represented with a red asterisk) is released and, unlike eEF1A, it does not require an exchange factor. With the release of the deacetylated tRNA, the ribosome is now ready to start the next cycle of elongation.

1.1.3. Termination

Once a stop codon (UAA, UGA or UAG) enters the A-site, elongation is completed the and termination process begins. Eukaryotes have two release factors, eRF1 and eRF3, which are class I and class II factors, respectively. The class I factor is responsible for high fidelity stop codon decoding and also for hydrolysing the ester bond between the polypeptide chain and tRNA located in the P site. This action

needs assistance from eRF3, since eRF1 has no GTP binding motifs (Zhouravleva et al., 1995). The class II factor eRF3 is a translational GTPase, assisting with both polypeptide chain release and termination efficiency (Eyler and Green, 2011, reviewed in Dever and Green, 2012).

eRF1 has a tRNA shape and is composed of three domains, N, M, and C. The N-terminal domain has the conserved NIKS and YxCxxxF motifs, which are involved in stop codon recognition (Chavatte et al., 2002; Kolosov et al., 2005). The M domain has a similar function as the tRNA acceptor stem and can enter the PTC to assist polypeptide chain release (Song et al., 2000). This domain has the highly conserved GGQ motif, that is considered to be involved in the chemistry of peptide hydrolysis (Frolova et al., 1999). The eRF1 C domain interacts with eRF3, forming a ternary complex with GTP and the ribosome, promoting GTP hydrolysis (Frolova et al., 1996), and eRF1 M domain entry on the peptidyl transferase centre, which allows stop codon decoding and polypeptide chain release (reviewed in Dever and Green, 2012). eRF1 and eRF3 also play a role in recycling.

1.1.4. Recycling

Although recycling is well understood in prokaryotes, the recycling process and factors encoded by bacteria are not conserved and eukaryotes do not have homologs of ribosome recycling factors (RRF) (reviewed in Dever and Green, 2012). Initially, it was proposed by Pisarev and colleagues (Pisarev et al., 2007) that initiation factors eIF1, eIF1A and eIF3, especially eIF3j, an associated subunit of eIF3, promote dissociation of post-termination ribosomes. However, it was later proposed (Pisarev et al., 2010) that a member of the ATP-binding cassette (ABC) protein family, ABCE1 (Ril1 in yeast), promotes ribosome dissociation in the presence of eRF1 in a wider range of Mg^{2+}, compared to the previous model. Other studies also demonstrated the role of ABCE1/Ril1 in recycling. Shoemaker and Green (Shoemaker and Green, 2011) proposed a kinetic model for translation

termination and recycling, involving eRF1 and eRF3 and also two other related factors, Dom34 (yeast)/Pelota (mammals) and Hbs1. Dom34 and Hbs1 have significant structural similarity to eRF1 and eRF3, respectively (Shoemaker and Green, 2011), but Dom34 lacks both the NIKS motif in the N domain (stop codon recognition) and GGQ motif in the M domain (peptide release) (Dever and Green, 2012). In Shoemaker and Green's kinetic model, the first step is eRF1:eRF3 or Dom34:Hbs1 binding to the A-site of the ribosome. In the case of eRF1:eRF3, stop codon recognition promotes GTP hydrolysis. Then, eRF3 or Hbs1 in a GDP bound state leaves the complex, followed by accommodation of eRF1 or Dom34 in the active site. As described before (p11), only eRF1 has the GGQ motif to promote peptide release, which occurs with the support of Ril1 in an ATP-independent manner, after accommodation. Ril1 action at this point locks eRF1 or Dom34 in an accommodated state on the ribosome before ATP hydrolysis occurs. After peptide release, this complex can initiate recycling, in which Ril1 and eRF1 (or Dom34) promote ribosome disassembly in an ATP-dependent manner.

The Hbs1 N-terminus interacts with the mRNA entry site, most likely surveilling the 3' region mRNA prior to GTP hydrolysis. In a similar manner, eRF3 interacts with PABP via its N terminus, which might be involved in identifying authentic stop codons, modulating eRF3 activity. After ribosome disassembly, the subunits are captured by interaction with initiation factors including eIF1, eIF1A and eIF3 and another cycle of translation can begin (Shoemaker and Green, 2011).

Figure 5 illustrates the steps of the eukaryotic translation termination and recycling pathways (adapted from Dever and Green, 2012).

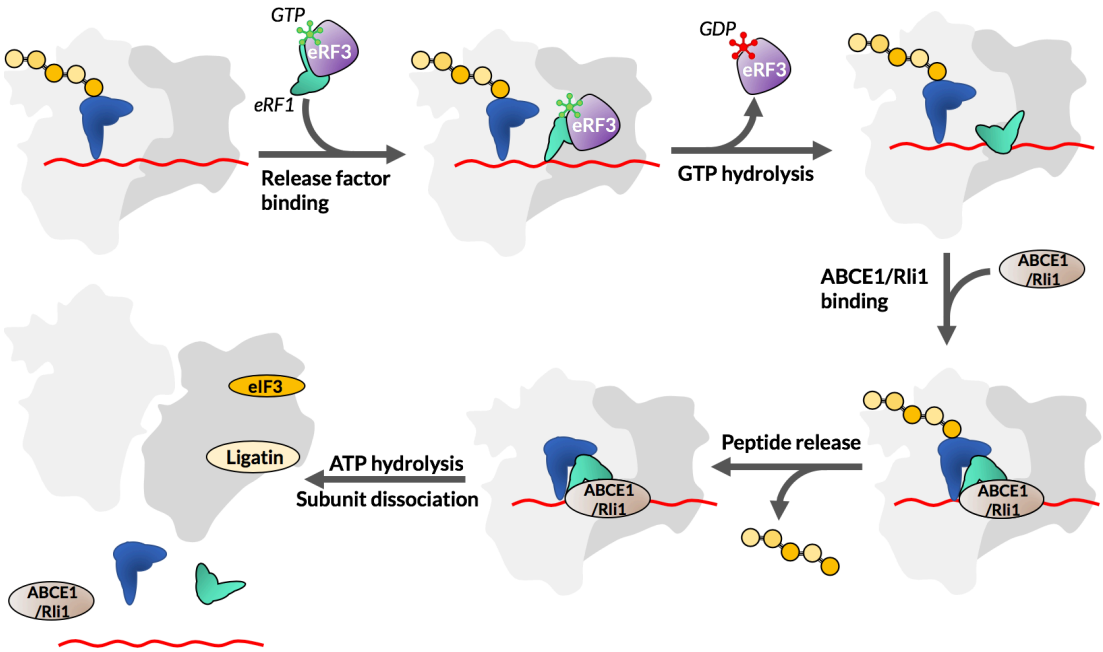

Figure 5: Steps of the eukaryotic translation termination and recycling pathways (adapted from Dever and Green, 2012). Ribosomal subunits are represented in grey. Once a stop codon is found, eRF1:eRF3-GTP (represented with a green asterisk) binds to the A site of the ribosome and promotes GTP hydrolysis, releasing eRF3-GDP (represented with a red asterisk) from the complex. ABCE1/Rli1 binds and assists the accommodation of eRF1 into the ribosome and peptide release occurs. This initiates recycling and Ril1 and eRF1 (or Dom34) promote ribosome disassembly in an ATP-dependent manner.

1.2. Ageing

1.2.1. Overview

Ageing is a time-dependent biological process characterised by the progressive loss of cellular function. Accumulation of cellular damage over time is considered to cause ageing, especially the accumulation of genetic damage and defective proteins (reviewed in López-Otín et al., 2013). Studies in *Saccharomyces cerevisiae* (budding yeast), *Caenorhabditis elegans* (nematode worm), *Drosophila melanogaster* (fruit fly) and mice have generated understanding about the molecular basis of the ageing process and have demonstrated that the majority of ageing pathways were conserved through evolution (reviewed in Gems and Partridge, 2013).

López-Otín et al., (2013) defined, in their review, nine hallmarks of ageing, which are: genomic instability, telomere attrition, epigenetic alterations, deregulated nutrient sensing, mitochondrial dysfunction, cellular senescence, stem cell exhaustion, altered intracellular communication and loss of proteostasis.

Figure 6 illustrates these features (adapted from López-Otín et al., 2013).

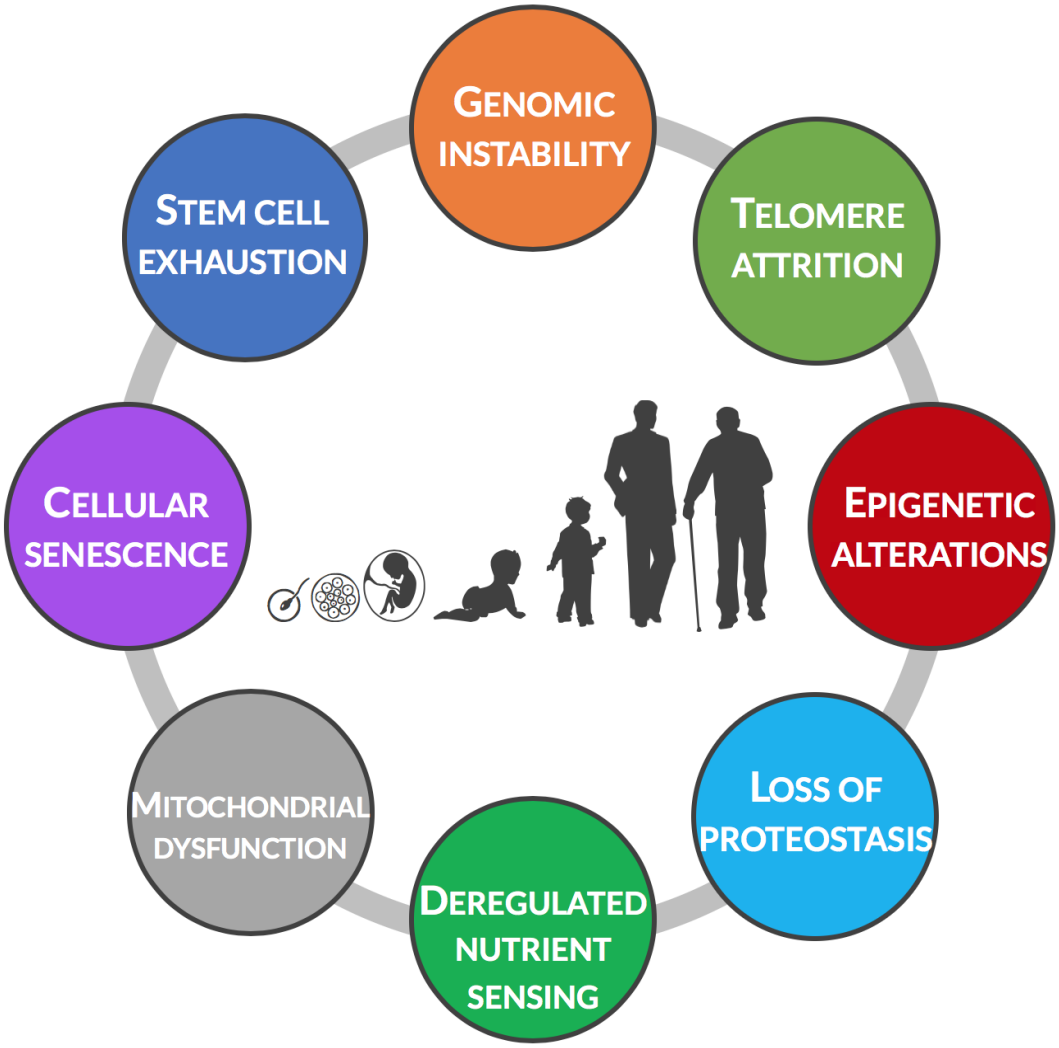

Figure 6: Nine hallmarks of ageing (adapted from López-Otín et al., 2013). This illustration shows the nine manifestations of the ageing process, which are: genomic instability, telomere attrition, epigenetic alterations, deregulated nutrient sensing, mitochondrial dysfunction, cellular senescence, stem cell exhaustion, altered intracellular communication and loss of proteostasis.

Genome stability

The DNA molecule relies only on repair mechanisms and is not remanufactured; therefore, genomic damage can accumulate during life, being caused by endogenous or exogenous factors (Hoejimakers, 2009). Endogenous threats include DNA replication errors and reactive oxygen species (ROS); exogenous threats include UV radiation and chemicals. Although organisms do have DNA repair mechanisms to minimize lesions, the genome is still constantly damaged and during the course of a lifetime, this instability can lead to ageing and/or cancer. When genome maintenance is compromised, the ageing process is accelerated (Hoejimakers, 2009). Premature ageing diseases like Werner syndrome and Bloom syndrome are caused by the accumulation of DNA damage. Genetic lesions can include translocation, point mutations, chromosomal aneuploidy, telomere shortening and gene disruption caused by integration of virus or transposon DNA. Those DNA alterations can affect gene expression and lead to dysfunctional cells that, if not eliminated, can compromise stem cell competence and their role in tissue renewal (reviewed in López-Otín et al., 2013). Experimental evidence supporting the importance of DNA integrity for ageing is provided by Baker et al, 2013, in a study showing that transgenic mice overexpressing BubR1 have increased lifespan and reduced risk for aneuploidy and cancer. BubR1 acts promoting correct mitotic checkpoint and microtubule-kinetochore attachment.

Mitochondrial DNA has an enhanced risk of mutation and the accumulation of lesions can also impact ageing. The mtDNA repair mechanism is less efficient than that for nuclear DNA, and there are no protective histones; this, associated with the small size of the mitochondrial genome, can increase the mutation rate (Linnane et al., 1989). A work published by Vermulst et al. (2008) have demonstrated that mutant mice having a proofreading-deficiency in the mitochondrial polymerase gamma show accelerated signs of ageing, with mtDNA deletions accumulating at a higher rate in the brain and the heart, organs strongly associated with ageing-related diseases.

The nuclear lamina is also related to genome stability. A very important component of the lamina, the A-type lamins, provide structural support and a scaffold for proteins involved in genome maintenance (reviewed in López-Otín et al., 2013). Gonzalez-Suarez et al. (2009) have demonstrated that A-type lamins are involved in telomere maintenance, the DNA damage response (DDR) and genomic stability. Loss of A-type lamins induces telomere shortening and increases the DNA damage rate. Mutations in the *LMNA* gene are also involved in progeria syndromes, like Hutchinson-Gilford (Gonzalez-Suarez et al., 2009), which is characterized by accelerated ageing of children.

Telomere attrition

Another important hallmark of ageing is telomere attrition. Every time cells replicate, DNA is replicated, but DNA polymerase does not have the capacity to replicate the terminal ends of the DNA molecule. Therefore, every cell division results in shortened telomeres. Telomerases are enzymes responsible for the maintenance of telomere length, but they are not expressed in the majority of mammalian somatic cells, which leads to cumulative telomere erosion (López-Otín et al., 2013). Sahin et al. (2010) reviewed the consequences of telomere attrition, which involves stem cell depletion and tissue/organ failure. Jaskelioff et al. (2011) demonstrated that expression of TERT, the catalytic subunit of telomerase, in adult mice with telomere dysfunction, reversed multi-system degeneration. Reactivation of telomerase activity extended telomeres and eliminated degenerative phenotypes in organs including testicles, spleen, and intestines.

Epigenetic alterations

Epigenetic alterations affect ageing as well and include posttranslational modification of histones, changes in DNA methylation and chromatin remodelling. Manipulation of histone-modifying enzymes can influence lifespan, *e.g.* deletion of components of histone methylation complexes extends longevity in nematodes and flies. Additionally, inhibition of the histone demethylase UTX-1 increases lifespan in

worms by affecting the insulin/IGF-1 signalling pathway (Jin et al., 2011). Sirtuins, belonging to the class III histone deacetylases family (Fiorino et al., 2014), can also influence lifespan. Although there has been some controversy about sirtuins truly extending lifespan in different organisms, a recent study performed by Kanfi et al., (2012) demonstrated that transgenic mice overexpressing SIRT6 have longer lifespan, reduced levels of insulin-like growth factor 1 (IGF1), higher levels of IGF-binding protein 1, and altered phosphorylation patterns in IGF1 signalling. The correlation between DNA methylation and ageing is complex and is represented by disbalance: generally, hypomethylation occurs, although loci corresponding to tumour suppressor genes become hypermethylated during ageing (Maegawa et al., 2010; López-Otín et al., 2013). Chromatin remodelling can also be affected by ageing. Chromosomal proteins like heterochromatin protein 1α (HP1 α) and chromatin remodelling factors like Polycomb group proteins have decreased levels in both naturally and pathologically aged cells (reviewed in López-Otín et al., 2013). A study performed by Larson et al. (2012) demonstrated that flies with HP1 α mutations have shortened lifespans and increased rRNA transcription, but when flies had overexpression of HP1 α longer lifespan and reduced rRNA transcription were observed.

Nutrient sensing

Nutrient sensing is very important for organisms and its deregulation is a manifestation of ageing. Nutrient-responsive pathways are very well conserved among organisms, with emphasis for the insulin and insulin-like growth factor 1 (IGF1) pathway (IIS pathway), the most conserved ageing-controlling pathway during evolution (López-Otín et al., 2013). Other nutrient-responsive pathways also affect ageing, including the mTOR pathway, responding to high concentration of amino acids in the cell (representing high energy availability); AMP-activated protein kinase (AMPK), responding to increased concentrations of AMP in the cell (representing low energy levels); and sirtuins, responding to high NAD^+ concentration (representing low energy levels). For multicellular eukaryotes, the IIS

pathway is upstream in the nutrient-sensing pathway. Downregulation of pathways sensing high energy levels and upregulation of pathways sensing low energy levels increases lifespan or healthspan (reviewed in Janssens and Veenhoff, 2016). Consistent with that is the fact that dietary restriction (DR) increases lifespan or healthspan in all eukaryotes investigated, from yeast to primates (López-Otín et al., 2013). As reviewed in Fontana et al. (2010), DR and reduced growth factor signalling can increase oxidative stress resistance, decrease molecular damage and increase longevity from yeast to mammals. In rodents, DR can reduce cognitive decline and the incidence of tumours. In humans, DR and reduced growth factor signalling can decrease the incidence of cancer, diabetes and cardiovascular disease (Fontana et al., 2010). Downstream intracellular effectors mediate increased lifespan effects of dietary restriction in different organisms, and they include PKA, AKT, mTOR, and FOXO. Mutations and polymorphisms decreasing the activity of IGF-1 receptor, insulin receptor or the downstream intracellular effectors were related to increased lifespan in both humans and model organisms (Kenyon, 2010; Kenyon, 2011, Fontana et al., 2010). The mTOR kinase comprises the by mTORC1 and mTORC2 multiprotein complexes. mTORC1 is the main component of mTOR that influences ageing. Genetic downregulation of mTORC1 in yeast, worms, and flies increases lifespan. Interestingly, dietary restriction does not further increase lifespan in those mutants, indicating that mTOR downregulation phenocopies the effects of dietary restriction (López-Otín et al., 2013). A study performed by Yang et al., (2012) has demonstrated that there is an age-related increase in mTOR activity in the mice hypothalamus, which was contributing to obesity. The application of intracerebral rapamycin, an inhibitor of the mTOR pathway, resulted in increased excitability of neurons in the hypothalamus and reduction of food intake, with consequent weight loss. Although downregulation of mTOR generally benefits longevity and healthspan, Wilkinson et al., (2012) have demonstrated that rapamycin administration to mice resulted in increased cataract severity and testicular degeneration, albeit beneficial results were also observed in this study. Sirtuins and AMPK sense low nutrient levels. Sirtuins are responsive to high levels of NAD^+ and the beneficial effects of its activation were discussed before in this chapter (p17).

AMPK activation affects metabolism and induces autophagy, also downregulating mTORC1 (Alers et al., 2012). There are indications that AMPK activation might be involved in the increased longevity seen in worms and mice after administration of metformin (Onken and Driscoll, 2010; Anisimov et al., 2011; López-Otín et al., 2013).

Mitochondrial dysfunction

Mitochondrial dysfunction can be caused by the accumulation of mutations and deletions in mtDNA (as discussed before in this chapter – p15), accumulation of damaged proteins, defects in the respiratory chain complexes, defective mitophagy (which targets deficient mitochondria to proteolytic degradation), changes in the mitochondrial membrane lipid composition, among others. Dysfunctional mitochondria can impact ageing independently of increases in reactive oxygen species, affecting apoptotic signalling and triggering inflammatory reactions (López-Otín et al., 2013). The modified bioenergetic properties of mitochondria observed in ageing can be the result of reduced mitochondrial biogenesis. Telomere attrition can play a role in this reduced biogenesis since telomerase-deficient mice exhibit increased p53 (a senescence implementing pathway) activity, which in turn represses PGC-1 α and PGC-1 β, transcriptional coregulators that control the expression of genes involved in mitochondrial biogenesis. Therefore, this p53-mediated repression of PGC-1 α and PGC-1 β decreases mitochondrial biogenesis. Telomerase reactivation can reverse this mitochondrial decline (reviewed in Sahin e DePinho, 2012). Sirtuins also play a role in mitochondrial function. SIRT1 also modulates PGC 1 α activity, influencing biogenesis, and modulating autophagy of damaged mitochondria (Lee et al., 2008). SIRT3, the main mitochondrial deacetylase, targets enzymes involved in the energy metabolism and antioxidant activity (Lombard et al., 2007; Giralt and Villarroya, 2012). The balance between mitochondrial biogenesis, functionality, and turnover is very important and activities known to improve healthspan, like intense physical activity and intermittent fasting can retard mitochondrial degeneration through, at least in part, induction of autophagy (reviewed in López-Otín et al., 2013).

Cellular senescence

Cellular senescence is defined as a permanent arrest in the cell cycle and it can be triggered by telomere attrition, non-telomeric DNA damage and de-repression of the INK4/ARF locus (expressing $p16^{INK4a}$ and $p19^{ARF}$, part of senescence implementing pathways), alterations that occur during natural ageing. Although senescence is normally considered a contributor to the ageing process, its purpose is to avoid the propagation of damaged cells, activating clearance of these cells by the immune system. The accumulation of senescent cells in old organisms is probably a result of an imbalance between clearance and replacement, caused, for example, by an attenuated immune system response and exhausted regenerative capacity (López-Otín et al., 2013). Like DUA damage, oncogenic or mitogenic signalling can trigger senescence. The $p16^{INK4a}$/Rb and $p19^{ARF}$/p53 pathways are the most important senescence implementing pathways and the expression of $p16^{INK4a}$ and $p19^{ARF}$ are significantly related to chronological ageing of different tissues in mice and in human fibroblasts (in vitro) and skin cells (in vivo) (Krishnamurthy et al., 2004; Ressler et al., 2006). Additionally, in mice, the age-associated increase in the expression of $p16^{INK4a}$ is attenuated by calorie restriction with a decrease in organ degeneration also being observed (Krishnamurthy et al., 2004). Baker et al., (2011) demonstrated that, in mice, elimination of $p16^{INK4a}$-positive senescent cells delayed age-related disorders. These data indicate that senescence needs a fine balance between clearance and replacement of cells in a tissue to be beneficial in its attempt to prevent propagation of damaged cells (López-Otín et al., 2013).

Stem cell exhaustion

Another manifestation of ageing, stem cell exhaustion, impacts the regenerative capacity of tissues and organs. In humans, decreased haematopoiesis results in reduced production of adaptive immune cells and an increased risk of anaemia and myeloid neoplasia. Studies have also demonstrated similar age-related stem cell attrition in other tissues, like bones and muscles (López-Otín et al., 2013). Stem cell exhaustion seems to be also linked to the INK4/ARF locus. A study published by

Janzen et al., (2006), have reported that the increase in expression of $p16^{INK4a}$, characteristic in many aged cell types, is also observed in haematopoietic stem cells (HSC), modulating ageing related functions. Furthermore, in the absence of $p16^{INK4a}$, HSC exhibited increased regeneration capacity. Telomere attrition also impacts stem cell exhaustion. Animals with telomere defects have increased activation of senescence and apoptosis in stem cell compartments like haematopoietic tissue, intestinal crypt, and testes (reviewed in Sharpless and DePinho, 2007). Stem cell quiescence is important for maintaining longer regenerative capacity. Kippin et al., (2005) demonstrated that p21 null mice, lacking this cyclin-dependent kinase inhibitor involved in linking DNA damage to cell cycle arrest, had higher proliferation rates of neural stem cells (NSC), compared to wild-type mice, until 240 days of age; after this period, p21 null mice had a decline in NSCs compared to control mice. P21 null NSC also displayed limited self-renewal capacity in vitro, compared to wild-type NSC. Dietary restriction and mTOR pathway inhibition can also impact stem cells, with decreased mTOR activity resulting in enhanced self-renewal capacity of HSC and intestinal stem cells (ISC) (Chen et al., 2009; Yilmaz et al., 2012).

Altered intercellular communication

Altered intercellular communication is also affected by ageing, with inflammation being one of the most prominent alterations. Age-related inflammation can be the result of an accumulation of proinflammatory tissue damage, failure of the immune system to eliminate pathogens and dysfunctional cells, increased secretion of proinflammatory cytokines, defective autophagy response, among others. Inflammation is also related to diabetes, obesity, atherosclerosis and can inhibit epidermal stem cell function (López-Otín et al., 2013). Analysis of 365 microarrays comprising 9 different tissues predicted 14 motifs associated with ageing, and the transcription factor NF-κB is the most strongly associated with ageing. NF-κB controls the expression of genes involved in inflammation and its inhibition in epidermal tissue of old mice reverted age-related characteristics and gene expression patterns to resemble those of young mice epidermis (Adler et al., 2007).

Genetic and pharmaceutical inhibition of NF-κB delayed age-related characteristics of progeroid mice and also reduced oxidative DNA damage and cellular senescence (Tilstra et al., 2012). Sirtuins can also influence the inflammatory response. SIRT1 can influence deacetylating histones and components of inflammatory signalling pathways like NF-κB, down-regulating their activity (Xie et al., 2013). Accordingly, low levels of SIRT1 is correlated with inflammatory diseases (López-Otín et al., 2013).

Loss of proteostasis

Protein homeostasis, or proteostasis, is crucial for health and is impacted by the ageing process. Many ageing-related diseases are linked to loss of proteostasis, like cystic fibrosis (loss of function disease) and Alzheimer's, Parkinson's and Huntington's diseases (gain of toxic functions) (Powers et al., 2009). Factors and mechanisms important to proteostasis are those involved in protein synthesis/folding/unfolding, like ribosomes, chaperones, aggregases and disaggregases; protein degradation, like proteases, autophagy, lysosomal targeting, etc; and posttranslational modification, like oxidation, phosphorylation and acetylation (Powers et al., 2009). They are part of an important quality control array to preserve proteostasis, functioning co-ordinately to assist correct folding of misfolded polypeptides or direct defective proteins to degradation, preventing intracellular accumulation of damaged proteins (López-Otín et al., 2013). During ageing, stress-induced expression of chaperones is impaired and the heat shock response declines, contributing to the incidence of protein aggregation diseases (Calderwood et al. 2009). Morrow et al. (2004), demonstrated that flies overexpressing Hsp22 in motorneurons maintain for longer their locomotor activity; additionally, when Hsp22 was overexpressed ubiquitously, flies had increased lifespans. Sirtuins are also involved in the activation of the heat shock response. In mammalian cells, activation of SIRT1 increased deacetylation of heat shock factor 1 (HSF-1), which augmented activation of heat shock genes like Hsp70; inhibition of SIRT1 reduced the heat shock response (López-Otín et al., 2013). Autophagy also contributes to proteostasis and impacts the ageing process. Decreased autophagy

is observed in normal and pathological ageing, and inhibition of autophagy induces degeneration in mammalian tissues (Rubinsztein et al., 2011). Another proteolytic system, the ubiquitin-proteasome system (UPS), which is the major pathway for protein degradation (Kruegel et al., 2011) shows decreased activity during the ageing process. Insufficient autophagy can compromise the degradation of UPS substrates (López-Otín et al., 2013 and Rubinsztein et al., 2011). Autophagy also plays a role in changes that increase lifespan, since autophagy inhibition impairs the lifetime extension effects of dietary restriction, rapamycin administration, SIRT1 activation, inhibition of insulin/insulin growth factor signalling, etc (reviewed in Rubinsztein et al., 2011). Rapamycin can also contribute to proteostasis through inhibition of S6 protein kinase 1 (S6K1), necessary for protein synthesis. Providing supporting evidence for the importance of the protein quality control system for the ageing process, Kruegel et al. (2011) demonstrated that increased UPS capacity increases lifespan and resistance to proteotoxic stress in yeast.

1.2.2. Yeast as a model organism for ageing studies

The budding yeast *S. cerevisiae* plays an important role in molecular ageing studies. It has contributed to the discovery of more ageing-related genes than any other model organism (Longo et al., 2012) due to its short generation time, amenability to genetic and biochemical methods and because many of the features of ageing observed in this organism are conserved in invertebrate and mammalian models (Kaeberlein, 2010). Consistently, many features of human ageing are present in yeast, especially genomic instability, epigenetic alterations, mitochondrial dysfunctions, deregulated nutrient sensing and loss of proteostasis (Janssens and Veenhoff, 2016). Two ageing models have been studied in yeast, replicative lifespan (RLS) and chronological lifespan (CLS). Replicative lifespan is reflected in the number of daughter cells a mother cell can produce before reaching senescence and is a model of mitotically active cells (Kaeberlein, 2010), with a hypothesis also linking replicative ageing to stem cell exhaustion (Longo et al., 2012; Janssens and

Veenhoff, 2016). Chronological lifespan is defined by how long a cell can survive in a nondividing state and is a model of post-mitotic ageing.

In yeast, genomic instability studies were performed mainly because of its relevance to cancer (Janssens and Veenhoff, 2016), but have provided good evidence for the importance of genomic instability to the ageing process. Mutations in the yeast gene *SGS1*, which encodes RecQ helicase (important to genome maintenance and stability), and in the human homolog *WRN*, cause premature ageing in both organisms (McVey et al., 2001). The *WRN* gene is mutated in Werner and Bloom progeria syndromes and mutation of the yeast version, *SGS1*, decreases lifespan by 60%. Additionally, mutations in the nuclease/helicase gene *DNA2* cause premature signs of ageing in yeast, as do nuclease gene *RAD27* mutants (Hoopes et al., 2002), pointing to the important role genomic stability plays in the yeast ageing process. Providing further evidence of the existence of conserved ageing mechanisms between yeast and humans, the lifespan of *dna2* mutants is extended by overexpression of the *SIR2* gene, a *SIRT1* homolog (Hoopes et al., 2002).

Sirtuins are also important for their ability to modulate epigenetic alterations and increase lifespan in different organisms (Janssens and Veenhoff, 2016). Kaeberlein et al., (1999), demonstrated that yeast *sir2*, *sir3* and *sir4* mutant strains have shortened lifespan while overexpressing SIR2 increased lifespans. In 2009, Dang et al., demonstrated the importance of histone H4 lysine 16 acetylation for yeast longevity, where *SIR2* gene plays a role. They report an age-associated decrease in Sir2 protein abundance with a consequent increase in histone H4 lysine 16 acetylation and a reduction in histones at subtelomeric regions. Moreover, Sarg et al., (2002) reported a significant increase in trimethylation of histone H4 at lysine 20 in different organs of old rat.

Mitochondrial dysfunction is also a feature of ageing in yeast. Janssens et al., reported in 2015 that some mitochondrial components are reduced in old yeast

cells. Additionally, Hughes and Gottschling, in 2012, demonstrated that vacuolar pH influences mitochondrial function, with a decrease in vacuolar acidity being observed in old cells. When vacuolar acidity was maintained, mitochondrial functionality was preserved, resulting in increased lifespan. They also observed that calorie restriction increased vacuolar acidity, benefiting mitochondrial function.

Alterations in nutrient sensing have been observed in yeast, with decreases in glycolysis accompanied by increases in gluconeogenesis and energy storage in old cells (Janssens and Veenhoff, 2016). Lin et al., (2001) have observed how alterations in the activity of Snf1p, a serine/threonine kinase that modulates responses to glucose starvation, influenced lifespan. In the absence of the Snf1p activator, Snf4p, yeast cells lived longer, while in the absence of theSnf1p repressor, Sip2p, ageing was accelerated. Transcriptional responses also demonstrated an age-related augmentation of gluconeogenesis and glucose storage in wild-type cells, with *sip2*Δ cells displaying an exaggerated shift to this metabolic alteration and *snf4*Δ cells displaying reduced gluconeogenesis and glucose storage (Lin et al., 2001). Additionally, increasing the level of downstream intracellular effectors of dietary restriction, like FOXO transcription factors, known to increase lifespan in higher eukaryotes, also increases lifespan in yeast (Postnikoff et al., 2012). Increased expression of the yeast forkhead box transcription factor FKH1 and FKH2 promoted longer lifespan and improved stress-response (Postnikoff et al., 2012). Janssens and colleagues also demonstrated in 2015 that the content of yeast proteome is not directly predictable from to the transcriptome in old cells, mainly due to an increased abundance of translation machinery components. This can be the result of an age-related increase in the nutrient-sensing mTOR pathway activity, which also modulates translation (Janssens et al., 2015; Janssens and Veenhoff, 2016). Kaeberlein et al., (2005) already demonstrated that deletion of *SCH9*, the yeast functional ortholog of the mammalian S6K, or deletion of *TOR1* increases lifespan in yeast. In the same work, they performed a large-scale analysis of 564 single-gene deletion strains and found 10 gene deletions that promoted longevity. Six of those

genes are part of the TOR and Sch9 pathways (Kaeberlein et al., 2005). Taken together, these data also point to the connection between deregulated nutrient sensing and proteostasis (Janssens and Veenhoff, 2016).

Proteostasis is maintained by a fine balance between protein synthesis, chaperone-mediated protein folding, autophagy and proteasomal degradation (Janssens and Veenhoff, 2016). Imbalances between these functions can lead to protein aggregation, which is deleterious and known to contribute to ageing-related diseases like Alzheimer's, Parkinson's, and Huntington's (Janssens and Veenhoff, 2016). Many chaperones are heat shock proteins (HSP) and the heat shock response decreases during the ageing process (Calderwood et al., 2009). Old cells lose their capacity to activate HSP synthesis through transcriptional pathways and this affects muscles, neurons and liver (Calderwood et al., 2009). In yeast, Janssens and colleagues observed an age-related decrease in protein folding and protein targeting components (Janssens et al., 2015). Interestingly, proteins involved in responses to heat, osmotic and oxidative stresses are increased with ageing (Janssens et al., 2015; Janssens and Veenhoff, 2016). Additionally, the ubiquitin-proteasome system is part of the protein homeostasis promoting machinery, being the major pathway for protein degradation, whereas its capacity decreases with ageing (Kruegel et al., 2011). In yeast, manipulation of UPS can strongly increase lifespan, through augmented proteasome abundance, or decrease lifespan through decreased proteasome abundance (Kruegel et al., 2011). A similar correlation between clearance of toxic huntingtin protein (involved in Huntington's disease) fragments and lifespan is also observed in a yeast model for neurodegenerative diseases (Kruegel et al., 2011). This provides evidence that proteostasis is indicative of ageing in yeast, and also emphasize the importance of yeast as a model organism for studying ageing, from the basis of its mechanism to the complexity of ageing-related diseases like Huntington's.

1.2.3. Translation control and the ageing process

A significant number of interventions known to influence lifespan and healthspan target and modulate components of the translation machinery. Evolutionarily conserved pathways affecting the ageing process, like insulin/IGF-1, mTOR, the p38 mitogen protein kinase and Mnk1 (mitogen-activated protein kinase-interacting kinase), components of the mitogen-activated protein kinase (MAPK) pathway, also regulate protein synthesis (Gonskikh and Polacek, 2017, Tavernarakis, 2008). These signalling pathways influence mRNA translation in quantitative and qualitative ways, modulating phosphorylation of translation machinery components in response to hormones, growth factors and nutrients, thus, promoting cell growth and proliferation and, therefore, stimulating protein synthesis (Tavernarakis, 2008, Roux and Topisirovic, 2012). Downregulation of these pathways increased lifespan in different model organisms and reduced protein synthesis rate (Gonskikh and Polacek, 2017).

In multicellular organisms, the insulin/IGF-1 pathway lie upstream mTOR and MAPK pathways (Janssens and Veenhoff, 2016), regulating kinase cascades.
The mTOR pathway is evolutionarily conserved and exists in two different protein complexes, referred to as mTOR complex 1 (mTORC1) and mTOR complex 2 (mTORC2). mTORC1 regulates several cellular processes like growth, autophagy, proliferation and translation in response to nutrient and energy availability. It is responsive to rapamycin, that works as an allosteric inhibitor (Roux and Topisirovic, 2012). mTORC2 regulates cytoskeletal organization and cell survival and its upstream regulators and substrates are less well understood. mTORC2 is not responsive to rapamycin in short treatment (Roux and Topisirovic, 2012).

Insulin receptors (IRS) activate the insulin/IGF-1 pathway and, consequently, the mTOR pathway through a cascade of events. IRS stimulation results in the activation of the phosphatidylinositol 3 kinase (PI3K), which in turn converts

phosphatidylinositol (4,5)-bisphosphate (PIP2) to phosphatidylinositol (1,4,5)-trisphosphate (PIP3) (Tavernarakis, 2008). PIP3 activates Akt kinase, responsible for phosphorylation of the GTPase activating protein TSC2, inhibiting its activity and, consequently, maintaining the small GTPase Rheb (Ras homolog enriched in the brain), active (Gonskikh and Polacek, 2017, Tavernarakis, 2008). Rheb binds to the mTORC1, activating it by promoting conformational changes that allosterically realigns activate-site residues, positioning them into the correct alignment for catalysis (Yang et al., 2017). Activation of the mTOR pathway primarily regulates translation initiation but also affects translation elongation and the activity of ribosomal components. An active mTOR leads to eIF4E-binding protein (4E-BP) phosphorylation, increasing the availability of the eIF4E initiation factor, favouring then its interaction with eIF4G and promoting cap-dependent translation initiation (Gonskikh and Polacek, 2017). A decrease in 4E-BP phosphorylation upon mTOR downregulation, reduces the pool of available eIF4E, therefore decreasing cap-dependent translation. mTOR also modulates the function of the eEF2 kinase; when mTOR is active, it promotes eEF2 kinase phosphorylation and consequent inactivation. When eEF2 kinase is inactive, the elongation factor eEF2 is kept functional and elongation continues at full efficiency. (Gonskikh and Polacek, 2017). mTOR downregulation leads to activation of the eEF2 kinase, which phosphorylates eEF2, inactivating this factor and impairing elongation. mTOR signalling also leads to activation of S6 kinases 1 and 2 (S6K1 and S6K2), that phosphorylates and activates the S6 small ribosomal subunit (Gonskikh and Polacek, 2017; Tavernarakis, 2008).

The Insulin/IGF-1 pathway can also regulate the activity of the MAPK pathway. This signal transduction pathway is also conserved through evolution, participating in many cellular processes. All eukaryotic cells have a MAPK pathway, which regulates processes including metabolism, mitosis, gene expression, differentiation, among others (Roux and Topisirovic, 2012). Stimulation of insulin/IGF-1 pathway regulates MAPK pathway components through the activity of small Ras GTPases, which

sequentially activate Raf, MEK and ERK (Roux and Topisirovic, 2012). ERK (extracellular signal-regulated kinases) 1 and 2 control the activity of the MAPK interacting kinase Mnk1, in a stimulatory manner (Tavernarakis, 2008). Mnk1 is also stimulated by p28 MAPK in response to environmental stress (Tavernarakis, 2008; Roux and Topisirovic, 2012). Mnk1 interacts with the initiation factors eIF4G and eIF4E, binding directly to eIF4G and phosphorylating eIF4E. Phosphorylation of eIF4E promotes a more stable interaction with both eIF4G and 5' cap of the mRNA, which in turn favours translation initiation (Gonskikh and Polacek, 2017). Additionally, ERK1 and ERK2 also stimulate the S6 kinase, activating, like the mTOR pathway, the S6 small ribosomal subunit (Tavernarakis, 2008).

Providing supporting evidence that translation rate plays an important role in lifespan modulation, Zid et al., (2009) demonstrated that 4E-BP is required for maximal lifespan increase in *Drosophila melanogaster* during dietary restriction; additionally, overexpression of 4E-BP extends the lifespan in flies, even in a non-restrictive diet. Consistently, Ruggero et al., (2004) demonstrated that overexpression of eIF4E promotes senescence in mouse embryonic fibroblasts and, in mice, upregulation of eIF4E significantly increased tumorigenesis. Additionally, Pan et al., (2007) demonstrated that in *Caenorhabditis elegans*, downregulation of *ifg-1* (worm homologue of eIF4G) increased lifespan, as well as downregulation of *rsks-1* (worm homologue of S6 kinase). Together, these data demonstrate the importance of translation control in longevity.

It is generally considered that accumulation of cellular damage is an indication, and also a cause, of ageing and of ageing-associated diseases (Gonskikh and Polacek, 2017; López-Otín et al., 2013). Increased protein production is also accompanied by the production of damaged proteins due to transcriptional, translational or folding errors. Damaged proteins have the tendency to accumulate in the cell, forming toxic aggregates (Gonskikh and Polacek, 2017). The protein quality control system can target this issue by directing misfolded or damaged proteins to assisted folding or

degradation, but, during ageing, the activity of proteolytic systems, including the cytosolic proteasomal system, decline resulting in increased half-life of damaged proteins (Gonskikh and Polacek, 2017; Tavernarakis, 2008). Decreased protein biosynthesis due to depletion of translation factors or ribosome components slows down the rate of damaged protein production, reducing the accumulation of toxic proteins (Gonskikh and Polacek, 2017).

Although Saarikangas and Barral in 2015 demonstrated that, in mid-aged budding yeast, protein aggregates formed under unstressed conditions do not compromise the efficiency of the protein quality control system, they also demonstrated that deletion of protein quality control components reduced lifespan. The authors observed that yeast cells naturally formed a single deposit of aggregated proteins, which did not impair the cell capacity to revert to its normal state after stress exposure. Additionally, cells containing the protein deposit displayed an accelerated ubiquitin-proteasome system degradation activity. But, when the protein disaggregase Hsp104 was deleted, cells had a significant decrease in lifespan, showing that accumulation of protein aggregates promotes ageing. Consistently, deletion of Hsp70 proteins, SSa1 and Sa2, which act synergistically with Hsp104 in protein refolding resulted in accelerated formation of protein aggregates focus. Together, the Hsp104/Hsp70 system counteracts protein aggregation, which is essential to longevity (Saarikangas and Barral, 2015). Hsp70 chaperones also aid the folding of nascent proteins and, in conditions of proteotoxic stress, these chaperones are sequestered away from the ribosome, impairing elongation and making the ribosome to stall (Steffen and Dillin, 2016).

Very interestingly, Janssens et al., (2015) performed a system-level transcriptome and proteome analysis in ageing yeast, demonstrating that, as the cells age, the proteome increasingly uncouples from the transcriptome. Strikingly, the study demonstrated a global tendency of protein overabundance related to their mRNA levels in the cell and, furthermore, proteins involved in translation activity were

significantly overrepresented compared to their transcripts. The protein overrepresentation progressively augmented as the cells aged and, based on further analysis, the authors developed a model that demonstrates that this protein overrepresentation is causal for ageing. Translation machinery proteins accumulate in the cells during the ageing process, which can intensify proteome uncoupling from transcriptome as a whole, favouring degenerative effects like loss of protein stoichiometry in complexes and formation of toxic protein aggregates (Janssens et al., 2015).

1.3. Gene expression stochasticity

1.3.1. Overview

Gene expression stochasticity, or gene expression noise is reflected in proteome heterogeneity in otherwise genetically identical cells. This can be the result of variations in transcription and translation, even under constant environmental conditions (Kærn et al., 2005). Stochasticity can play a role in different biological processes, including cellular differentiation (Chang et al. 2008), protein biosynthesis and oxidative stress responses (Janes et al., 2010), and synchrony in circadian clocks (Barkai and Leibler, 2000). Noise can also be potentially damaging, limiting the accuracy of gene expression and cellular processes, impacting cellular signalling and regulation (Elowitz et al., 2002; Raser and O'Shea, 2005). The ageing process can also be detrimentally impacted by noise, with research showing that ageing is correlated with increased gene expression noise (Newlands et al., 1998; Rea et al., 2005; Bahar et al., 2006, Raj et al. 2008). Furthermore, stochasticity is a biologically important variable, being subjected to natural selection forces. In some conditions, where elevated gene expression noise is beneficial, it can be subject to positive selection (Zhang et al., 2009). Other work has indicated that the synthesis of essential proteins has evolved to minimise harmful stochastic variation, in the sense

that these proteins manifest reduced level of noise, compared to the production of other genes (Fraser et al., 2004; Lehner, 2008).

Experimental observations that individual cells manifest variations in gene expression are not entirely new. The first research to detect this phenomenon was performed by Novick and Weiner in 1957. The authors demonstrated that the expression of the enzyme beta-galactosidase in bacteria was variable, with some individual cells expressing the enzyme at the maximum rate, while others expressed none. They observed that the average rate of enzyme synthesis in a cell population is attributable to individual cells expressing a range of different levels, including some cells generating a maximum amount and some generating no enzyme (Novick and Weiner., 1957). Later on, in 1990, Ko et al. examined, at a single-cell level, the expression of a glucocorticoid-responsive transgene encoding beta-galactosidase in response to different doses of glucocorticoid and found that heterogeneity in the expression of this transgene was high. Increased glucocorticoid doses increased the number of cells showing some level of expression of the transgene rather than increasing the expression in every cell (Raj et al., 2008).

The biochemical processes responsible for gene expression are inherently stochastic, being dependent on molecular interactions, and are, therefore, the result of random encounters (Kærn et al., 2005). The causes and consequences of stochasticity in the expression of a gene can be demonstrated by comparing the protein concentrations obtained from stochastic simulations, which take into account the random formation and decay of molecules, and from deterministic simulations, which do not take stochastic processes into account. Normally, the deterministic simulations cannot capture the effects of stochasticity in gene expression, but in the case of large system sizes (high number of mRNA and protein molecules and large cell volumes) and fast promoter kinetics, the protein concentration predicted by stochastic and deterministic simulations are similar.

However, when these conditions are not met, the effects of molecular-level noise can significantly impact gene expression (Kærn et al., 2005).

The molecular-level of gene expression noise can be investigated by comparing intracellular protein and/or mRNA concentrations and the relative deviations of these from the average. This can be measured by calculating the ratio of the standard deviation (SD) to the mean, referred to as the coefficient of variation (CV).

The landmark study performed by Elowitz et al. (2002) investigated the origins of gene expression noise and introduced the concepts of intrinsic stochasticity and extrinsic stochasticity in gene expression (Raj et a., 2008). The authors used two fluorescent reporters, the cyan fluorescent protein (CFP) and yellow fluorescent protein (YFP) regulated by the same promoter to study variability in gene expression in *Escherichia coli*. In this experiment, intrinsic noise arises from processes inherent to transcription and translation and affect each reporter independently, making their expression uncorrelated. Extrinsic noise, on the other hand, arises from variations in cellular states and locations of molecules (*e.g.* polymerases) affecting the expression of both reporters equally (Elowitz et al., 2002; Raj et a., 2008).

Although the procedure of Elowitz et al. (2002) to measure the intrinsic and extrinsic components of gene expression noise is frequently adopted (using microscopy to examine the expression of the described dual reporter), Newman et al., (2006), developed a new methodology to study intrinsic noise using flow cytometry. Much of the variation seen in protein levels between isogenic cells are the results of variations in cell size and cell cycle states, which can obscure the cause of protein-specific variations. Flow cytometry can reduce the contribution of these factors, since it can provide approximate measures of cell size (using the forward scatter (FSC) parameter) and granularity or complexity (using the side scatter (SSC) parameter) (Newman et al., 2006). The authors performed a gating strategy by defining a circular gate centred in the FSC and SSC median and varying its radius.

They noticed that the gating strategy successfully eliminated the two peaks observed for the GFP-tagged histone subunit Hhf2, which is cell-cycle-regulated. Additionally, they performed a modified version of the dual reporter experiment described by Elowitz et al., 2002, and demonstrated that, while ungated cells were dominated by extrinsic noise, the gating analysis decreased the contribution of extrinsic noise to levels comparable to intrinsic noise (Newman et al., 2006). In this study, the authors demonstrated that proteins involved in the process of protein synthesis are less noisy than those involved in response to environmental changes, pointing to the importance of accurate protein synthesis regulation for the cell.

1.3.2. Correlation between gene expression stochasticity and other biological processes

Phenotypic heterogeneity and survival

For microbial cells, gene expression noise can be useful in providing phenotypic heterogeneity, which can increase survival rates in case of sudden environmental changes (Booth, 2002, Thattai and Oudenaarden, 2004). Variation in gene expression can be an advantageous mechanism to sample different physiological states and phenotypes that, in times of stress, could increase the probability of survival without the need for genetic mutation (Kærn et al., 2005). Thattai and Oudenaarden, in 2004, investigated this phenomenon using a stochastic population model and showed that a heterogeneous population of isogenic bacteria (the result of noisy gene expression) can achieve a faster growth rate in a fluctuating environment when compared to a homogeneous population. A heterogeneous population can, therefore, have a fitness advantage in case of sudden environmental changes, increasing the chance of survival (Thattai and Oudenaarden, 2004; Kærn et al., 2005).

Resistance to treatment

Although phenotypic heterogeneity can be beneficial to a microorganism, it can seriously impact the efficacy of medical treatments. Switching between physiological states and phenotypes may contribute to persistent bacterial infections (Kærn et al., 2005). Balaban et al. demonstrated in 2004 that, in contrast to mutant strains that are truly resistant to the antibiotic, some cells that survive the treatment remain sensitive to the antibiotic. The authors investigated *E. coli* and observed that persistence was correlated to pre-existing phenotypic heterogeneity in the population, with persistent cells growing at a reduced rate (Balaban et al. 2004). Although the majority of the cells are eliminated by the antibiotic, a subpopulation of the genetically identical cells is in a dormant state and survives the treatment period. Once the antibiotic is removed, the subset of dormant cells switches back to a normal growth rate, which results in infection reappearance (Kærn et al., 2005).

Another example of a pathogen difficult to target pharmacologically is the human immunodeficiency virus (HIV). After HIV infection, a subset of latent CD4 T lymphocytes containing the integrated virus does not express it. This reduced or absent expression impairs pharmacological targeting of these cells, which hinders treatment (Raj et al., 2008). In 2005, Weinberger et al. demonstrated that noise in the expression of the Tat protein can create cells with different levels of viral expression. Tat protein increases viral transcription and its transactivation is essential to the completion of the viral life cycle. Stochastic variations in Tat impacts viral latency decision, and thus, impacts HIV treatment as well (Weinberger et al., 2005; Raj et al., 2008).

Development

During development and cellular differentiation, gene expression noise can play a beneficial role (Kærn et al., 2005). During the development of *Drosophila melanogaster*, the epidermal—neural choice involved in the emergence of neural

precursor cells from an initially homogeneous population can be determined by stochasticity in the turnover of two proteins, Notch and Delta (Simpson, 1997; Kærn et al., 2005). Thus, noise contributes to this process of cellular differentiation.

Another example of stochasticity playing a role in cellular differentiation is the process of hematopoiesis. Chang et al., (2008) demonstrated that stochasticity in the expression of the Sca-1 stem cell marker is involved in the cell decision to become an erythroid or myeloid lineage (Chang et al., 2008; Raj et al., 2008).

Cancer

Han et al., 2016, demonstrated in a genomic scale investigation that cancer cells have increased gene expression noise compared to normal cells. The authors analysed the transcriptomic data of human breast, liver, lung and colon cancers and observed that gene expression noise was increased in 74.9% of the 16,424 genes analysed, in comparison with normal tissues. Their findings suggest that the necessary accuracy of gene expression collapsed during cancer development (Han et al., 2016). It was also observed in this study that patients with low p53 and low immune activity had a tendency of increased gene expression noise. The p53 pathway is involved in maintaining genome stability and is frequently mutated in cancers. Additionally, they found that more than 53% of genes displayed increased stochasticity in patients with late-stage, as opposed to early-stage cancer, indicating that accuracy in gene expression was linked to the cancer outcome (Han et al., 2016).

Ageing

A few studies indicate that gene expression noise might play a role in the ageing process. Newlands et al., 1998 investigated gene regulation in skeletal muscle fibres, observing that not all muscle loci are transcriptionally active simultaneously and that the number of active loci declines with fibre maturation. Additionally, the author observed that in a fully mature fibre, the expression of a locus appears to be

random, with the mechanism of regulation being stochastic and transcription occurring in pulses.

In 2006, Bahar et al. investigated the transcriptional noise of housekeeping and heart-specific genes in mouse cardiomyocytes and found that gene expression stochasticity increases with age. Additionally, the authors treated young cardiomyocytes with hydrogen peroxide, to induce oxidative damage. They found that this treatment increased the level of gene expression noise, indicating that oxidative damage might affect stochasticity.

In the study performed by Rea et al. (2005), the authors investigated an isogenic population of *Caenorhabditis elegans* and found that the level of stochasticity in the expression of a reporter coupled to a heat shock promoter on the first day of adulthood was linked to the lifespan of the organism.

These earlier studies pointed to an important connection between ageing and gene expression noise, but are only at the beginning of the investigation of the mechanistic principles underpinning this apparent relationship.

1.4. Aim of this study

To investigate in *S. cerevisiae* the relationship between protein synthesis rate, gene expression noise and the ageing process using two different and independent methodologies: microfluidics and flow cytometry.

In order to use flow cytometry in this investigation it is necessary to apply and validate a cell-wall staining strategy that will enable the identification of old cells in an exponentially growing culture, allowing then the observation of cells over their ageing process.

Chapter 2 - Materials and methods

2.1. Strains, plasmids and primers

2.1.1. Strains used in this study

Table 1: *Escherichia coli* strains

Strain name	**Collection number**	**Genotype**	**Remarks**	**Source**
Top 10F'	PTC46	F' [laclq Tn10(TetR)] mcrA d(mrr-hsdRMS-mcrBC) (80 lacZdM15 dlacX74 deoR recA1 araD139 d(ara-leu)7697 galU galK rpsL(StrR) endA1 nupG	Used for plasmid cloning	INVITROGEN

Table 2: *Saccharomyces cerevisiae* strains

Strain name	**Collection number**	**Genotype**	**Source**
Wild-type (W303 derived)	PTC41	*MATalpha ade2-1 ura3-1 leu2-3,112 his3-11,15 can1-100*	M. Tuite, University of Kent
Wild-type	PTC1076	*MATalpha ade2-1 ura3-1 leu2-3,112 his3-11,15 can1-100*, *his3::HIS3::Ylp-HK-*P_{TEF1}*-yEGFP-MS2SL-PGK1t*	This study

Table 2: *Saccharomyces cerevisiae* strains (continued)

Strain name	**Collection number**	**Genotype**	**Source**
tif4631Δ	PTC1077	*MATalpha ade2-1 ura3-1 leu2-3,112 his3-11,15 can1-100, tif4631Δ, his3::HIS3::Ylp-HK-P_{TEF1}-yEGFP-MS2SL-PGK1t*	This study
tif4632Δ	PTC1078	*MATalpha ade2-1 ura3-1 leu2-3,112 his3-11,15 can1-100, tif4632Δ, his3::HIS3::Ylp-HK-P_{TEF1}-yEGFP-MS2SL-PGK1t*	This study

2.1.2. Plasmids used in this study

Table 3: List of plasmids

Plasmid name	**Description**	**Markers**	**Source**
pNM1-HIS	Plasmid containing P_{TEF1} promoter controlled yEGFP_mut3 gene with a synthetic 5'UTR (L0) followed by MS2 stem loop sequence (24 loops). Used to generate transforming DNA for integration in yeast genome after restriction enzyme digestion.	AmpR and HIS3	This study

2.1.3. Oligonucleotides used for construction and confirmation of strains

Table 4: List of Primers

Name	**Sequence (5'-3')**
HIS3 flanking R	TCGAAGATAGGATTATCATTCATAAGTTTCAG
HIS3Δ1 Insertion F New Tail:	TGACCGAGAGCAATCCCGCAGTCTTCAGTGGTGTGATGGT CGTCTATGTGTGCAGCTCCCGGTCATTATC
OPS 169	TACGGAATACCACTTGCCACC
OPS 231	ACCGTTAATAGCAACTCTAACC
Amp R	GCTGTTGAGATCCAGTTC
OPS277	TTGCTTTGCTGTGGGAAAAACTTATCGAAAGATGACGACT AGTGAGCGAGGAAGCGGAAGAGC
yeGFPout2F	AGACCACATGGTCTTGTTAG

2.2. Media and buffers

2.2.1. Bacterial media

2.2.1.1. Super Optimal broth with Catabolite repression (SOC)

To prepare chemically competent or to transform *E. coli* cells, Super Optimal broth with Catabolite repression (SOC) media was used. SOC contains 2% w/v tryptone, 0.5% w/v yeast extract, 10 mM NaCl, 2.5 mM KCl, 10 mM $MgCl_2$, 10 mM $MgSO_4$

and 20 mM glucose. It was prepared by dissolving MP Biomedicals SOC (Powder) (Fisher Scientific) in the appropriate volume of sterile water.

2.2.1.2. Luria-Bertani Broth (LB Broth)

To transform *E. coli* cells, LB Broth could also be used. It is composed of 1% w/v tryptone, 0.5% w/v yeast extract and 1% w/v sodium chloride. It was prepared by dissolving granulated Luria Broth (Melford) in the appropriate volume of sterile water.

2.2.2. Yeast media

For yeast strain transformation YPD media was used. YPD contains yeast extract (Formedium) at 1% w/v concentration, peptone (Sigma-Aldrich) at 2% w/v concentration and glucose (Fisher Scientific) at 2% w/v concentration as carbon source. To prepare plates, agar (Formedium) was added to a final concentration of 2% w/v.

For experiments, synthetic media was used, prepared by mixing 6.9 g/L of Yeast Nitrogen Base without Amino Acids (Formedium) and 690mg/L of Complete Supplement Mixture (Formedium). For auxotrophic selection, the specific amino-acid was omitted from the medium. To prepare low fluorescence media for time-lapse experiments, 6.9 g/L Yeast Nitrogen Base without Amino Acids, without folic acid and without riboflavin was used. For this media, Complete Supplement Mixture without phenylalanine, tryptophan and tyrosine was used (690mg/L). Since some strains in this study lack *ADE2* gene, adenine supplementation was necessary to avoid autofluorescence. Therefore, adenine (adenine hemisulphate - Sigma-Aldrich) was added to the media to a final concentration of 100 µg/mL.

2.2.3. Phosphate buffer saline (PBS)

PBS was used for cell washing and staining steps, and it is composed of 11.8 mM phosphate (10mM Na_2HPO_4 and 1.8 mM KH_2PO_4), 2.7 mM KCl, 137 mM NaCl in sterile water, pH adjusted to 7.4.

2.3. Cell protocols

2.3.1. Preparation of chemically competent *E. coli* cells

Adapted from Hanahan et al. 1991. Bacterial cells were cultivated overnight at 18˚C in SOC media. In the morning, cells were diluted in 200mL of fresh LB medium to OD_{600} 0.1. The culture was then cultivated at 30˚C until reaching OD_{600} 0.6. After incubation, cells were chilled on ice for 20 minutes and harvested by centrifugation at 4˚C for 10 minutes at 4.000 rpm. Once harvested, cells were chilled on ice, the supernatant was removed and cells were diluted in 100mL of ice cold 0.1M $CaCl_2$. Cells were kept on ice for 30 minutes. Cells were harvested again by centrifugation at 4˚C for 10 minutes at 4.000 rpm and diluted in 8mL of 0.1M $CaCl_2$. Glycerol was carefully added to a final concentration of 20%, the cells were divided in 200 µL aliquots and stored in -80˚C.

2.3.2. *E. coli* transformation

An aliquot of *E. coli* chemically competent cells was thawed on ice for 15-20 minutes. A volume of 2-3 µL of plasmid was added to a 1.5mL tube, then 60µL of competent cells was added with gentle mixing. Incubation on ice was done for 10 minutes, followed by heat shock at 42˚C for 40 seconds and cooling down step on ice for 3-5 minutes. The recovery step was performed with addition of 300µL LB/SOC and incubation at 37˚C for 1 hour. After that, cells were plated on selective medium and incubated overnight at 37˚C.

2.3.3. *S. cerevisiae* transformation

Protocol adapted from Güldener et al, 1996. A yeast culture was grown in appropriate medium and incubated overnight at 30˚C; in the following morning cells were re-suspended in fresh medium and grown until OD_{600} = 0.5-0.8. Cells were harvested by centrifugation and washed in sterile water followed by double washing with 1mL of TE/LiAc (10 mM Tris– HCl pH 7.5, 1 mM EDTA, 0.1 M LiAc pH 7.5). Cells were pelleted and re-suspended in 200µL of TE/LiAc. For chromosomal integration, approximately 5 µL of the PCR product was mixed with 10µL denatured salmon sperm DNA and 50 µl of cells in TE/LiAc. For complementation tests, 3-6µL of plasmid was mixed with 10µL denatured salmon sperm DNA and 50 µl of TE/LiAc cells suspension. 300 µl of sterile 40 % PEG/LiAc (50 % PEG, 10 mM Tris–HCl pH 7.5, 1 mM EDTA, 0.1 M LiAc pH 7.5) was added to the cells with DNA, gently mixed and incubated at 30˚C for 1 hour. Heat shock was done for 40 min at 42˚C. A recovery step of the transformed yeast cells was performed after a washing step in sterile water, with pellet re-suspension in 1 ml of YPD and incubation overnight at 30˚C. In the morning, cells were collected by centrifugation, re-suspended in 600 µl of sterile water, spread onto selective agar plates and incubated at 30˚C for 2-3 days.

2.4. DNA manipulation and cloning protocols

2.4.1. Plasmid isolation from *E. coli* cells

The plasmid containing strain was cultivated overnight and 2-3 mL of culture were centrifuged for 5 minutes at 4000 rpm. Then, the GeneJET Plasmid Purification (Thermo Scientific) miniprep kit was used to isolate plasmid DNA. Purified plasmid DNA was resuspended in 100µL of sterile water and stored at 4˚C.

2.4.2. Yeast fast genomic DNA extraction

Using a protocol adapted from Lõoke et al, 2011, yeast cells were re-suspended in 100µL of 200mM LiAc and 1% SDS solution and incubated at 70˚C for 15 minutes. 300µL of EtOH was added to the cell suspension and mixed using a vortexer. After 3 minutes of centrifugation the pellet was re-suspended in 100µL of sterile water and centrifuged again for 1 minute. The supernatant was used as a PCR template for strain confirmation.

2.4.3. Polymerase chain reaction (PCR)

Polymerase chain reaction was used to amplify the DNA fragment of interest using plasmid or genomic DNA as template, for both analytical or cloning purposes. To confirm the correct transformation of strains, RedTaq Ready-Mix (Sigma) or Taq Mix Red (PCR Biosystems) were used to prepare a final 20µL reaction volume, as follows:

Table 5: PCR reaction table for Taq ready mix

Component	**20µL reaction volume**	**Final concentration**
10µM Forward Primer	0.5µL	0.25 µM
10µM Reverse Primer	0.5µL	0.25 µM
Template DNA	variable	<500ng
2X Taq ready mix	10µL	1X
Sterile dH_2O to complete	20µL	

To amplify DNA for plasmid construction or genomic integration, Expand High Fidelity PCR system (Roche) was chosen because of its proof-reading capacity, which

minimises the chance of errors during DNA amplification. The reaction was prepared to a final volume of 20µL, as follows:

Table 6: PCR reaction table for Expand High Fidelity enzyme

Component	**20µL reaction volume**	**Final concentration**
10µM Forward Primer	0.5µL	0.25 µM
10µM Reverse Primer	0.5µL	0.25 µM
Template DNA	variable	<500ng
Nucleotide mix	0.5µL	200µM (each dNTP)
10X Expand High Fidelity buffer	2.0µL	1X
Expand High Fidelity enzyme mix	0.3µL	1.05 U/reaction
Sterile dH_2O to complete	20µL	

T100 Thermal Cycler (Bio-Rad) was used to perform the reaction. The initial step in the reaction aims to denature template DNA and was set at 98˚C for 5 minutes. The next steps were 30-35 cycles composed of 15-30 seconds of denaturing at 98˚C; 30 seconds of annealing, with temperature depending on primer sequence; and extension at 72˚C for fragments smaller than 3 kb or 68˚C for fragments longer than 3 kb, with time depending on expected fragment size. The last step was a final extension time at 72˚C for 10 minutes.

2.4.4. Agarose Gel Electrophoresis

Electrophoresis separates DNA fragments of different sizes (base pairs) using an electrical field. Negatively charged DNA moves across the agarose gel towards a

positively charged electrode. Agarose gels were prepared at the desired concentration (1-2%) by melting agarose in Tris-acetate-EDTA (TAE) buffer (40 mM Tris-HCl, 20mM Acetate, 1 mM EDTA, pH 8.0) or Tris-borate-EDTA (TBE) buffer (89mM Tris-borate, 89mM boric acid, 2mM EDTA, pH 8.0). After melting, ethidium bromide (0.2 µg/ml) or 0.1 % of SYBR safe DNA gel stain (Invitrogen) was added to the gel before pouring it in casting trays with well-combs. Once polymerisation was complete, PCR product samples mixed with DNA loading dye (30% (v/v) glycerol, 0.25% (w/v) bromophenol blue, 0.25% (w/v) xylene cyanol), along with GeneRuler 1 Kb DNA Ladder (Fermantas), were inserted in wells. Electrophoresis was performed in a BioRad horizontal gel tank, at 100V, using the same buffer the agarose gel was prepared in. Bands were visualised using a BioRad Gel Doc XR+ Gel Documentation System.

2.4.5. PCR product purification

PCR products were purified using the Thermo Scientific GeneJET Plasmid Purification kit. When gel extraction was necessary, Thermo Scientific GeneJET Gel Extraction Kit was used.

2.4.6. Molecular Cloning

Plasmid vectors and DNA fragments of interest were assembled together through restriction enzyme digestion and ligation as described below.

Appropriate restriction enzymes were used to set separated reactions for vector and DNA fragments, which comprised 4µL of appropriate digestion buffer, 2µL of each restriction enzyme, 5-8µL of insert or vector and, to make-up the final 40µL volume, nuclease-free water was added. Reactions were then incubated at 37˚C for 1 hour. Vector dephosphorylation was performed after digestion by adding 1µL of FastAP Thermosensitive Phosphatase (Fermentas) to the reaction and incubating it at 37˚C for 15 minutes, followed by inactivation at 75˚C for 5 minutes. Digested DNA

fragments and vectors were purified using Thermo Scientific GeneJET Plasmid Purification kit and, if required, the digested vector underwent agarose gel electrophoresis for checking size and yield and was then gel purified using Thermo Scientific GeneJET Gel Extraction Kit and diluted in sterile water.

Ligation was performed in an insert/vector molecular ratio of 3/1, and reaction was prepared using 2µL of 10x NEB Ligase buffer (New England Biolabs), appropriate volumes of insert and vector, 1µL of T4 ligase (New England Biolabs) and nuclease-free water to a final volume of 20µL. The reaction was incubated at room temperature for 10 minutes. The new plasmid was used to transform *E. coli* as described in section 2.3.2. of this chapter.

2.4.7. Gibson Assembly

Whenever possible, the Gibson protocol (Gibson et al., 2009) was used to assemble DNA fragments and plasmids. Primers were designed with 5' ends that are identical to an adjacent segment and a 3' end that anneals to the target sequence. PCR was set and the amplified product underwent agarose gel electrophoresis for verifying yield and size, and then was gel-purified using Thermo Scientific GeneJET Gel Extraction Kit and diluted in sterile water. Fragments and vector were combined with Gibson cloning master mix and the reaction mix comprised 15µL of master mix, 3 µL of DNA fragment and 2.0µL of vector, to a final volume of 20µL. The reaction was then incubated at 50˚C for 1 hour.

Gibson cloning master mix was prepared, to a final volume of 1.2mL, using 320 µL of 5x isothermal mix (Tris-HCl 500mM - pH7.5, $MgCl_2$ 100mM, dATP 1mM, dCTP 1mM, dGTP 1mM, dTTP 1mM, DTT 50mM, PEG8000 30mM, NAD: 5mM, ddH_2O to the desired volume), 0.64µL of T5 exonuclease 10 U/µL, 20µL 2 U/µL Phusion DNA Polymerase, 0.16µL Taq DNA Ligase 40000 U/µL, 860µL ddH_2O.

2.4.8. DNA sequencing

To confirm plasmid constructions, DNA sequencing was used. 5 µL of purified plasmid (80-100 ng/µL) was mixed with 5µL of desired primer (5 pmol/µL). Samples were sequenced by Eurofins-GATC. Sequences were analysed using Snap Gene software v.4.2 (GSL Biotech LLC).

2.4.9. Growth rate analysis

Growth rate analysis was performed using a Tecan F200 plate reader, which allowed optical density measurements at regular intervals, for a defined time, providing the required growth rate curve. Yeast cells were incubated overnight in a liquid culture prepared with appropriate medium. In the following morning, cells were re-suspended in fresh medium until OD_{600} = 0.1 and allowed to grow until OD_{600} = 0.4-0.6. After that a further cell re-suspension was performed to obtain OD_{600} = 0.05 to prepare the plates for the plate reader. Optical density measurements were taken every 6 minutes, over 11-36 hours. The software provided an Excel spread sheet with OD_{600} data of every measurement for every well. Analysis was performed using the following formula:

$$log_2 \frac{N_t}{N_0} = \alpha(t - t_0)$$

where N is the number of cells, t is time in hours and α is the growth rate. In a practical way, the number of cells was estimated by the OD_{600} value and = slope of $log_2 OD_{600}$ versus time (Hall et al., 2014).

2.5. Microfluidics, microscopy and flow cytometry

2.5.1. Microfluidics

The microfluidics SU-8 master moulds were made according to Fehrmann et al., 2013 and Jo et al., 2015 designs, using standard soft lithography techniques (collaboration with University of Warwick Physics Department, Dr. Polin's group). Polydimethylsiloxane (PDMS) and curing agent (Sylgard 184 kit - Dow Corning) were mixed in a 10:1 weight ratio and degassed under vacuum. Then the mixture was poured over the SU-8 master mould and cured at 80˚C for 2 hours to produce the microchannels. The PDMS piece was then removed from the master mould and inlet and outlet channels were punched. The PDMS piece was covalently bonded to a glass coverslip using a plasma cleaner (Harrick Plasma). Since this equipment requires low pressure to generate plasma, a RC.8D vacuum pump (D.V.P. vacuum technology) was used for 1-3 minutes to evacuate the air inside the chamber and was kept on until the end of procedure. Oxygen was the processing gas. High radio frequency (RF) was used for 1-2 minutes to create radicals in both PDMS chip and glass coverslip surfaces. After this time, atmospheric pressure was re-established by turning off the vacuum pump and slowly venting air into the plasma cleaner. The PDMS chip was immediately placed on top of glass coverslip and the assembled microfluidics device was placed on a heating block (60˚C-80˚C) (Fisher Stirring Hotplate – Fisher Scientific) for two hours.

2.5.2. Instrumental Assembly of Microfluidics Apparatus

Microfluidics device assembly for the preparation of experiments was performed as follows. To avoid damage to the microscope that could be caused by any possible medium leakage from the microfluidic chip, the glass coverslip was bound to a plate lid with an appropriate central circular aperture made to allow necessary space for the lenses, while avoiding any medium leakage to reach the microscope. The

microfluidic device was then placed on the Nikon TI-E Eclipse motorized wide-field epifluorescence microscope, inside a cage incubator (Okolab) that controls the temperature during the experiment. The medium reservoir was connected to a CellASIC® ONIX Microfluidic Platform, that controls the medium flow during the experiment. Next, using 1/16" ID / 1/32" OD PTFE tubing, the medium reservoir was connected to the chip inlet, the outlets were connected to a waste bottle and medium was flown into the microfluidic device to remove any undesired particle. After that the inlet was connected to a syringe containing an exponential-phase cell culture and, using a syringe pump (NE-300 Just Infusion™ Syringe Pump - New Era Pump Systems), with a flow rate of 10 - 20µL/minute, cells were injected into the microfluidic device. Once cells were injected, medium reservoir was reconnected to the chip inlet and the microfluidics apparatus was ready for time-lapse experiment.

2.5.3. Time-lapse Acquisition

High-resolution time-lapse microscopy of yeast cells growing in constantly flowing medium (1.0 psi) in the microfluidics chip installed inside a cage incubator (Okolab) at 30°C was obtained using a Nikon TI-E Eclipse motorized wide-field epifluorescence microscope equipped with EMCCD or sCMOS cameras (Andor) and a 60x oil immersion objective. Bright field or phase contrast images were acquired at 10-minute intervals, with GFP excitation (λ_{ex}= 488nm) performed every 60 minutes. The total time-lapse duration was 90 hours. A CellASIC® ONIX Microfluidic Platform was used to regulate and maintain the medium flow pressure.

2.5.4. Image Analysis

Images were processed using the Image J (v2.0.0-rc-66/1.52b National Institutes of Health) software package to count the number of daughter cells produced by a

single mother cell and to measure fluorescence intensity. Analysis of bud scar numbers was also performed using ImageJ.

2.5.5. Corrected Total Cell Fluorescence Calculation

When performing image analysis of time-lapse experiment, more than 100 cells for each strain were followed until their 10th budding process and the fluorescence intensity of these cells was measured when newborn and when 10 generations old. An outline was drawn around each cell and area, integrated density, mean fluorescence and minor and major axes of each ellipsoid shape were measured. Background readings were also performed. Corrected total cell fluorescence (CTCF) = integrated density – (area of selected cell × mean fluorescence of background readings) (McCloy, et al., 2014) was then calculated for each cell at the two different ages. Cell volume was calculated from 2D images by using minor and major axes of each cell at each time point to calculate the ellipsoid volume, as performed by Cookson et al (Cookson, et al., 2010). The formula is presented below.

$$V = \frac{4}{3}\pi abc$$

V is the volume and a, b and c are the ellipsoid semi-axes. The cells height was defined as equal to the minor axis. When larger cells had a minor axis greater than the height of the microfluidics chamber, the height of the cell was considered as the height of the microfluidics chamber (Cookson et al., 2010). The calculated CTCF values were then normalized by cell volume to estimate GFP concentration. Mean and standard deviation (SD) of normalized CTCF values were calculated. Additionally, normalized CTCF values that were outside an interval of mean +/- 3*SD were excluded to remove extreme events. Finally, the coefficient of variance (CV) was calculated to analyze gene expression noise.

2.5.6. Cell Wall Staining, Flow Cytometry Analysis and Cell Sorting

Protocol adapted from Yang et al., 2015. Yeast cells were cultured at 30°C overnight and were then diluted the next day to OD_{600} = 0.01– 0.02 and incubated for 8-10 h, until reaching OD_{600} = 0.4– 0.7. Cells were diluted once more in fresh medium to OD_{600}= 0.0001– 0.0002 and cultivated overnight. This 2-day cultivation prior to the experiment is important to better stabilize GFP expression. The very low dilution is important to keep cells always in exponential growth and avoid any influence of stationary phase cells on gene expression noise measurements. The following day, cells were diluted to OD_{600} = 0.1– 0.2 and incubated for 3-5 h to reach OD_{600} = 0.4– 0.7. A single sample was collected at a time to be analysed. The sample was sonicated for 5-15 seconds to free-up aggregates and analysed in a flow cytometer (BD Biosciences Fortessa) prior to staining (young cells). The remaining cells were harvested by centrifugation, washed with PBS, and the cell wall was stained for 10 minutes at 30°C during shaking incubation with 250µL of 26.7 mM Alexa 555-NHS ester/PBS solution. This staining allows us to differentiate mothers from daughter cells, since daughter cells synthesize a new cell membrane and cell wall, thus, not inheriting the surface dye. After staining, cells were washed twice with PBS, re-suspended in culture media, diluted to OD_{600} = 0.0001– 0.0002 and incubated at 30 °C for 16-19 h to allow the cells to replicate approximately 10 times. For 15 budding processes, cells were diluted to OD_{600} = 0.00001 – 0.00002 and incubated for 22h – 25h. After incubation, samples were collected one at a time, sonicated for 10 - 60 seconds to separate aggregated cells and analysed by flow cytometry. The BD Biosciences Fortessa flow cytometer was used to measure GFP (B488-530/30-A) and Alexa 555 (YG561-586/15-A) fluorescence emission signals. Flow cytometry data were recorded using the 'Area' option and exported from the acquisition program (FACSDiva) in the FCS3.0 format with a data resolution of 2^{18}.

For bud scar number analysis of 10-generation-old cells, a 400mL sample was collected and subjected to fluorescence activated cell sorting (FACS). A BD Biosciences FACSAria Fusion was used to measure GFP (B488-530/30-A) and Alexa

555 (YG561-586/15-A) fluorescence emission signals and sort cells according to their Alexa 555 fluorescence level (>10^3 arbitrary units (a.u.)).

2.5.7. WGA-conjugate scars staining

The protocol was adapted from Patterson & Maxwell, 2014. After FACS, selected cells were subjected to scars staining with Wheat Germ Agglutinin (WGA) CF-405S conjugate. The cells were collected by centrifugation and washed twice with PBS. Cells were stained with 250µL of 100µg/mL WGA CF-405S – PBS solution, protected from light, with gentle rocking at 30 °C for 30 minutes. Cells were then washed twice with PBS and used to prepare microscopy slides.

2.5.8. Microscopy analysis of stained cells

Cell-wall-stained and scar-stained cells were prepared for microscopy analysis using anti-fade mounting-medium, following the manufacturer's protocol. Images were acquired using a Nikon TI-E Eclipse motorized spinning disk confocal microscope equipped with EMCCD camera (Andor) and a 100x oil immersion objective. For scar-stained cells, multiple images were taken at different focal distances to build a composite image. Image J (v2.0.0-rc-66/1.52b National Institutes of Health) was used to perform image analysis.

2.5.9. Analysis of flow cytometry data

Analysis of raw flow cytometry data was performed as described by Newman (Newman, et al., 2006). We used R programming language scripts (using flowCore, flowViz and flowDensity Bioconductor packages) developed in our group by Dr. Xiang Meng to calculate statistics for each file (for the scripts, please refer to Chapter 10.7 and 10.8). To calculate the coefficients of variation (CV values), flow cytometry data files were processed as described for young cells:

1. The first and last 0.2 second of data were removed to minimize errors generated by unstable sample flow through the flow cytometer.
2. The bottom and top 2.5% of the FSC and SSC data were excluded to limit the influence of cellular debris and aggregated cells
3. For the remaining data, the FSC and SSC values of the highest density centre of the FSC–SSC scatterplot were calculated, and the distance of the i^{th} sample to the centre was determined:

$$\text{Distance i} = \sqrt{((\text{FSC i} - \text{FSC centre})^2 + (\text{SSC i} - \text{SSC centre})^2)}$$

4. The smallest and largest 0.5-1.0% of the GFP values situated within the defined radius centred at the highest density point of the FSC-SSC scatterplot were removed and the remaining GFP data within the defined radius were used to calculate the (percent) coefficient of variation:

$$\%\text{CV} = \left(\frac{\text{Standard deviation}}{\text{mean}}\right) \times 100$$

For the analysis of old mother cells, the bottom 3.0% and top 0.0-0.35% of the FSC and SSC data were excluded to limit the influence of cellular debris and aggregated cells, without excluding large old cells. Prior to the identification of the highest density point in the FSC-SSC scatterplot, data were subjected to another round of processing to select only red old cells (Alexa 555 signal above 10^3 a.u.). Using only the selected old cell data, the highest density point in the FSC-SSC scatterplot was calculated and the distance of the i^{th} sample to the centre was determined as the highest density point. The smallest and largest 0.5-5.0% of the GFP values situated within the defined radius centred at the highest density point of the FSC-SSC scatterplot were removed and the remaining old cells GFP data within the radius were used to calculate the (percent) coefficient of variation as described. When larger sample volumes were required to perform the experiment, a longer sonication time was necessary to free up aggregates. In such cases, more cell debris

and damaged cells accumulated, so that it was necessary to make a small adjustment in the exclusion threshold for the lowest GFP fluorescence values. The definition of gate radius in this study used the same rationale as Newman et al., 2006. The CV value decreases as the gate radius is reduced, until the CV becomes relatively constant, and a balance between a gate radius that yields the lowest possible CV value while retaining a sufficient number of cells for the analysis was considered in this study when defining the radius.

Chapter 3 - Microfluidics and the study of ageing

In 1959, Mortimer and Johnston performed the first study investigating *S. cerevisiae* longevity and demonstrated that although yeast cultures can be propagated indefinitely, individual yeast cells can only generate a limited number of daughters. The number of daughter cells a mother can produce is referred to as the replicative lifespan. When performing the study, Mortimer and Johnston used a micromanipulator, where yeast cells are streaked on solid growth medium spread on top of a coverslip and kept inside a temperature-controlled chamber. Under the microscope, daughter cells are separated from the mother cell by cutting thin slices of the growth medium, with this process being repeated until the end of the replicative lifespan. Although micromanipulation is still considered to be bread-and-butter for yeast ageing studies (Chen et al., 2016) and recently published studies have still used this methodology (McCormick et al., 2015), there are important imposed limitations. Micromanipulation is significantly laborious and time-demanding, consequently limiting sample size and impacting the statistical confidence of results (Chen et al., 2016). As an example, genome-wide studies of replicative lifespan were performed analysing only 5 mother cells per deletion strain (Kaeberlein and Kennedy, 2005; McCormick et al., 2015). To overcome these limitations, over the last decade research groups have been developing new microfluidic technologies that aim to permit semi-automated replicative lifespan studies (Koschwanez et al., 2005; Xie et al., 2012; Lee et al., 2012; Zhang et al., 2012; Fehrmann et al., 2013; Crane et al., 2014; Jo et al., 2015; Liu et al., 2015). Microfluidic devices feature sub-millimetric chambers and channels, and to create these extremely small patterns, a SU-8 mould, built using soft lithography, is required. SU-8 is a negative epoxy-based photoresist, used to thin-coat a silicon wafer in the initial steps of mould fabrication. The negative photoresist is exposed to UV light using a designed mask, causing the exposed area to cross-link, while the non-exposed area remains soluble and can be washed away during the development step, forming the desired sub-millimetric features. Once the mould is

finished, polydimethylsiloxane (PDMS), a clear, gas-permeable and bio-compatible elastopolymer, is cast on top, creating the desired microchannels and microchambers on the surface of the PDMS piece, which is then sealed onto glass coverslips (Chen et al., 2016), creating a device for controlled cell cultivation and observation.

3.1. Microfluidic devices to be used in this study

The main aim of this project was to explore the relationship between translation machinery activity, gene expression noise and ageing. Three *S. cerevisiae* strains were generated for this work: wild type, *tif4631*Δ and *tif4632*Δ, developed from the strain W303 (MATalpha ade2-1 ura3-1 leu2-3,112 his3-11,15 can1-100). I used these strains to investigate variations in gene expression noise during the ageing process as a function of imposed restriction on protein synthesis. Deletion of *TIF4631* gene, which encodes the eIF4G1 isoform (corresponding to 85% of the total eIF4G content; Firczuk et al., 2013) results in a major reduction in the rate of translation initiation (Firczuk et al., 2013). Removal of eIF4G2 (encoded by *TIF4632*) on the other hand, imposes only a small attenuation of translation initiation (Firczuk et al., 2013).

In order to study gene expression noise in these strains, I integrated into their respective genomes the fluorescent reporter yEGFP under the control of the P_{TEF1} promoter, a strong and relatively low noise promoter (due to the absence of TATA box in its sequence; Blake et al., 2006; Murphy et al., 2010), followed by the synthetic L0 5'UTR (Dacheux et al., 2017) (Figure 7). L0 5'UTR is a short, unstructured 5'UTR which has been used as an efficient and low noise 5'UTR in previous studies (Oliveira et al., 1993, Dacheux et al., 2017).

Figure 7: Illustration of the chromosome-integrated yEGFP reporter construct. P_{TEF1}, a strong, relatively low noise promoter controls the expression of yEGFP. 24 bacteriophage MS2 binding motifs in the 3' UTR can be used as targets for smFISH probes in future studies. The terminator used (T) is PGK1. For the integration plasmid map, please refer to Chapter 10.1.

Microfluidics is one of the techniques used in this PhD work to investigate the relationship between translation machinery activity, gene expression noise and ageing. An illustration of the experimental set-up assembled around the microfluidics apparatus is shown in Figure 8. A microfluidic chip is placed on an epifluorescence microscope, inside a temperature-controlled chamber, and each inlet channel is connected to a medium reservoir connected to a pump that controls the medium flow during the experiment. The outlet channels are connected to a waste bottle. After priming the microfluidic chip by flowing some media into it, cells can be injected into the chip, where they will be kept in a controlled environment with a constant flow of medium during the entire experiment. The microchambers are designed to retain the mother cell during the study, while the daughter cells can be either washed away by the flowing medium or retained in a chip with features that allow the daughter cell to be held without compromising the observation of the original mother cell. The time-lapse acquisition is controlled by software. This experimental set-up was found to be superior to the microdissection experiment, allowing the researcher to observe more cells in parallel over a shorter period of time. Moreover, unlike the standard microdissection method, this approach works with cells cultured in any liquid medium of choice, and also makes it possible to change the medium during an experiment, if necessary.

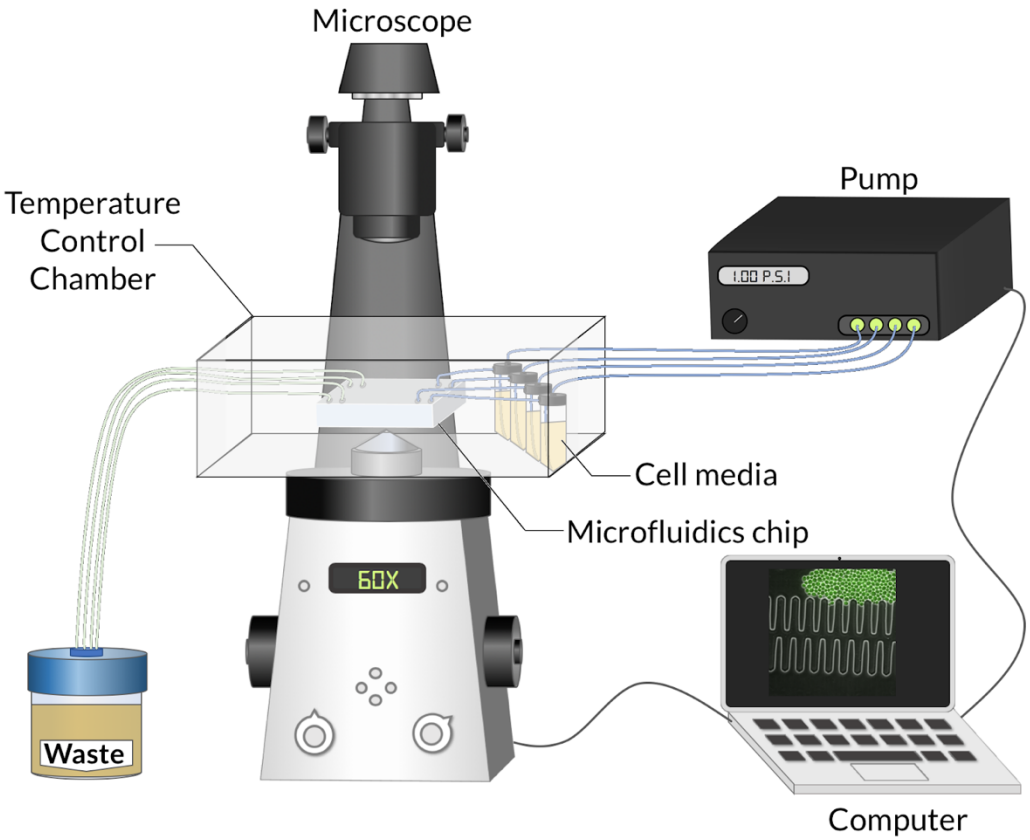

Figure 8: Experimental set-up for microscopy time-lapse studies using a microfluidic device. Overview of the apparatus used for yeast cell observation during the replicative lifespan. The microfluidic device is placed on an inverted epifluorescence microscope, inside a temperature-controlled chamber. Cells are loaded into the device and a constant flow of medium is generated by the pump. Image acquisition is managed automatically via software.

HYAA chip design

Initially, I used the HYAA (High-throughput Yeast Ageing Analysis) microfluidic device developed by Jo et al., 2015. This design features 16 parallel channels grouped into four modules and each channel contains 520 cup-shaped single-cell trapping structures, where the trap main opening, outlet opening and height measure 6µm, 3µm and 5µm respectively. The master mould was built according to the authors' design, using soft lithography, in collaboration with Dr. Marco Polin's group, from the University of Warwick Physics Department. PDMS was poured and

cured over the master mould to create the desired microchannels and cell-trapping units, as described in the Methods section.

Each one of the cup-shaped units is designed to trap one single mother cell and ideally retain it until the end of its RLS, while the daughter cells that bud off can be washed away through the main or outlet openings (Figure 9 A).

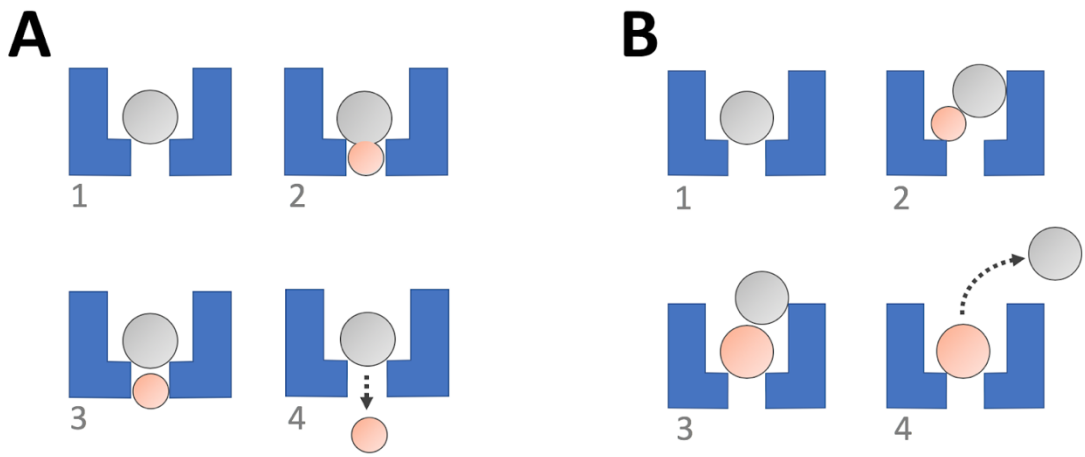

Figure 9: Scheme of HYAA microfluidic device. A: Ideal performance of the HYAA microfluidic device, with a mother cell (grey) trapped by each cup-shaped structure. Budding yields a daughter cell (orange) that is released through the appropriately sized gap in the lower part of each trap structure. **B:** Non-ideal performance of the HYAA device - the mother cell is levered out by the daughter cell and subsequently lost from the trap.

Although Jo et al., 2015 reported a retention rate of up to 92% for mother cells, during the experiments I frequently observed mother cells to be ejected by their daughter cells at variable points during the lifespan (Figure 9 B), therefore impairing the necessary observation of mother cells through a consistent number of generations, as can be observed in the images of Figure 10.

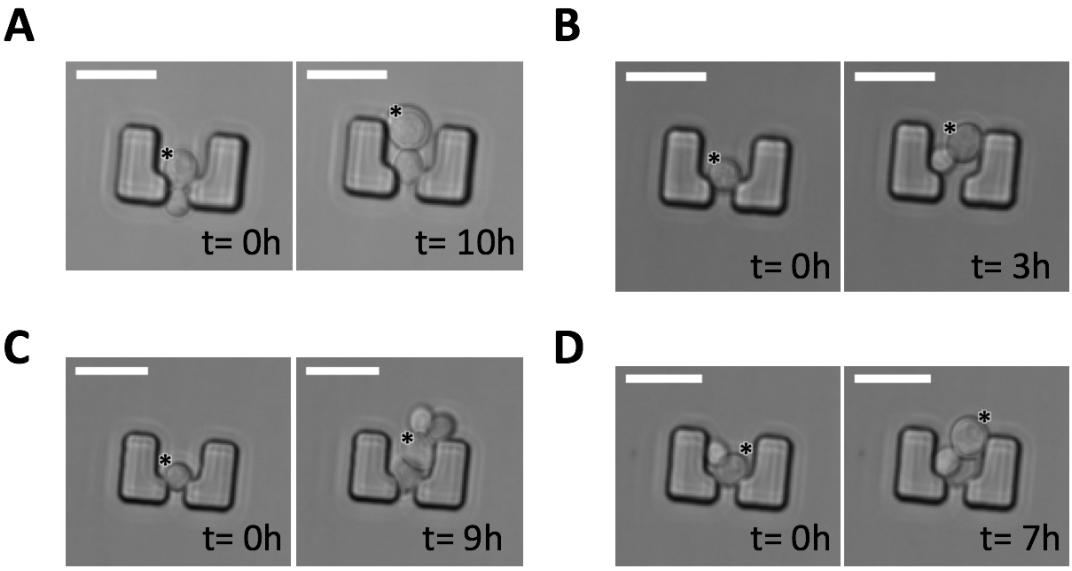

Figure 10: Time-lapse images of yeast cells in a HYAA microfluidic device. The images show the microfluidic design developed by Jo et al., 2015, featuring four trapped *S. cerevisiae* cells as they progress through the cell cycle. **A:** t=0h is the first image after cell trapping; this is followed by the time-point where the original mother cell (marked with *), after a few budding processes, was lifted up by a new daughter cell, a few imaging events before it was washed out through the main trap opening (10h). In the other three cases, the mother cell was pushed upwards by its developing daughter cell and lost after 3 hours (**B**), 9 hours (**C**) and 7 hours, respectively (**D**). Images were acquired at 15-minute intervals. Scale bars represent 10 μm.

Thus, to be able to study cells over the course of their ageing process and investigate gene expression noise, I needed a chip design that would allow the observation of the mother cells through a longer and more consistent period of time.

CLiC 2 chip design

As an alternative, I used a microfluidic device developed by the Charvin lab, in the *Institut de Génétique et de Biologie Moléculaire et Cellulaire*, France (unpublished data), and kindly provided to our group. This design was based on the Cell Loaded into a Cavity (CLiC) design published by the same group (Ferhmann et al., 2013).

This device was constructed high throughput to analyse a larger number of cells and/or strains, compared to the first CLiC design and features 10 parallel channels containing 320 elongated-cavity trapping structures, where the trap opening is 6μm wide, and chamber height is 3.3μm (Figure 11). With this design, whilst the cells multiply inside the chip, they start to occupy the trapping structures, allowing through this process the identification of a newborn cell. Additionally, due to the structure of this design, mother cells cannot be ejected from the trapping structures during budding processes, allowing them to be observed for a more consistent number of generations.

In Figure 11 is displayed an image of the elongated-cavity trapping units before injection of cells and Figure 12 illustrates how this design works.

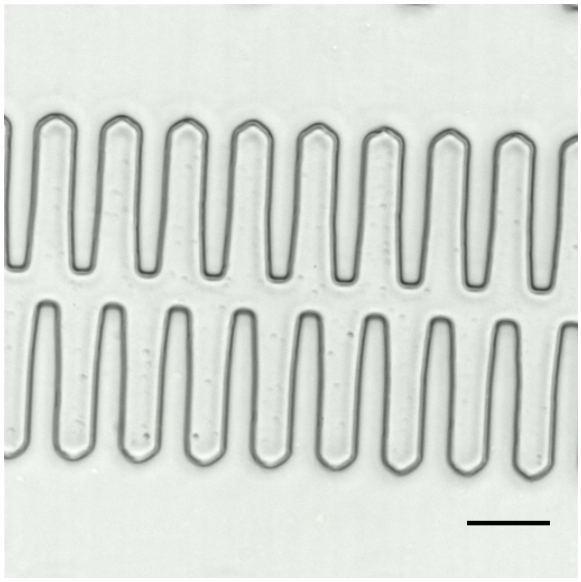

Figure 11: Image of the microfluidic device before cell loading. Microfluidic device developed by Charvin's group. Scale bar represents 20 μm.

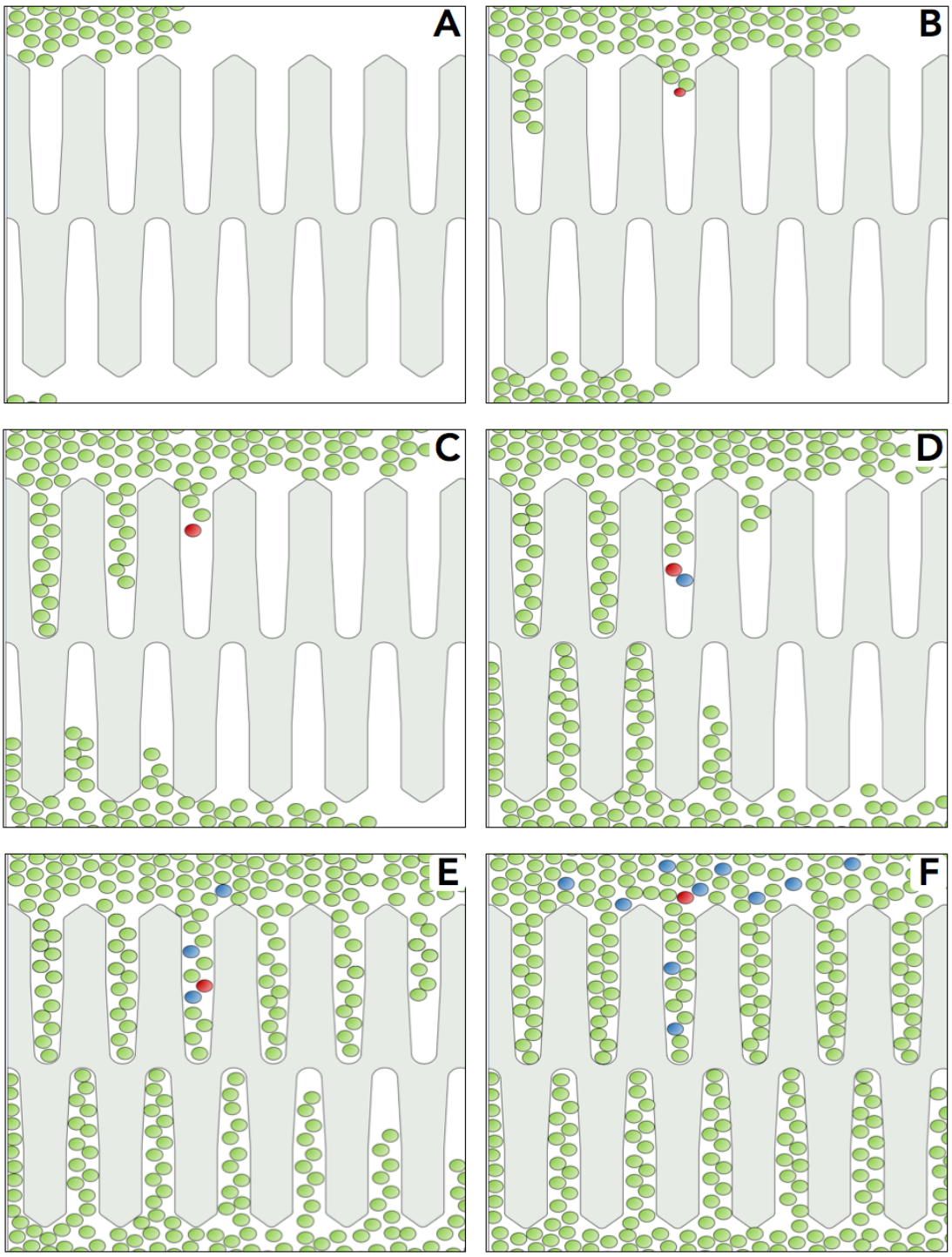

Figure 12: Illustration of the CLiC 2 microfluidic device after cell loading and its dynamics during time-lapse. After loading inside the device (A), cells continue to divide and start to occupy the traps (B,C,D). Red represents a newborn cell (B) that can be followed over its replicative lifespan (C, D, E, F). Blue cells represent the daughter cells generated by the red cell (D, E, F). Although cells move inside the device, this design still retain them for a more consistent number of budding processes.

3.2. Evaluating nutrients availability in the CLiC2 Chip

One concern with this design was that fresh medium might not be able to reach the bottom of the traps at a sufficient rate when they became crowded, which would make cells starve during the experiment and influence noise. To evaluate that, I performed two tests, assessing the cell doubling time and monitoring cells access to fresh medium by tracking P-body formation.

To investigate the cell cycle duration, after performing a time-lapse experiment, I used Image J software to measure the doubling time of 50 newborn wild-type cells dividing both inside and outside the elongated cavities. Two consecutive cell cycles were observed for each cell and the resulting doubling times were averaged. It was observed that the mean doubling time inside the elongated cavities was 117 minutes (Figure 13 A), and 100 minutes outside the elongated cavities (Figure 13 B). This made it evident that the doubling time was slightly increased inside the cavities, although it is important to note that the median doubling time was 7 minutes (6%) shorter, 110 minutes, and, as shown in the histogram the majority of the cells still displayed a normal doubling-time range (90-105 minutes), while a few manifested very long cell cycles (> 180 minutes). This increase in cell-cycle duration can be explained by the response of a small number of cells that occupied the crowded environment deep inside the elongated cavities.

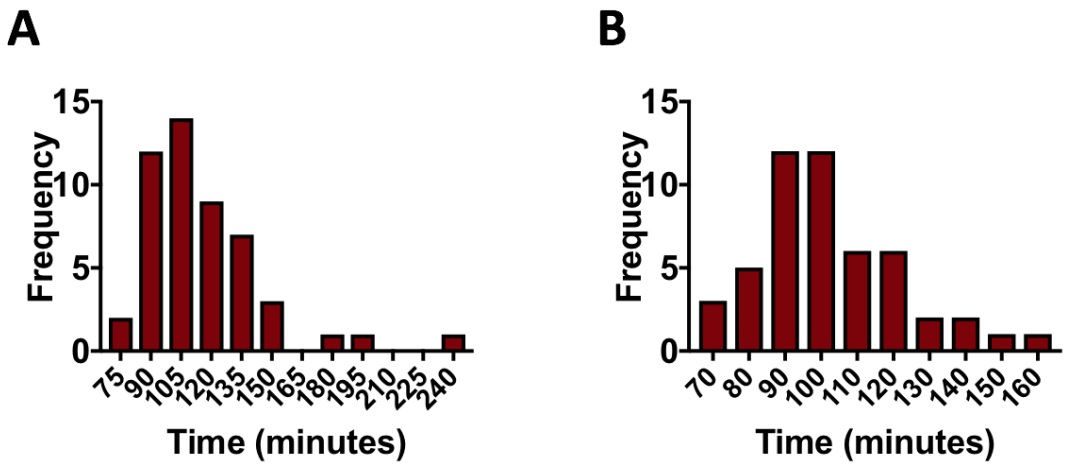

Figure 13: Analysis of doubling time inside and outside elongated-cavities. Two consecutive cell cycles were measured and doubling time average was calculated. **A**: Histogram of doubling time (minutes) for cells inside elongated traps. Mean = 117 minutes; Median = 110 minutes; n = 50. **B**: Histogram of doubling time (minutes) for cells outside elongated traps. Mean = 100 minutes; Median = 98 minutes n = 50.

In the second approach to evaluating how effectively cells were receiving access to fresh medium inside the elongated cavities, I used a strain containing a tagged P-body marker, since Teixeira et al., 2005 have demonstrated that there is a significant increase in the number of P-body foci in response to glucose deficiency. A strain containing an *EDC3::yEGFP* fusion gene was used to evaluate medium perfusion through these traps during a long time-lapse experiment. The time-lapse was set up as described in Materials and Methods, with the medium flow at a constant pressure of 1.0 psi, for 115 hours (longer than time-lapse experiment performed in this study). P-body foci were absent or rare during the majority of the experiment. Towards the very end of the time-lapse experiment, cells showed an increase in fluorescence, but the number of P-body foci was low (Figure 14). A positive control was not used in this experiment because a colleague in the group, Oliver Sinfield, studied the formation of P-bodies in this microfluidic device under different nutritional conditions. Using a fluorescent P-body marker, he observed the formation of P-bodies in response to glucose limitation (0.1%).

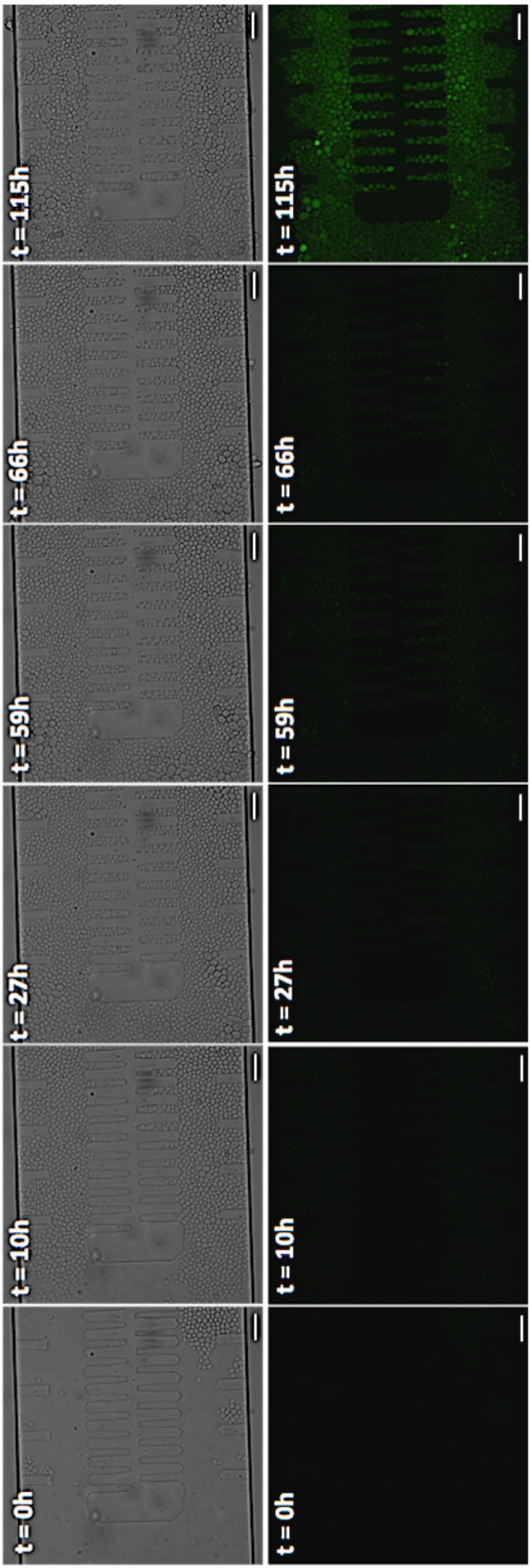

Figure 14: Time-lapse images of *EDC3::yEGFP* strain at different time points during the glucose availability test. Bright field images are shown on top; yEGFP images are shown below. Edc3 tagged with yEGFP is a P-body marker and a significant increase in P-body foci is expected if cells are subject to glucose starvation. Images show that P-body foci were absent or extremely rare for the majority of the experiment. An increase in fluorescence is observed towards the very end of the experiment, but the number of foci is low. Images were acquired at 12 minute-intervals for both bright-field and yEGFP channels. Scale bars represent 20 µm.

Taking into account the results from both of these control experiments, it is clear that there is no evidence of glucose starvation in cells growing within the elongated cavities, at least during the typical duration of the time-lapse experiments. There was, however, evidence of a small increase in the doubling time, indicating that some of the cells in the elongated cavities are subjected to glucose-limited growth, although this affected a minority of cells.

Chapter 4 - Microfluidics applied to the investigation of the relationship between ageing, translation and noise

Microfluidics allows the investigation, at the single-cell level, of variations in the expression of a fluorescent reporter over the ageing process. In this chapter, I discuss the application of the CLiC2 design in the study of *S. cerevisiae* cells. As described before (p58), I used the wild-type (WT), *tif4631*Δ and *tif4632*Δ strains, all carrying the genomic P_{TEF1}-yEGFP construct. The *tif4631*Δ strain has a reduced rate of translation initiation, while *tif4632*Δ strain has only a small attenuation (Firczuk et al., 2013), allowing thus the study of the relationship between translation machinery activity, gene expression noise and the ageing process.

First, I assessed if the autofluorescence of the cells is below the range of the reporter fluorescence. Using microscopy, I have measured the fluorescence intensity of all the three strains analysed in this study and compared to the autofluorescence of the parental strain not carrying the construct. I performed image analysis and calculated the normalized corrected total cell fluorescence as described in the Methods section (p52) (and later on this chapter) observing that the fluorescence intensity of the strains carrying the construct is at least 50-fold higher than the autofluorescence of the strain not carrying the construct. Therefore, the autofluorescence of the cells does not have a significant impact on the investigation of gene expression noise and measurements of coefficient of variance.

Using the CLiC2 microfluidics design (Figure 15), I followed, then, the wild-type, *tif4631*Δ and *tif4632*Δ strains expressing yEGFP for 90 hours. Phase contrast images were acquired every 10 minutes and GFP images every 60 minutes to avoid photobleaching.

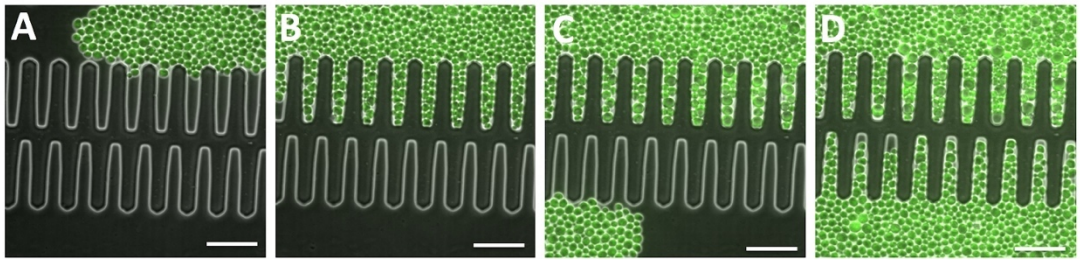

Figure 15: Time-lapse images of yeast cells in the elongated-trap microfluidics device. Yeast cells expressing y*EGFP* at different time points of a time-lapse experiment. A: The growing cell population expands into the microfluidic device and upper row of elongated traps (B). The cells are subsequently forced into the lower elongated traps (C, D). Images are a composite of phase contrast and yEGFP channels. Images were acquired 10 min apart for phase contrast and 60 min apart for yEGFP. Scale bars represent 20μm.

To perform image analysis, I have initially tried to use PhyloCell software (Ferhmann et al., 2013), to count budding processes and measure cell fluorescence, but this software was not suitable for data analysis due to a number of technical problems. CellProfiller (Carpenter et al., 2006) and Imaris v9.0 (BitPlane) software packages were also tested, but image segmentation was impaired because of the high cell density inside the device. Then, ImageJ (National Institutes of Health) was used to make manual counting of budding processes and to measure fluorescence level of single cells. I identified newborn cells and followed each of them until the 10^{th} budding process, repeating this process to analyse more than 100 cells, measuring the fluorescence intensity of newborn and 10 generation-old cells, for each strain. An outline was drawn around each cell and the area, integrated density, mean fluorescence and minor and major axes of ellipsoid were measured. Background readings were also performed. Corrected total cell fluorescence (McCloy et al., 2014) was calculated through the following expression:

CTCF = integrated density – (area of selected cell × mean fluorescence intensity of background readings)

The CTCF was then calculated for each cell at the two different ages. Cell volume was calculated from 2D images by using minor and major axes of each cell at each time point to calculate the ellipsoid volume, as performed by Cookson et al., 2010. The formula is presented below (Figure 16), where *V* is the volume and a, b and c are the ellipsoid semi-axes. The cells height was defined as equal to the minor axis. When larger cells had a minor axis greater than the height of the microfluidics chamber, the height of the cell was considered as the height of the microfluidics chamber (Cookson et al., 2010). The volume calculations were performed assuming ideal cell orientation (i.e. aligned horizontally) inside the microfluidics device. Since, under real conditions, cell alignment may not be perfectly horizontal, this will introduce an error into volume estimation for each individual cell since this would result in a smaller transversal cross section and thus an underestimate of the volume. However, since the resulting errors are expected to be relatively small and, moreover, they apply to all such experiments, they will not significantly affect the relative changes in CTCF values observed in this work.

$$V = \frac{4}{3}\pi abc$$

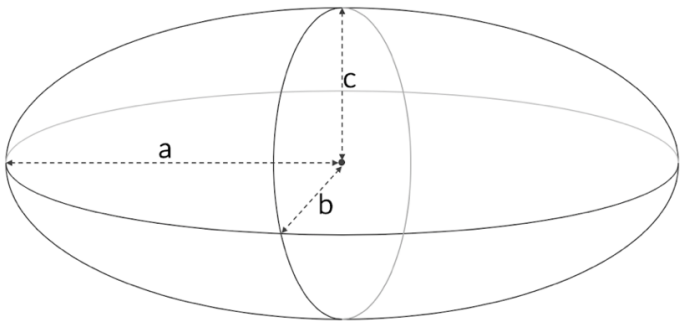

Figure 16: Schematic of ellipsoid volume formula used to estimate cell volume. Yeast cells were approximated to be an ellipsoid and their volumes were calculated using the ellipsoid volume formula where *V* is the volume and a, b and c are the ellipsoid semi-axes. The height of the cells was defined as equal to the minor axis. If larger cells had a minor axis greater than the height of the microfluidics chamber, the height of the cell was defined as equal to the height of the microfluidics chamber (Cookson et al., 2010).

As demonstrated by Kempe et al. (2014), cell-to-cell-variation is best represented by concentration, thus I normalized the calculated CTCF by the calculated cell volume to estimate yEGFP concentration. The workflow is illustrated in Figure 17.

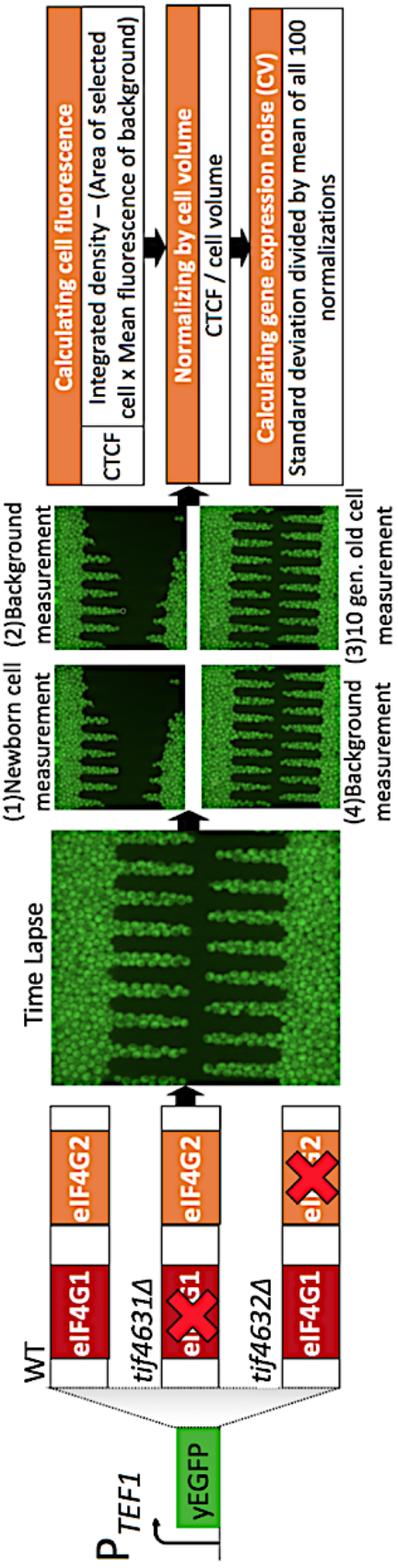

Figure 17: Workflow of image analysis using Image J. Cells expressing *yEGFP* were observed through time-lapse. Manual cell tracking was performed, in which a newborn cell was followed until the 10th budding process was completed; more than 100 cells were tracked per strain. Integrated density, mean fluorescence and minor and major axes of ellipsoid were measured, as well as background readings. Cell images are GFP-channel only. Corrected Total Cell Fluorescence (CTCF) values were calculated by the integrated density of the outlined cell minus area of outlines cell times mean fluorescence of background. CTCF was normalized to cell volume and the coefficient of variance was calculated for each strain analyzed.

A summary of the data obtained in this part of the study can be seen in Figure 18, where A shows, for each strain, the level of noise in young cells (0 - 1 generation) and B shows, for each strain the level of noise in 10-generation old.

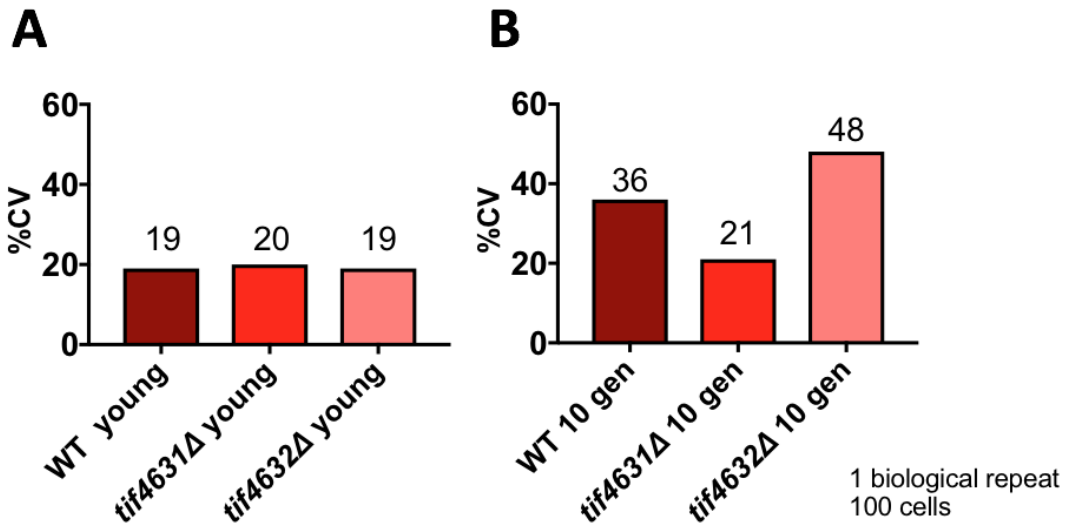

Figure 18: Gene expression noise of young and 10-generation-old cells. For each strain, fluorescence heterogeneity was measured for newborn cells and for 10-generation-old cells and the CV% values for the respective strains are represented in the plots A and B.

These data obtained using microfluidics technology and image analysis show that cells manifested an increase in gene expression noise as they age. Interestingly, the *tif4631Δ* strain shows the lowest level of noise increase during the ageing process. Since this set of results includes one biological repeat, statistical analysis of significance cannot be applied, as stated in Vaux, 2012. Although statistical analysis is not performed at this stage, the results obtained here were confirmed using flow cytometry analysis, as presented in Chapter 6, whereby multiple biological repeats and full analysis of statistical significance were carried out.

As mentioned earlier, this strain has decreased translation activity since the translation initiation factor eIF4G1 is absent. McCormick et al. (2015) have reported that this strain has a longer lifespan. Together, these facts point to a relationship between ageing, translation and gene expression noise.

Although this set of results constitutes just part of the results reported in this PhD work, it is worthwhile to consider a few points at this stage. To our knowledge, we are the first group to investigate the relationship between ageing, translation and noise. However, the relationship between ageing and gene expression noise has been examined previously. Bahar et al (2006) investigated gene expression noise in young and old cardiomyocytes using real-time PCR. They measured the transcriptional noise variation for two protease-encoding genes, seven housekeeping genes, three heart-specific genes and three mitochondrial genes. They found increased transcriptional noise in old cardiomyocytes for all nuclear genes analysed, which is consistent with my results. Newlands et al. (1998) and Martinez-Jimenez et al. (2017) also demonstrated that gene expression noise increases during the ageing process. Although a number of papers have shown an increase in gene expression noise during the ageing process, one paper has reported that gene expression noise decreases over the lifespan. Liu et al (Liu et al, 2017) used microfluidics to investigate yeast cell-to-cell variation in gene expression noise of P_{GAL} promoter regulated yellow fluorescent protein (YFP), finding that the stochasticity in gene expression noise decreased during the ageing process. Disagreements with the results obtained in my work can be explained by differences in the strategies used to analyse gene expression noise. Liu et al used the regulatable P_{GAL} promoter for their study, while I used the strong, constitutive P_{TEF1} promoter to control the expression of a fluorescent protein. Concentration and composition of carbon sources used could also be behind discrepancies in the old cells level of noise. Liu et al used a combination of 0.2% glucose and 0.5% galactose, while in this research I used 2% glucose. Consistent with this interpretation is the fact that, in another publication from the same group (Sarnoski et al., 2018), the authors have reported an age-dependent increase in the gene expression noise from a constitutively expressed construct (P_{TEF1}-ssGFP).

Chapter 5 - An innovative strategy for the analysis of gene expression noise during the ageing process

Although microfluidics combined with microscopy and image analysis is a powerful tool to investigate different aspects of the ageing process, I wanted to develop an alternative method for use in studies of the relationship between ageing, protein synthesis and gene expression noise. While the combination of microfluidics and image analysis provides a useful approach to studying the ageing process, problems can arise, for example when an automated analysis functions imperfectly because of cell crowding.

Flow cytometry is a robust technique and one of the standard methods to study gene expression stochasticity**,** being widely used to investigate variations in the expression of a fluorescent reporter (Newman et al., 2006; Knijnenburg et al., 2011). Still, there is no existing methodology that allows the concomitant investigation of gene expression noise during the ageing process. Therefore, I decided to apply a cell wall staining strategy to allow the use of flow cytometry in the study of how gene expression noise varies in yeast cells over the ageing process. This innovative strategy can reduce the time required to perform experiments and also the time required for data analysis, overcoming some of the challenges encountered when using other methods

5.1. Why use cell wall staining?

To use flow cytometry to measure yEGFP expression across the ageing process of a cell population and estimate variations in gene expression noise, I needed a way to distinguish old cells from young cells. Based on the work of Yang, et al., 2015, I started to develop a new strategy to study gene expression noise during the ageing process using Alexa 555-N-Hydroxy-Succinamide ester dye (Alexa 555-NHS ester)

to stain the cell wall and differentiate mother from daughter cells. NHS ester conjugated dyes bind covalently to lysine and arginine residues since these amino acids have primary amines in their side chains. Once bound to lysine and arginine residues, the dye remains attached at the mother cell wall, while the daughter cells, when synthesizing *de novo* their cell wall during the budding process, inherit minimum or no dye. Thus, mother cells display a high-intensity Alexa 555 signal, while daughter cells display a weak red fluorescence signal.

At this stage of the study, the same strains were used to continue the investigation: Wild type (WT), *tif4631*Δ, *tif4632*Δ, all with the fluorescent reporter yEGFP under the control of P_{TEF1} promoter (Dacheux et al., 2017) integrated into their genomes. Therefore, this new strategy allows the separation of mother data from daughter data in the flow cytometry analysis and thus the study of the relationship between ageing, translation and noise.

5.2. Measuring the efficiency and specificity of the staining process

To evaluate the effectiveness of the staining strategy, I examined the stained cells using microscopy and flow cytometry.

After performing the cell-wall staining protocol, as described in the Methods section, I examined the cells under the microscope, observing that all cells were successfully stained. When examining the cells using flow cytometry, I observed a clearly defined Alexa 555 fluorescence intensity peak, fully distinguishable from non-stained cells (Figure 19). This demonstrates that using this strategy I can successfully stain the cell wall of yeast cells and differentiate stained and non-stained populations when investigating them using flow cytometry.

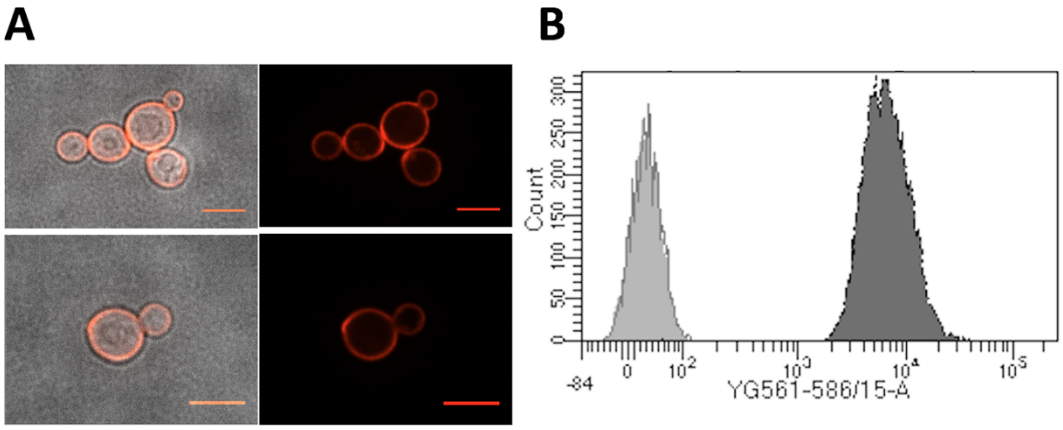

Figure 19: Yeast cells after the cell wall staining procedure using Alexa 555 NHS ester. A: Microscopy images of yeast cells. Left panel: composite of bright-field and red channels; right panel: red channel only. Scale bars represent 5µm. **B:** Flow cytometry analysis of stained cells reveals the distribution of fluorescence intensity across the population of stained cells. The light grey peak shows fluorescence intensity of unstained cells.

In order to check whether daughter cells would inherit a comparatively small number of dye molecules and thereby be readily distinguishable from the stained mothers after one doubling time, I examined cells incubated for two hours, sufficient time to allow them to recover from the staining protocol and go through one cell cycle. Again, I inspected cells under the microscope and performed flow cytometry analysis, observing that daughter cells do indeed inherit a minimal number of dye molecules and are readily discernible from their mother cells, displaying a distinct and much weaker fluorescence intensity peak, as can be seen in Figure 20.

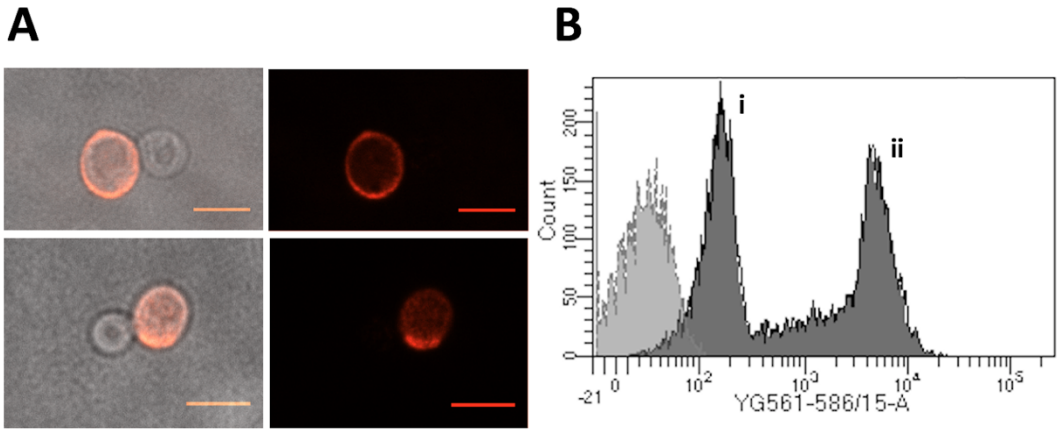

Figure 20: Yeast cells 2 hours after the cell wall staining procedure using Alexa 555 NHS ester. **A:** Microscopy images show a red mother cell and a non-stained daughter cell. Left panel: composite of bright field and red channels; right panel: red channel only. Scale bars represent 5µm. **B:** Flow cytometry analysis showing that red mother cell fluorescence (ii) is readily distinguishable from non-stained daughter cell fluorescence (i). The light grey peak shows the fluorescence intensity distribution of unstained cells.

I continued to examine the cells and the same trend was observed after the second doubling time, where daughter cells again inherited a minimal number of dye molecules and were clearly distinguishable from old cells (Figure 21).

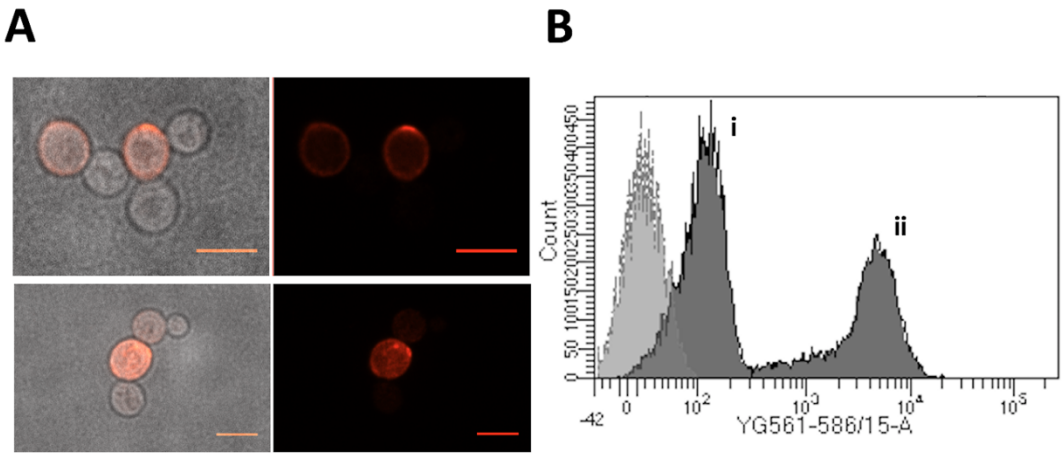

Figure 21: Yeast cells 3.5 hours after the cell wall staining procedure using Alexa 555 NHS ester. **A:** Microscopy images show red mother cells and non-stained daughter cells after 2 doubling-times. Left panel: composite of bright field and red channels; right panel: red channel only. Scale bars represent 5µm. **B:** Flow cytometry analysis showing old (ii) and young (i) cell fluorescence intensity peaks after 2 doubling-times. The light grey peak shows the fluorescence intensity distribution of unstained cells.

Progressing in the observations, flow cytometry analysis demonstrated that old cells continue to display a high-intensity fluorescence distribution after five doubling-times, remaining clearly identifiable and distinguishable from daughter cells (Figure 22 A). As a final test, I verified the efficiency of the staining method by analysing and sorting 5 generation-old cells.

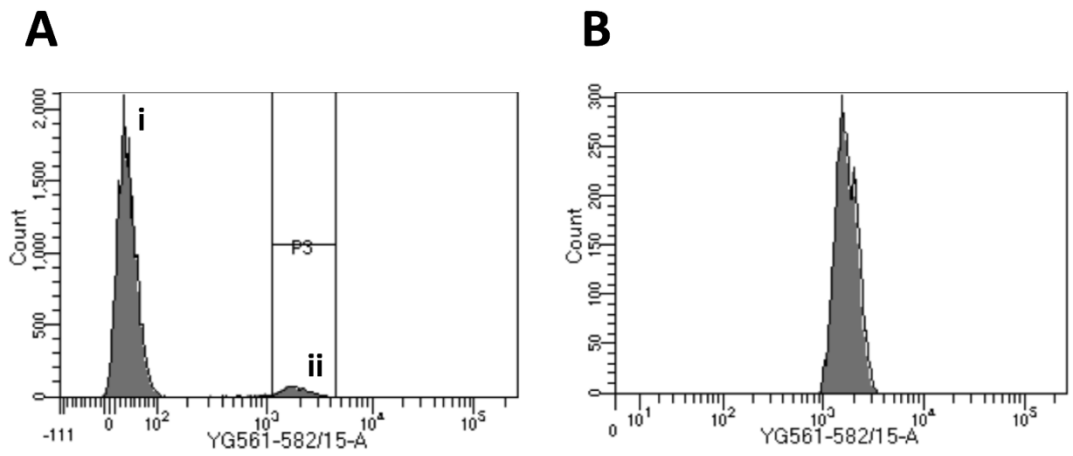

Figure 22: Verifying cell sorter efficiency in selecting cell wall stained cells. A: A culture of cells was subjected to fluorescence-activated cell sorting (FACS) after the equivalent of 5 average-doubling-times. Sorting was triggered in response to Alexa 555 signal intensity. **B:** After FACS, the sorted cells (ii) were reanalyzed to verify efficient sorting of mother cells.

Red mother cells were successfully sorted (Figure 22 B), what further demonstrates that this staining strategy efficiently allows the differentiation of old from young cells.

Therefore, when applying cell wall staining using a NHS-ester fluorescent dye, I can clearly differentiate old mother and young daughter cells, which will thus allow me to separate old cell data from young cell data when continuing the investigation of the relationship between ageing, translation and noise in even older cells. This new strategy allows more biological repeats to be performed in a shorter period of time and requires a less laborious data analysis, which can allow, in future studies, high-

throughput analysis of other genes that might influence gene expression noise during the ageing process.

Chapter 6 - Cell wall staining combined to flow cytometry to study the relationship between ageing, translation and noise

To obtain information about gene expression noise in young cells, I routinely measure yEGFP fluorescence in cells of an exponentially growing culture, where approximately 80% of the cells are newborn (have never budded before) and 12% have budded once (Jo et al., 2015; Lee et al., 2012). This first measurement gives information about the heterogeneity of a very young population. To follow cells through their ageing process, as discussed in chapter 5, I performed cell wall staining with Alexa 555-NHS ester and incubated cells overnight. After multiple generations, I measured yEGFP and Alexa 555 signals and separated red mother cell data to obtain information about gene expression noise in old cells.

To further confirm the age of the cells analysed I performed bud scar staining using Wheat-Germ-Agglutinin (WGA) conjugated to CF405S, a blue fluorescent dye. WGA is a lectin that binds to N-acetylglucosamine, the monomer unit of the polymer chitin (Burger and Goldberg, 1967). Bacon et al in 1966 and Cabib and Bowers in 1971 demonstrated that each bud scar is a crater-like ring, with its rim mainly composed of chitin. Therefore, WGA fluorescent conjugate staining successfully allows the assessment of how many daughters a specific mother cell has produced.

Figure 23 summarizes the workflow.

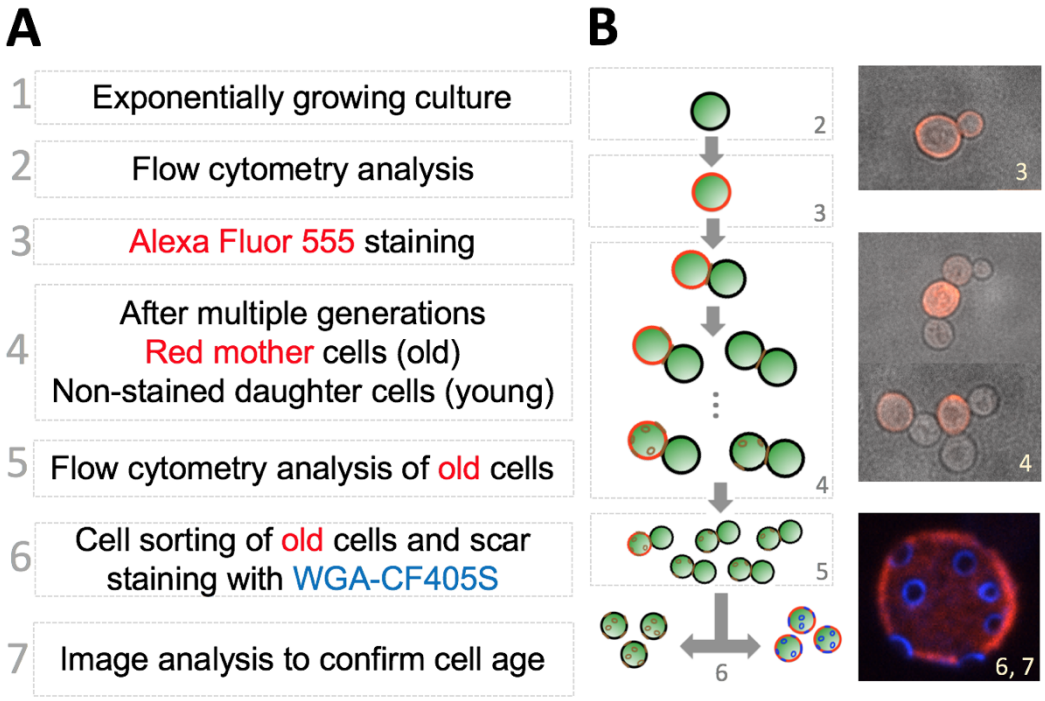

Figure 23: Workflow of flow cytometry analysis combined with cell wall staining to measure gene expression noise. **A:** A sample of an exponentially growing culture of transformed cells is analysed in a flow cytometer to measure GFP signal to obtain information about noise in a young population (2). Alexa 555 NHS ester cell wall staining is then performed (3) and, after overnight incubation (4), samples undergo flow cytometry analysis to measure GFP expression (5). The Alexa 555 signal is used to distinguish old mother from young daughter cells. Old cells are red and have a high-intensity Alexa 555 signal. Young cells are distinguishable from the old population because they have a low-intensity red signal. Old mother cells are collected using fluorescence activated cell sorting and undergo bud-scar staining using wheat-germ-agglutinin-CF405S dye (blue) (6). Images are then analyzed to confirm cell age (7). **B:** The illustrations follow the steps of this new methodology, showing cell wall staining, division during the incubation time and bud scar staining. The upper three images are composites of bright-field and red channels; the last image is a composite of red and DAPI (blue) channels and shows stained bud scars.

The goal at this stage of the study was to estimate how intrinsic noise varied during the ageing process, and how this could be influenced by the absence of either eIF4G1 (*tif4631Δ*) or of eIF4G2 (*tif4632Δ*) translation initiation factors.

Since a great part of the extrinsic gene expression noise is linked with variations in cell size, shape and cell-cycle stage, I decided to use the flow cytometry gating strategy based on forward (FSC) and side scatter (SSC) parameters, as described by Newman et al., 2006 (and used in the work performed by Dacheux et al., 2017 and Meng et al., 2017) to reduce the influence of extrinsic factors on noise.

In flow cytometry, FSC gives an estimate of cell size and SSC gives an estimate of cellular complexity (*e.g.* granularity and internal structures). Discrepancies in these physical cellular characteristics correlate with disparities in cell shape, size and cell-cycle stage, what masks the intrinsic heterogeneity (Knijnenburg et al., 2011; Newman et al., 2006).

In the FSC-SSC gating analysis used in this study, the centre is defined at the highest cell density point of the FSC – SSC scatterplot, whereby gates are defined according to cell distance to this central point. This gating strategy, therefore, allows the analysis of subsets of cells that are increasingly homogeneous in size and complexity. A common means to exclude cell aggregates (or doublets) in flow cytometry analysis is to use FSC pulse width (FSC-W) data. However, the gating method described by Newman and colleagues can also be used to exclude aggregates/doublets from the results. In additional work, it was found that applying the analysis of Newman et al. (2006) to just the singlet cell subpopulation (as identified using FSC-W data) yielded very similar values of estimated intrinsic noise to those obtained with the wider cell population (please refer to Chapter 10.2).

An illustration of the gating radius procedure can be seen in Figure 24 (modified from Meng et al., 2017).

Raw flow cytometry data were processed to eliminate events that were not representative of the population, as described in Materials and Methods. Then, the gating radius strategy was applied, with the centre being the highest cell density point of the FSC-SSC scatter plot, as mentioned.

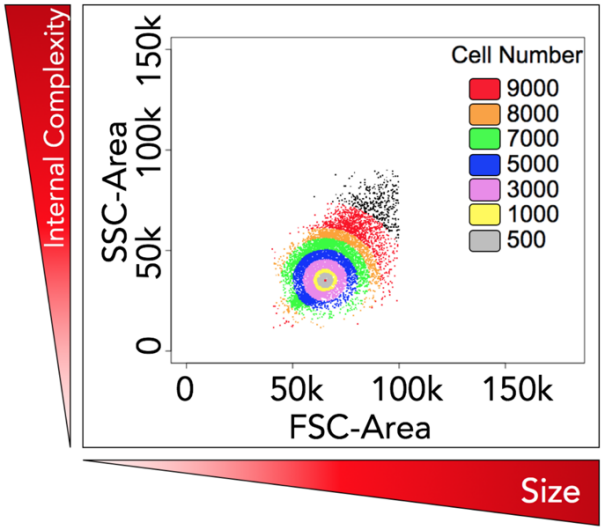

Figure 24: Illustration of gating radius procedure. Figure modified from Meng et al., 2017. Subsets of cells are defined and display increased homogeneity, reducing the influence of extrinsic noise factors. Centre of gating radius is defined as the highest cell density point.

The results from young cell analysis performed in triplicates showed that the *tif4631*Δ strain displayed the highest fluorescence intensity, when compared to WT and *tif4632*Δ, and also the lowest level of noise, as observed in figure 25. Although the level of fluorescence of *tif4631*Δ strain is higher, a Mann-Whitney test showed that this difference is not statistically significant when compared to the level of fluorescence of WT and *tif4632*Δ strains ($p > 0.05$). Statistical analysis of the strains' CV values was performed and will be discussed in Figure 32.

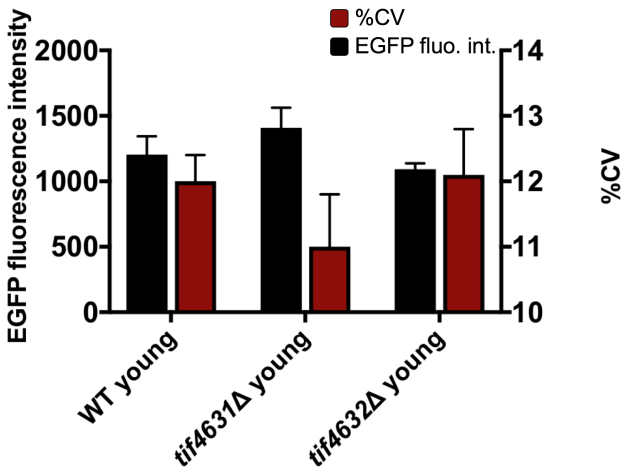

Figure 25: Analysis of yEGFP fluorescence intensity and coefficient of variance for young cells. Three experiments were performed per strain. Black bars represent fluorescence intensity. Whiskers show standard deviation of the mean fluorescence measured in each experiment. The coefficient of variance was calculated from flow cytometry data and is represented in dark red bars, with values indicated above. Whiskers show standard deviation of CV values for the three experiments.

Nevertheless, it is important to explore whether the estimated CV value was in some way directly linked to the response of the flow cytometer photomultiplier to the level of fluorescence intensity. In order to test this at a technical level, I reduced the flow cytometer photomultiplier (PMT) voltage in order to attenuate the *tif4631*Δ mean yEGFP fluorescence intensity (the highest) to the level of the *tif4632*Δ mean yEGFP fluorescence intensity (the lowest). As can be observed in Figure 26, reducing *tif4631*Δ mean fluorescence intensity in this way slightly reduced %CV, instead of increasing it, which, indicates that there is no significant correlation between mean fluorescence intensity and the observed noise values. Thus, these data indicate, that the flow cytometer does not artificially generate higher CV values at lower fluorescence intensities and the CV values differences in between strains result of biological noise rather than technical noise.

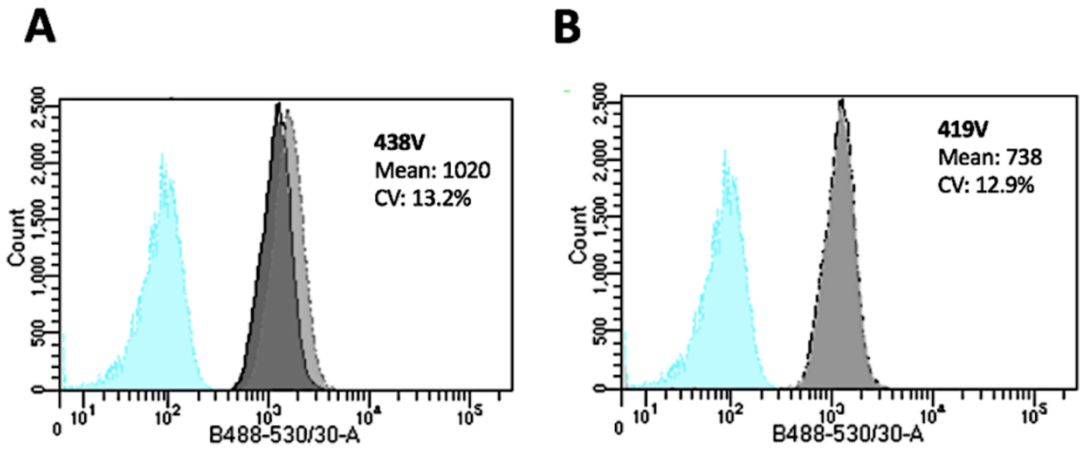

Figure 26: Addressing technical questions related to flow cytometry. This control experiment demonstrates that lower mean fluorescence intensity does not influence the observed noise values significantly. **A**- *tif4631Δ* strain (light grey) displays the highest mean fluorescence intensity compared to the other strains analysed, whereas *tif4632Δ* (dark grey) displays the lowest mean fluorescence intensity compared to the other strains analysed. **B -** Reducing *tif4631Δ* detected mean fluorescence intensity to the same level of *tif4632Δ* (by reducing the photomultiplier voltages) does not change the observed noise values significantly. Each plot displays the mean fluorescence intensity and CV value for the subset of cells identified by the gating radius set at 2000 a.u. Strains analysed carry the genomic P_{TEF1}-yEGFP construct (light grey and dark grey). The host strain autofluorescence (light blue) is of relatively low intensity relative to that of strains carrying the yEGFP construct and therefore does not significantly influence the experimental estimates of CV.

Knowing that the CV values are not artifactually influenced by the induced fluorescence intensities, I proceeded with the analysis of old mother cells. As described before (p79 and p80), overnight incubation allowed the cells to divide approximately 10 times before the examination using flow cytometry. Raw flow cytometry data were then subjected to processing to eliminate events that do not represent the population characteristics of viable cells. Moreover, for the old cells, another round of processing was performed prior to identifying the highest density point and performing gating radius strategy. In this step, cells displaying an Alexa 555 fluorescence signal equal to or higher than 10^3 a.u. (old stained mother cells) are identified and selected for further analysis, as can be observed in Figure 27.

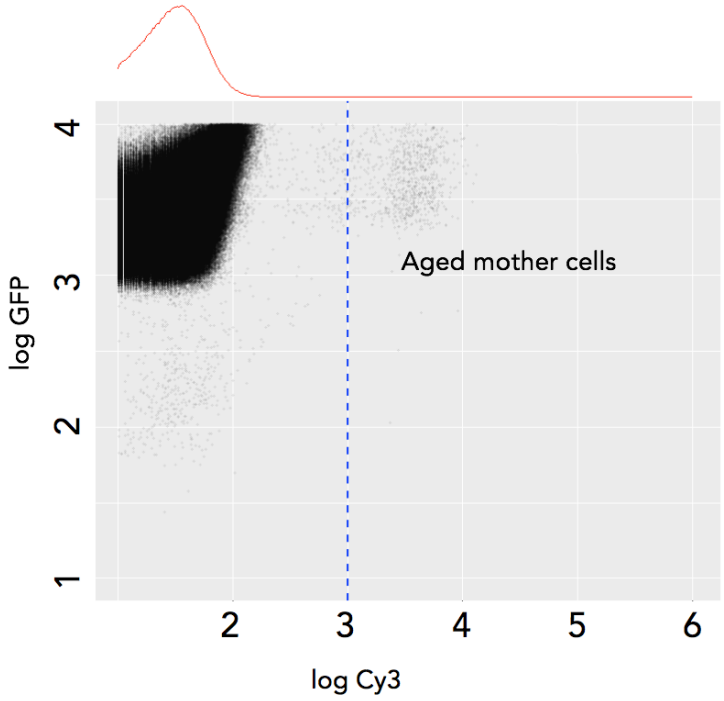

Figure 27: Illustration of the procedure to select only stained old cells. Cells displaying Alexa 555 fluorescence intensity equal or higher 10^3 a.u. are successfully identified in culture and are selected for further analysis to study gene expression noise. Dashed line represents selection threshold.

This additional step successfully identifies the old mother cells, originally stained at the beginning of the protocol, selecting them for the analysis of gene expression stochasticity in old cells.

In parallel to flow cytometry analysis of old cells, I performed fluorescence-activated cell sorting (FACS) to further verify the old cell selection efficiency and to confirm the age of the cells analysed. Cell sorting was performed using the same selection parameters and cells displaying Alexa 555 fluorescence intensity equal to or higher than 10^3 a.u. were collected. Selected cells were subjected to the bud scar staining procedure using WGA-CF405S conjugate and were examined using confocal microscopy in multiple focal planes. The stained bud scar can be observed in Figure 28.

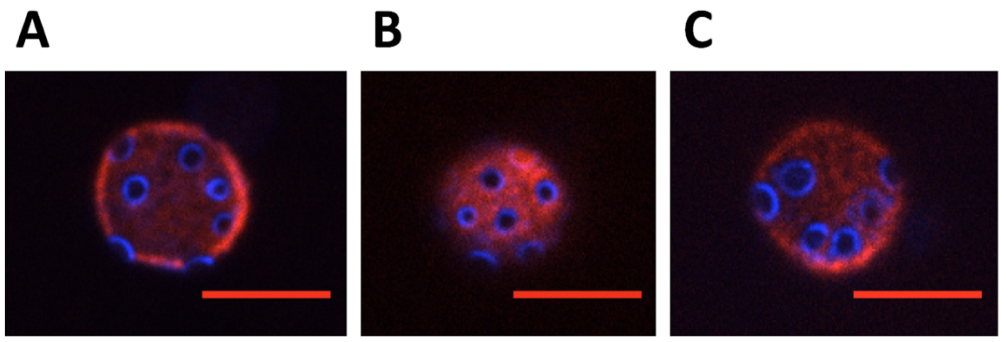

Figure 28: Yeast bud scars stained with WGA-CF405S. Old yeast mother cells that had been sorted according to Alexa 555 signal intensity were subjected to bud-scar staining using wheat germ agglutinin conjugated to CF405S, a blue fluorescent dye. Each blue ring identifies a bud scar formed after the generation of a daughter cell. **A**, **B** and **C** show individual cells in different focal planes. Images are composites of red (Alexa 555) and DAPI channels. Scale bars represent 5μm.

Image analysis and manual bud scar counting were performed using Image J software. A threshold of a minimum of 5 scars was applied since only 3 cells with four or less scars were observed during the analysis and they were normally not cell-wall stained, therefore they could be the result of very rare cells that were wrongly selected during the cell sorting procedure. Alternatively, cells born during the cell sorting procedure could also display a small number of bud scars that should not be included in this assessment.

The distribution of the age of cells analysed for each strain can be observed in the histograms (Figure 29). The mother cells analysed displayed an average of 11-12 budding events. Taking into account the time taken by the FACS analysis to select the rare stained cells in the population at room temperature, this is consistent with an average age of at least 10 generations at the time point that the cells were prepared for sorting. This confirms that the analysis procedure successfully selects cells at the expected age, whereby natural variation in the cell-cycle duration of individual cells results in a distribution of completed budding events.

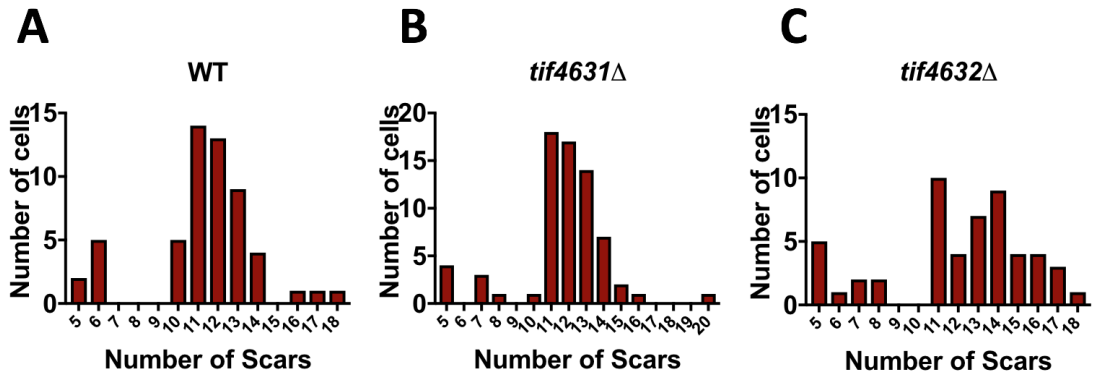

Figure 29: Distribution of the number of bud scars of selected cells. Using confocal microscopy, bud scars of individual cells stained with WGA-fluorescent conjugate (excitation at 405 nm and detection using 447/60 nm filter) were counted. Plots show the bud scar count for (mother) cells pre-selected by FACS. **A:** n = 55, average = 11.4. **B:** n = 69; average 11.7. **C:** n = 52; average 12.1.

Some ages were not observed during the bud scar number analysis. This could be due to the relatively small sample size, which was to be expected because stained old mother cells are rare in the population. Since the main objective was to confirm the average age, further bud scar experiments were not performed. A Mann-Whitney test performed for these data confirmed that the age distribution of the *tif4632*Δ strain is different from the age distribution of the WT strain, although the p-value is high (p= 0.047). When the *tif4632*Δ data were compared with the tif4631Δ data, the Mann-Whitney test showed that there is no difference in the age distribution between strains (p= 0.13). When WT was compared with *tif4631*Δ the test showed no difference in the age distribution between strains (p= 0.29).

When performing the analysis of the old cells, the highest density point was identified in the FSC-SSC scatterplot and the gating radius strategy was implemented.

As can be observed in Figure 30, the highest density point of the old cells (red dot) was slightly shifted relative to the position found with the young cells population

(dark blue area), which is expected since older cells are larger and more complex than young cells (Jo et al., 2015; Yang, et al., 2015).

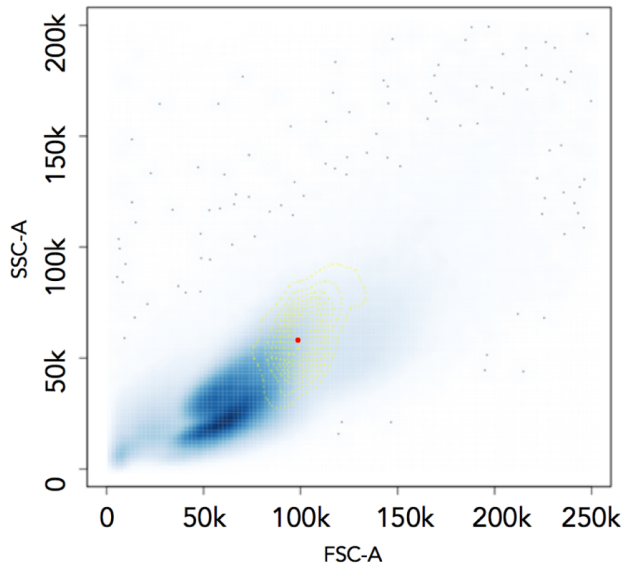

Figure 30: Example of highest density point and gating radius strategy in an old cell population. Central point (red) is located at the highest density region of the old cell population. Old cells are larger and more complex than young cells (dark blue area). The FSC-SSC scatterplot shows two subpopulations among young cells. One possible explanation for this might be the presence of budding cells, since the major difference between the two populations is the level of complexity. However, other forms of heterogeneity can contribute to a distribution of this kind, for example the presence of a variable cellular content of vacuoles.

Once the gating strategy is performed, the gating radius to be chosen for the analysis of the %CV was defined following the same rationale as Newman et al., 2006. As the gating radius decreases, cells become increasingly homogeneous in size and complexity, reducing the influence of extrinsic factors on the CV value, which becomes fairly stable, allowing an estimation of the intrinsic noise. A balance between the smallest CV while maintaining a sufficient number of cells is what defines the gating radius used to obtain the CV value. For the analysis of young cells, 50,000 events were measured and a gating radius of 2k was used to estimate the intrinsic noise (Figure 31 A). For the analysis of old cells, millions of events were measured to compensate for the small proportion of old (stained) cells in the culture.

Due to the challenge of this analysis, since the proportion of 10 generation-old cells in the culture is very small, and due to old cells behaving differently in different strains, the gating radius was defined individually and followed the rationale of choosing the smallest CV value, while including a sufficient number of cells for the analysis (Figure 31 B).

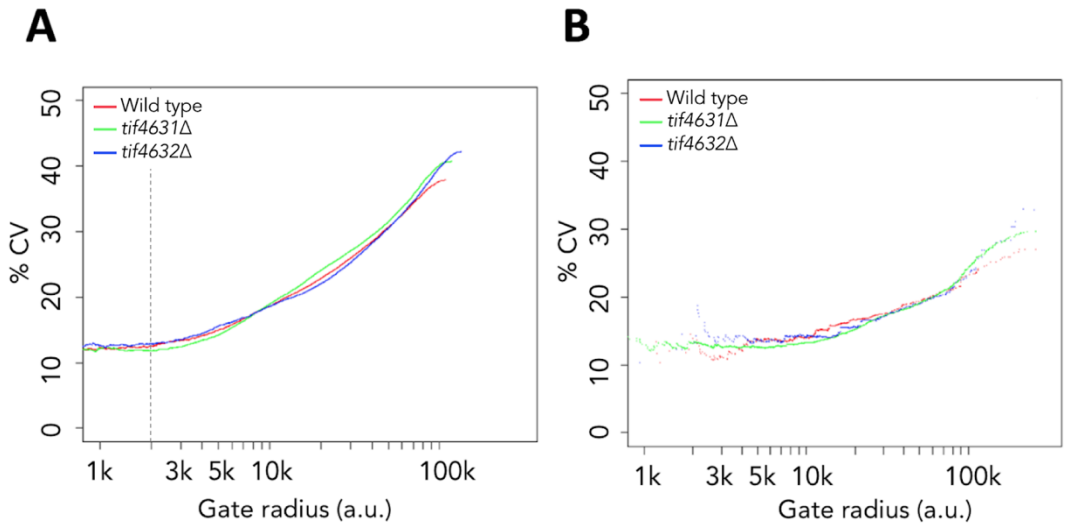

Figure 31: Example of CV versus gate radius plots of young and 10 generation old cells. A: plot shows an example of one CV versus gate radius plot for young cell analysis. Experiments were performed in triplicates (for the other two biological repeats plots refer to Chapter 10.3), and a gate radius of 2k reveals approximation to a minimum CV. **B:** plot shows plot shows one CV versus gate radius plot for 10-generation old cell analysis. Experiments were performed in triplicates (for the other two biological repeats plots refer to Chapter 10.3), and the gate radius was defined individually for each strain, maintaining a balance between the smallest CV while considering a sufficient number of cells for the analysis. In this example, gate radii were defined between 4k and 8k, where CV was smallest, the curve was fairly stable and a sufficient number of cells was included for the analysis.

The results of three independent experiments can be seen in Figure 32, where plot A summarizes the results of young cells analysis and plot B summarizes the results of 10-generation old cells analysis.

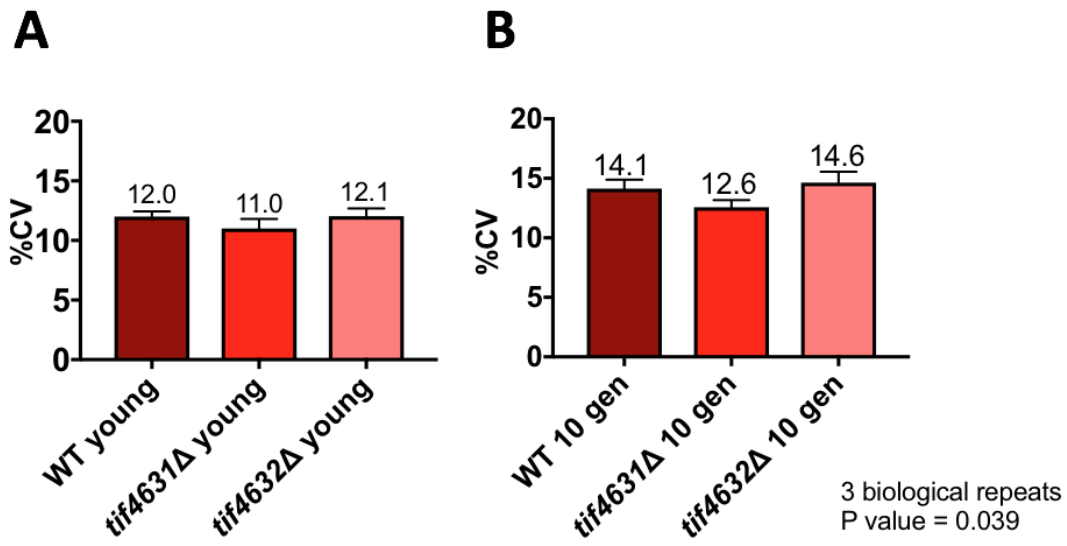

Figure 32: Flow cytometry analysis of cell-to-cell heterogeneity in young and 10 generation old cells. The coefficient of variance was calculated from flow cytometry data and is represented in the bars, with values indicated above. Whiskers show standard deviation. For each strain, fluorescence heterogeneity was measured for **A:** exponential-phase (young), and **B:** after overnight incubation (10-generation old). Statistical analysis was performed using one-way ANOVA. No statistically significant difference is observed between young populations of the three strains analysed ($F(2,6)$= 2.437, p = 0.17). For 10-generation old analysis, populations showed a statistically significant difference in the level of noise (%CV) ($F(2,6)$= 5.845, p = 0.039).

There is an increase in the estimated intrinsic gene expression noise in the cells of all strains analysed as they age, and a t-test analysis shows that for WT and *tif4632*Δ strains this age-dependent increase is statistically significant (WT [[M young = 12 ± 0.2517. M old = 14.13 ± 0.4333], $t(4) = 4.3$, $p = 0.013$], *tif4632*Δ [[M young = 12.03 ± 0.3844, M old = 14.63 ± 0.5364], $t(4) = 3.9$, $p = 0.017$]). For tif4631Δ strain, which has the smallest increase in the level of noise during the ageing process, the age-dependent increase is not statistically significant ([M young = 11 ± 0.4619, M old = 12.57 ± 0.348], $t(4) = 2.7$, $p = 0.053$).

Additionally, *tif4631*Δ displays the smallest CV from a very young age, when compared to WT and *tif4632*Δ, although one-way ANOVA analysis shows that the CV difference between strains analysed at a young age is not statistically significant.

Since the number of cells analysed at this stage is high, it can be concluded that young cells of these three strains analysed do not manifest a significant difference in the control of gene expression, presenting a similar level of gene expression noise.

Interestingly, for 10-generation old analysis, *tif4631*Δ displays the smallest increase in the estimated intrinsic noise during the ageing process, having the smallest CV value, when compared to 10-generation old WT and *tif4632*Δ strains. At this age, one-way ANOVA analysis shows a statistically significant difference between the strains' CV values, with a P value of 0.039.

After successfully performing the analysis of 10-generation old cells, I wanted to analyse even older cells. In order to do this, I decided to analyse cells that went through approximately 15 budding processes since a similar study performed by Janssens and Veenhoff in 2016 observed a median replicative life span of 16 generations.

The analysis was performed as described for 10-generation old cells, but with a longer cultivation time. Four independent replicates were performed for 15-generation-old cell analysis to compensate for an even more reduced proportion of old stained cells in the culture. Again, for the young cell analysis, 50,000 events were measured and a gating radius of 2k was used to estimate the intrinsic noise (Figure 33 A). For old cell analysis, millions of events were measured and due to the increased difficulty of performing this 15-generation old analysis, and due to old cells behaving differently in different strains, each gating radius was defined individually, as mentioned before (p88), and I continued to follow the rationale of choosing the smallest CV value while including a sufficient number of cells for the analysis (Newman et al., 2006) (Figure 33 B).

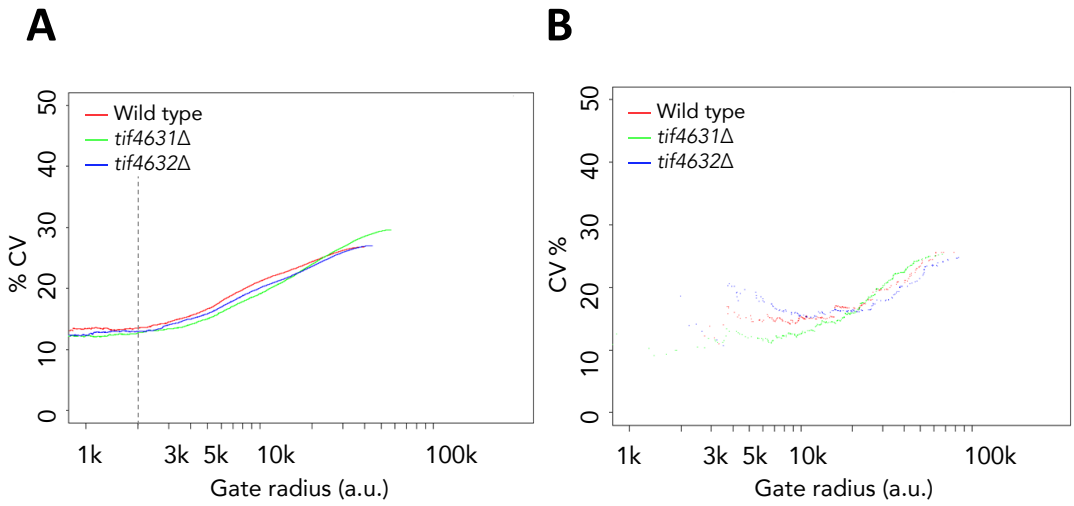

Figure 33: Example of CV versus gate radius plots of young and 15 generation old cells. A: plot shows an example of one CV versus gate radius plot for young cell analysis. Experiments were performed in four independent replicates (for the other three biological repeats plots refer to Chapter 10.5), and a gate radius of 2k reveals approximation to a minimum CV. **B:** plot shows plot shows one CV versus gate radius plot for 15-generation old cell analysis. Experiments were performed in four independent replicates (for the other three biological repeats plots refer to Chapter 10.5), and the gate radius was defined individually for each strain, maintaining a balance between the smallest CV while considering a sufficient number of cells for the analysis. In this example, gate radii were defined between 18k and 27k, where CV was smallest, the curve was relatively stable and a sufficient number of cells was included for the analysis.

The results of four independent experiments can be seen in Figure 34, where plot A summarizes the results of young cells analysis and plot B summarizes the results of 15-generation old cells analysis.

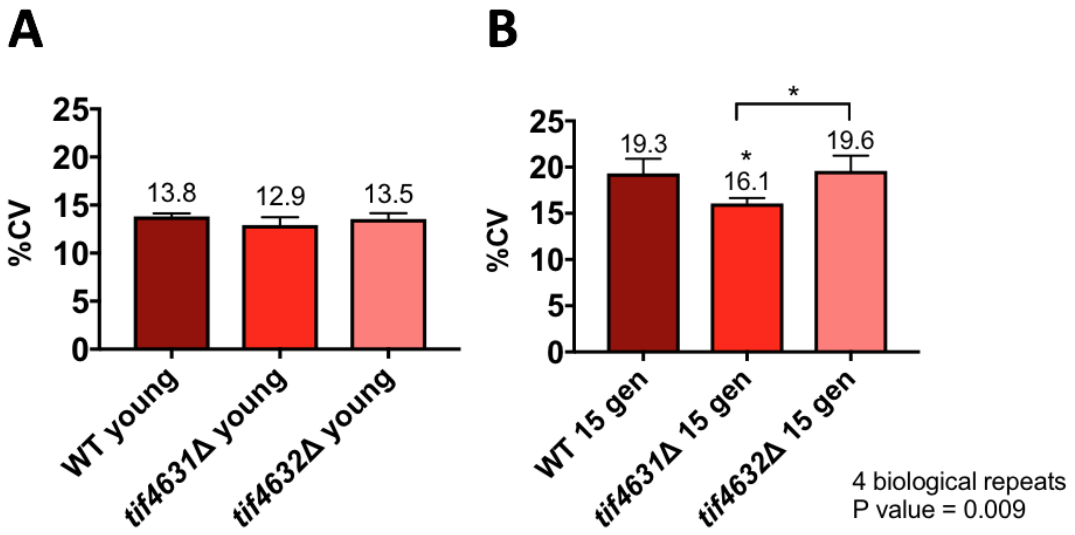

Figure 34: Flow cytometry analysis of cell-to-cell heterogeneity in young and 15 generation old cells. The coefficient of variance was calculated from flow cytometry data and is represented in the bars, with values indicated above. Whiskers show standard deviation. For each strain, fluorescence heterogeneity was measured for **A:** exponential-phase (young), and **B:** 15-generation old. Statistical analysis was performed using one-way ANOVA. No significant difference is observed between young populations of the three strains analysed ($F(2,9) = 2.262$, $p = 0.16$). For 15-generation old analysis, populations showed a very significant statistical difference in the level of noise (%CV) ($F(2,9) = 8.319$, $p = 0.009$). Post-hoc Tukey analysis test showed that *tif4631Δ* strain differs significantly from both WT and *tif4632Δ* strains ($p < 0.05$); WT and tif4632Δ strains do not differ significantly.

Here, the same trend is observed, and the estimated intrinsic gene expression noise increases for all three strains during the ageing process. At this age, a t-test analysis shows that for each strain the increase in the noise level over the ageing process is statistically very significant (WT [[M young = 13.83 ± 0.1548. M old = 19.33 ± 0.7941], $t(6) = 6.8$, $p = 0.0005$], *tif4631Δ* [[M young = 12.93 ± 0.409. M old = 16.08 ± 0.2898], $t(6) = 6.3$, $p = 0.0008$], *tif4632Δ* [[M young = 13.55 ± 0.3014. M old = 19.6 ± 0.8196], $t(6) = 6.9$, $p = 0.0004$]).

The *tif4631Δ* strain continues to display the smallest CV from a very young age when compared to WT and *tif4632Δ*, and the difference in CV values between the three strains remains statistically not significant, according to one-way ANOVA analysis.

Since *S. cerevisiae* cells divide asymmetrically, the ageing process of daughter cells is reset. The absence of significant intracellular damage at this early stage might help explain the similar level of gene expression stochasticity observed in young cells of these strains.

It is notable that, after 15 generations, the *tif4631*Δ strain continues to display the smallest increase in the estimated intrinsic noise during the ageing process, having again the smallest CV value, when compared to 15-generation old WT and *tif4632*Δ strains. Strikingly, one-way ANOVA analysis shows a very significant difference between the CV values of 15-generation old WT, *tif4631*Δ and *tif4632*Δ strains, with a P-value of 0.009. Additionally, *a posteriori* (post-hoc) test performed to confirm where the differences occurred between the strains revealed that *tif4631*Δ is significantly different from both WT and *tif4632*Δ, while WT and *tif4632*Δ were not significantly different from each other.

The *tif4631*Δ strain has decreased translation activity since the translation initiation factor eIF4G1 is absent. eIF4G1 represents 85% of total eIF4G content and its deletion reduces the overall translation activity (Firczuk et al., 2013). Li et al., 2009 also demonstrated that *TIF4631* gene is involved in ribosomal biogenesis, with the *tif4631*Δ strain displaying a defective synthesis of large ribosomal units. Additionally, McCormick et al. has reported in 2015 that this strain has a longer lifespan and Ramirez-Valle et al., (2008) demonstrated that the absence of eIF4G1 promotes autophagy in the cell, a process that is also involved in the regulation of lifespan.

The deletion of translation factors would be expected to influence extrinsic noise because of the consequential effects on the translation machinery (and thus global protein synthesis). In the present study, we have not directly calculated the extrinsic noise values because such calculations will not be very precise using the approach of Newman et al (2006). The latter method provides a more accurate estimate of intrinsic noise, which in any case is valuable because it relates to the noise specifically

associated with expression of the reporter construct. In future work, a dual-reporter strategy based on the method described by Elowitz et al (2002) will be used to obtain more precise estimates of the extrinsic noise values.

Nevertheless, the fact that the analysis of 15-generation-old cells reveals the same trend as observed for 10-generation old cells provides strong evidence for a relationship between ageing, cap-dependent translation and gene expression noise.

Chapter 7 - General discussion and future work

Translation is a crucial biological process. Several pathways that are known to influence ageing also modulate translation activity, like target of rapamycin (TOR), insulin-insulin growth factor (Ins-IGF-1) and mitogen-activated-protein-kinase (MAPK) pathways (Gonskikh & Polacek, 2017). Gene expression stochasticity is also a biologically important variable, playing a role in many cellular processes, including ageing (Newlands et al., 1998; Rea et al., 2005; Bahar et al., 2006; Martinez-Jimenez et al., 2017; Sarnoski et al., 2018).

We are the first group, to our knowledge, to investigate the relationship between ageing, translation and gene expression noise. In this study, using two independent methodologies (microfluidic technology and flow cytometry), I investigated this relationship in the budding yeast *S. cerevisiae*.

The use of microfluidic technology combined with image analysis provides a strategy to observe yeast cells and monitor protein expression during the ageing process. There are, however, certain limitations to this approach. In the CLiC 2 design, medium perfusion was a limiting factor, especially after all the trapping structures were occupied by the cells. In this work, the majority of the cells grown in the CLiC 2 device displayed normal growth and viability, but a small number of cells located at the bottom of the elongated cavities were affected by reduced medium perfusion and displayed signs of glucose-limited growth. Another limitation of this device was cell segmentation and image analysis, which were hindered by the proximity of the cells, impairing the use of different software packages (CellProfiler, Imaris) for automated image analysis.

Cell-wall staining combined with flow cytometry analysis overcame medium perfusion limitation, thus improving control over the growth conditions and reducing the time required for data analysis. This allowed more biological repeats

to be performed in the same time interval required for one biological repeat using the CLiC design, which is an additional advantage. Overall, it is evident that cell-wall staining combined with flow cytometry analysis is a less laborious and time-demanding strategy to analyse yeast cells and monitor protein expression during their ageing process. One limitation of flow cytometry analysis, compared to microscopy, is that the morphological characteristics of the cells cannot be observed during the experiment. However, this limitation had no real impact on the type of study performed here.

Despite the different characteristics and limitations of the respective methodologies, the results obtained using microfluidic technology and image analysis are generally consistent with the results obtained using cell wall staining combined to flow cytometry analysis. Both sets of results show that the three strains analysed, WT, *tif4631Δ and tif4632Δ* display an increase in gene expression noise during the ageing process. This observation is coherent with other reported data. Newlands et al. (1998) demonstrated that in mature skeletal muscle fibres the mechanism of gene expression becomes stochastic, with transcription occurring in pulses. Moreover, Bahar et al. (2006) studied the transcriptional noise of housekeeping and heart-specific genes in mouse cardiomyocytes, observing that noise increases with ageing. Consistent with these observations, recent investigations performed by Sarnoski et al. (2018) on diploid yeast cells and demonstrated that old cells display higher levels of gene expression noise when compared to young cells.

An important feature of the present work is that the *tif4631Δ* strain displays the lowest level of noise when compared to wild-type and *tif4632Δ* strains. The *tif4631Δ* strain has a decreased translation rate, since the translation initiation factor eIF4G1, the main eIF4G isoform, is absent. As reported previously, eIF4G1 constitutes 85% of the total eIF4G content and reduced eIF4G content can impact the overall translation activity (Firczuk et al., 2013). The absence of eIF4G2 (*tif4632Δ*), on the

other hand, imposes only a small attenuation of translation initiation (Firczuk et al., 2013). Additionally, Li et al. (2009) demonstrated that the *tif4631*Δ strain shows an impaired synthesis of large ribosomal subunits, which also contributes to reduced translation and, via a yet unknown mechanism, increases longevity. Therefore, our results indicate that the level of gene expression noise and translation rate are both inversely correlated with the lifespan.

When comparing young cells of the three strains investigated, statistical analysis showed that the level of noise does not vary significantly and the cells of the different strains start their life with similar levels of gene expression stochasticity. This might be due to the asymmetric cell division of *S. cerevisiae*, where daughter cells have their ageing process reset, while the mother cell asymmetrically retains the intracellular damage (Higuchi-Sanabria et al., 2014), including oxidatively damaged proteins. Reduced intracellular damage might contribute to more accurate gene expression regulation. Supporting this hypothesis is one experiment performed by Bahar et al. (2006) which demonstrated that young mouse cardiomyocytes treated with hydrogen peroxide, an inducer of oxidative damage, displayed an increased level of gene expression noise when compared to non-treated young cardiomyocytes.

Of relevance to the fact that cells with less intracellular damage manifest a reduced level of stochasticity is the observation that the *tif4631*Δ strain, which has a reduced translation rate, displays a slower increase in the level of noise during the ageing process. Decreased translation activity slows down the misfolded protein production rate, which might result in less intracellular damage accumulation (Hipkiss, 2007), especially of oxidatively damaged proteins. Thus, the *tif4631*Δ strain might display this slower increase in gene expression noise during the ageing process due to a delayed accumulation of damaged proteins. This is again consistent with the results observed by Bahar et al., (2006) since the induction of oxidative damage could also increase the amount of oxidatively damaged proteins.

Additionally, the protein synthesis process consumes up to 75% of the cell energy (Lane & Martin, 2010), and therefore reduced translation might also result in energy resources being shifted to cellular maintenance and repair processes. Evidence for this interpretation was given by Tavernarakis in 2007, showing that model organisms with reduced protein synthesis had increased stress resistance and longer life span. It is possible that cells with more energy resources available for cell maintenance might better regulate the gene expression process, which can result in reduced noise, but further studies are necessary to confirm that.

As mentioned, the results obtained in this work are consistent with the works performed by Newlands et al., 1998; Bahar et al., 2006 and Sarnoski et al., 2018, demonstrating an age-dependent increase in noise. However, it is important to know that Liu et al. (2017) reported that gene expression noise decreases during the ageing process. In Liu et al. they used microfluidics to study heterogeneity in yeast cells expressing YFP controlled by the regulatable P_{GAL} promoter. They used a combination of 0.2% glucose and 0.5% galactose as the carbon source. Of the two key differences in the experimental conditions used by Liu and colleagues, their use of a regulatable promoter is likely to be the most significant. This interpretation is supported by the fact that the same group reported an age-dependent increase in gene expression noise for a constitutively expressed construct (P_{TEF1}-ssGFP; a GFP isoform with a shorter half-life) in diploid cells (Sarnoski et al., 2018). The most likely explanation of the results described in Liu et al. (2017) is that the P_{GAL} promoter displays very different expression dynamics to a constitutive promoter such as P_{TEF1}.

Although there are differences between the results observed in this investigation and the results found in the work of Liu et al., some of our findings point in the same direction. In their study, the authors found that a long-lived strain, *rpd3*Δ, has the lowest level of noise variation during the ageing process, compared to all the other strains they analysed. This agrees with my findings that the *tif4631*Δ strain, which has a longer lifespan, also shows the lowest level of noise variation during the ageing

process, compared to the other strains I analysed. In combination, therefore, these data suggest that more stable and accurate gene expression, with smaller variations during the ageing process, can be related to longer life span.

Among the pathways involved in the ageing process, the target of rapamycin (TOR), insulin-insulin growth factor (Ins-IGF-1) and mitogen-activated-protein-kinase (MAPK) pathways also influence protein synthesis. Those pathways, when modulated, can stimulate or suppress ribosome production and influence the activity of the eIF4E initiation factor (Gonskikh & Polacek, 2017). mTOR is an important regulatory signalling pathway, responsive to stress, growth factors and nutritional state of the cell. Downregulation of the mTOR pathway, which is known to increase lifespan, reduces phosphorylation of eIF4E-binding-proteins (4E-BP) (Gonskikh & Polacek, 2017). Phosphorylated 4E-BP releases eIF4E, allowing eIF4E to interact with eIF4G. Dephosphorylated 4E-BPs form a stable complex with eIF4E, competing with eIF4G and reducing cap-dependent translation (Gebauer & Hentze, 2004). Thus, dephosphorylated 4E-BPs deplete the pool of available eIF4E, decreasing its interaction with eIF4G, an important translation initiation step. One of the strains used in this study, *tif4631Δ,* lacks the eIF4G1 translation factor, the most representative of the eIF4G isoforms. This strain was shown to be long-lived by McCormick et al in 2015. The lifespan-increasing effect seen in this strain might be attributable to similar mechanisms as the ones inducing longer lifespan in the mTOR pathway downregulation. Since interaction between eIF4E and eIF4G is reduced in the *tif4631Δ* strain by the absence of eIF4G1, translation rate is also reduced (Firczuk et al., 2013), and the increased lifespan observed in the *tif4631Δ* strain might be promoted by a mechanism similar to mTOR downregulation. Supporting this interpretation is the work performed by Ramirez-Valle et al. (2008), where it was observed that eIF4G1 depletion (but not depletion of other eIF4G family members) partially phenocopies inhibition of the mTOR pathway or nutrient starvation. The authors used siRNA silencing to reduce the levels of eIF4G1 in a breast epithelial cell line and observed that proliferative and bioenergetics

alterations of these cells were very similar to those observed in mTOR inhibited cells. eIF4G1-depleted cells display reduced cell size, decreased bioenergetic, mitochondrial and proliferation activities and manifested increased autophagy. Although Ramirez-Valle demonstrated these effects in mammalian cells, eIF4G is conserved across species and it is speculated that the role of mammalian eIF4G in ageing is similar, if not identical, as exhibited in simpler organisms, including yeast (Howard and Rogers, 2014). Therefore, taken together, these findings support the interpretation that the absence of eIF4G1 probably increases lifespan through a similar mechanism to that linked to the downregulation of the mTOR pathway.

The increased autophagy observed in the *tif4631*Δ strain could also be behind the slower increase in gene expression noise over the ageing process. Autophagy is one of the cell quality control pathways involved in the maintenance of homeostasis and is the preferred degradative route for cytoplasmic materials as invading bacteria, organelles and protein aggregates (Dikic, 2017). By targeting protein aggregates, autophagy contributes to proteostasis, reducing the accumulation of damaged proteins, and impacts the ageing process. The accumulation of defective and toxic proteins impacts the function of organelles and is recognized as an important factor in ageing and ageing-related diseases (López-Otín et al., 2013; Dikic, 2017). Autophagy takes place when the ubiquitin-proteasome system (the major pathway for protein degradation (Kruegel et al., 2011) becomes overwhelmed or inhibited, clearing the protein aggregates that accumulate due to reduced or inhibited proteasome activity (Dikic, 2017). Thus, reduced accumulation of toxic proteins (due to decreased protein biosynthesis) accompanied by augmented clearance of damaged proteins (promoted by increased autophagy) can facilitate more accurate gene expression, therefore reducing the level of noise increase over the lifespan. Once more, this interpretation is in consonance with what was observed by Bahar et al. in mouse cardiomyocytes after induction of oxidative damage. Increased oxidative damage resulted in cells displaying an increased level of gene expression noise.

The activity of translation machinery components and gene expression noise are also relevant to cancer. Abnormal expression of translation initiation factors was observed in several types of cancer, with initiation factors being involved in cellular transformation and tumour development, affecting cancer cell survival, angiogenesis and metastasis (de la Parra et al., 2018). eIF4G1, specifically, is overexpressed in nasopharyngeal carcinoma, squamous cell lung carcinoma and breast cancer, with eIF4G1 being the significant predictor of inflammatory breast cancer cells (Howard and Rogers, 2014). Consistently, overexpression of eIF4G1 was sufficient to induce tumour transformation in mouse fibroblasts (Fukuchi-Shimogori et al., 1997), demonstrating the importance of this initiation factor in cancer, particularly its expression regulation. Regarding gene expression noise, Han et al., (2016) demonstrated a link between cancer and noise. The authors performed a genomic scale investigation and observed increased gene expression noise in cancer cells, compared to the level in noise of normal cells. They analysed the transcriptomic data of human liver, colon, lung and breast cancers, observing that gene expression noise was increased in 74.9% of the 16,424 genes analysed when compared to normal tissues, which suggests that the necessary precise control of gene expression failed during cancer development (Han et al., 2016). It was also observed by the authors of this study that patients with low p53 (a pathway involved in cell senescence and genome stability) and low immune activity had a propensity to increased gene expression noise. Consistently, they found that more than 53% of genes displayed increased stochasticity in patients with late-stage, as opposed to early-stage cancer, indicating that accuracy in gene expression was linked to the cancer outcome (Han et al., 2016). Taken together, these data point to the importance of the activity of translation initiation factors and the accuracy of gene expression to age-related diseases. The control of eIF4G1 expression is essential, with its deregulation impacting cancer development, angiogenesis and metastasis, while gene expression noise is linked to cancer outcome, being elevated in tumour cells, suggesting that there is aberrant gene expression control during cancer development. These facts also point to the importance of the investigation of the

relationship between gene expression noise and the activity of translation machinery components.

Another study indicating that there is a correlation between translation machinery components, gene expression noise and the ageing process is that of Janssens et al., (2015). The authors analysed at a system level the transcriptome and proteome of ageing yeast, observing that over the lifespan, the proteome becomes uncoupled from the transcriptome. In their analysis, to identify the most uncoupled cellular processes, they plotted the fold changes of the transcript and protein expression of young and old cells in a map divided into quadrants. Quadrants 1 and 3 had coupled expression of transcripts and proteins, while quadrants 2 and 4 had uncoupled transcriptome and proteome. In quadrant 2, proteins of old cells were over-represented in comparison to their transcripts, with 38.4% of the transcript-protein pairs analysed being located in this quadrant. This suggests a global tendency of protein overabundance in comparison to their mRNA levels over the ageing process (Janssens et al., 2015). Strikingly, this quadrant was greatly enriched in gene products involved in protein synthesis, with ribosome, tRNA synthesis and translation regulation gene products being significantly overrepresented compared to their transcripts. This protein overrepresentation progressively increased as the cells aged, showing degenerative effects as accumulation of protein aggregates and loss of stoichiometry in protein complexes (Janssens et al., 2015). Based on further analysis, the authors developed a model which indicated that this protein overrepresentation is causal for ageing. Thus, the data obtained from Janssens et al. work supports our findings that there is a relationship between translation activity, gene expression noise and the ageing process. The overrepresentation of protein biogenesis machinery components is a driver of ageing and contributes to an accelerated accumulation of intracellular damage, including protein aggregates, which is widely known to influence lifespan. Additionally, the overrepresentation of translation machinery components contributes to and intensifies an increase in

proteome uncoupling from the transcriptome (Janssens et al., 2015), which can play an important role in the age-dependent noise increase observed in my results.

Janssens et al. also suggested that a robust lifespan extension has to target the driver of ageing, *i.e.* protein biogenesis, by altering the rate of protein synthesis (*i.e.* translation) or degradation (*i.e.* autophagy). The *tif4631*Δ strain has decreased translation activity due to the absence of eIF4G1 (Firczuk et al., 2013) and also has impaired synthesis of large ribosomal units (Li et al., 2009), which further contributes to decreased translation activity and increases lifespan. Furthermore, this strain has, as discussed, increased autophagy activity. Therefore, the fact that the results obtained by Janssens et al., are consistent with the data obtained in this PhD work strengthens the argument that translation rate and gene expression noise are inversely correlated to the lifespan of *S. cerevisiae*.

Future work

The results obtained in this PhD, using two independent techniques, provide new insight into the relationship between translation rate, gene expression noise and ageing. However, novel studies, together with answers, bring new questions to be addressed. We could obtain a more complete picture of this causal landscape by studying further long-lived strains and the influence of depletion of other translation factors on ageing and noise, and this will be a focus of future work. Additionally, a deeper investigation of intrinsic and extrinsic noise during the ageing process using a dual-reporter reporter strategy (Elowitz et al., 2002) will further enrich this research area and should also be a component of future research. Furthermore, the use of a different promoter in future studies will provide additional information about what influence promoter dynamics might have on gene expression noise over the ageing process.

Chapter 8 - Conclusions

The main aim of this project was to use two different and independent methodologies to investigate the relationship between translation machinery activity, gene expression noise and the ageing process in the budding yeast *S. cerevisiae*.

I used microfluidics combined with microscopy as one of the strategies to analyse yeast cells over their replicative lifespan. In a parallel strategy, I also applied a cell-wall staining method as the basis for studying gene expression noise during ageing using flow cytometry. This staining method allows the differentiation of young cells from old cells in an exponentially growing culture, permitting the application of flow cytometry in studies of ageing and gene expression noise.

The results obtained using microfluidics follow the same trend as those observed using flow cytometry, indicating that the application of the cell-wall staining method to track old cells over their replicative lifespan was successful and generated consistent results. Both methodologies suggest that there is a general increase in the level of gene expression noise during ageing, a result that is consistent with the literature. It is important to note that these results were obtained using a constitutive promoter that naturally lacks a TATA box.

The fact that one of the strains analysed (*tif4631*Δ) manifests both increased lifespan and a lower level of gene expression noise over the ageing process, compared to the other strains investigated (WT and *tif4632*Δ), suggests that accurate gene expression is coupled to longevity. Additionally, the *tif4631*Δ strain has reduced translation activity, while the WT strain has no alteration and the *tif4632*Δ strain manifests only a small attenuation of translation activity. Thus, taken together, these data indicate that translation rate and gene expression noise are inversely correlated to lifespan.

The fact that two different and independent methodologies were applied in this study and generated coherent and consistent results strengthens the findings obtained here. We are the first group, to our knowledge, to investigate how translation machinery activity and gene expression noise are related to the ageing process. This is an important study since there is evidence that both translation activity and gene expression noise are linked to ageing and ageing-related diseases.

Finally, the use of cell-wall staining enables complex studies of this kind to be particularly automated, thus enhancing both the range and speed of this type of work. Further improvements in the cell-wall staining technique in future work will help enhance such research even more.

Chapter 9 - Bibliography

ADLER, A. S.; SINHA, S.; KAWAHARA, T. L. A.; et al. Motif module map reveals enforcement of aging by continual NF-B activity. **Genes and Development**, v. 21, p. 3244–3257, 2007.

AITKEN, C. E.; LORSCH, J. R. A mechanistic overview of translation initiation in eukaryotes. **Nature Structural and Molecular Biology**, v. 19, n. 6, p. 568–576, 2012.

ALERS, S.; LÖFFLER, A. S.; WESSELBORG, S.; STORK, B. Role of AMPK-mTOR-Ulk1/2 in the Regulation of Autophagy: Cross Talk, Shortcuts, and Feedbacks. **Molecular and cellular biology**, v. 32, n. 1, p. 2–11, 2012.

ALGIRE, M. A.; MAAG, D.; SAVIO, P.; et al. Development and characterization of a reconstituted yeast translation initiation system. **RNA**, v. 8, n. 3, p. 382–97, 2002.

ALTMANN, M.; MÜLLER, P. P.; WITTMER, B.; et al. A *Saccharomyces cerevisiae* homologue of mammalian translation initiation factor 4B contributes to RNA helicase activity. **The EMBO journal**, v. 12, n. 10, p. 3997–4003, 1993.

ANISIMOV, V. N.; BERSTEIN, L. M.; POPOVICH, I. G.; et al. If started early in life, metformin treatment increases life span and postpones tumors in female SHR mice. **Aging**, v. 3, n. 2, p. 148–157, 2011.

ASANO, K.; SHALEV, A; PHAN, L.; et al. Multiple roles for the C-terminal domain of eIF5 in translation initiation complex assembly and GTPase activation. **The EMBO journal**, v. 20, n. 9, p. 2326–37, 2001.

BACON, J. S.; DAVIDSON, E. D.; JONES, D.; TAYLOR, I. F. The location of chitin in the yeast cell wall. **The Biochemical journal**, v. 101, n. 2, p. 36C–38C, 1966.

BAHAR, R.; HARTMANN, C. H.; RODRIGUEZ, K. A.; et al. Increased cell-to-cell variation in gene expression in ageing mouse heart. **Nature**, v. 441, n. 7096, p. 1011–1014, 2006.

BAKER, D. J.; DAWLATY, M. M.; WIJSHAKE, T.; et al. Increased expression of BubR1 protects against aneuploidy and cancer and extends healthy lifespan. **Nature cell biology**, v. 15, n. 1, p. 96–102, 2013.

BAKER, D. J.; WIJSHAKE, T.; TCHKONIA, T.; et al. Clearance of p16Ink4a-positive senescent cells delays ageing-associated disorders. **Nature**, v. 479, n. 7372, p. 232–6, 2011.

BALABAN, N. Q.; MERRIN, J.; CHAIT, R.; KOWALIK, L.; LEIBLER, S. Bacterial Persistence as a Phenotypic Switch. **Science**, v. 305, n. 5690, p. 1622–1625, 2004.

BARKAI, N.; LEIBLER, S. Biological rhythms: Circadian clocks limited by noise. **Nature**, v. 403, n. 6767, p. 267–268, 2000.

BEN-SHEM, A.; DE LOUBRESSE, N. G.; MELNIKOV, S.; et al. The structure of the eukaryotic ribosome at 3.0 Å resolution. **Science**, v. 334, n. 6062, p. 1524–1529, 2011.

BERTHELOT, K.; MULDOON, M.; RAJKOWITSCH, L.; HUGHES, J.; MCCARTHY, J. E. G. Dynamics and processivity of 40S ribosome scanning on mRNA in yeast. **Molecular Microbiology**, v. 51, n. 4, p. 987–1001, 2004.

BLAKE, W. J.; BALÁZSI, G.; KOHANSKI, M. A.; et al. Phenotypic consequences of promoter-mediated transcriptional noise. **Molecular cell**, v. 24, n. 6, p. 853–65, 2006.

BOOTH, I. R. Stress and the single cell: Intrapopulation diversity is a mechanism to ensure survival upon exposure to stress. **International Journal of Food Microbiology**, v. 78, n. 1–2, p. 19–30, 2002. Elsevier.

BURGER, M. M.; GOLDBERG, A. R. Identification of a tumor-specific determinant on neoplastic cell surfaces. **Proceedings of the National Academy of Sciences**, v. 57, p. 359–366, 1967.

CABIB, E.; BOWERS, B. Chitin and yeast budding. Localization of chitin in yeast bud scars. **The Journal of biological chemistry**, v. 246, n. 1, p. 152–9, 1971.

CALDERWOOD, S. K.; MURSHID, A.; PRINCE, T. The Shock of Aging: Molecular Chaperones and the Heat Shock Response in Longevity and Aging – A Mini-Review. **Gerontology**, v. 55, p. 550–558, 2009.

CARPENTER, A. E.; JONES, T. R.; LAMPRECHT, M. R.; et al. CellProfiler: image analysis software for identifying and quantifying cell phenotypes. **Genome Biology**, v. 7, n. 10, p. R100.0-R100.11, 2006.

CHANG, H. H.; HEMBERG, M.; BARAHONA, M.; INGBER, D. E.; HUANG, S. Transcriptome-wide noise controls lineage choice in mammalian progenitor cells. **Nature**, v. 453, n. 7194, p. 544–547, 2008.

CHAVATTE, L.; SEIT-NEBI, A.; DUBOVAYA, V.; FAVRE, A. The invariant uridine of stop codons contacts the conserved NIKSR loop of human eRF1 in the ribosome. **EMBO Journal**, v. 21, n. 19, p. 5302–5311, 2002.

CHEN, C.; LIU, Y.; ZHENG, P. mTOR Regulation and Therapeutic Rejuvenation of Aging Hematopoietic Stem Cells. **Science Signaling**, v. 2, n. 98, p. ra75, 2009.

CHEN, C.; STEVENS, B.; KAUR, J.; et al. Dissociation Early in Protein Synthesis. **Proceedings of the National Academy of Sciences**, v. 108, n. 41, p. 1–6, 2011.

CHEN, K. L.; CRANE, M. M.; KAEBERLEIN, M. Microfluidic technologies for yeast replicative lifespan studies. **Mechanisms of Ageing and Development**, v. 161, p. 262–269, 2016.

COOKSON, N. A.; COOKSON, S. W.; TSIMRING, L. S.; HASTY, J. Cell cycle-dependent variations in protein concentration. **Nucleic Acids Research**, v. 38, n. 8, p. 2676–2681, 2010.

CRANE, M. M.; CLARK, I. B. N.; BAKKER, E.; SMITH, S.; SWAIN, P. S. A Microfluidic System for Studying Ageing and Dynamic Single-Cell Responses in Budding Yeast. **PLoS ONE**, v. 9, n. 6, p. 1–10, 2014.

DACHEUX, E.; MALYS, N.; XIANG, M.; et al. Translation initiation events on structured eukaryotic mRNAs generate gene expression noise. **Nucleic Acids Research**, v. 45, n. 11, p. 6981–6992, 2017.

DANG, W.; STEFFEN, K. K.; PERRY, R.; et al. Histone H4 lysine 16 acetylation regulates cellular lifespan. **Nature**, v. 459, p. 802–808, 2009.

DE LA PARRA, C.; WALTERS, B. A.; GETER, P.; SCHNEIDER, R. J. Translation initiation factors and their relevance in cancer. **Current Opinion in Genetics & Development**, v. 48, p. 82–88, 2018.

DEVER, T. E.; GREEN, R. The elongation, termination, and recycling phases of translation in eukaryotes. **Cold Spring Harbor Perspectives in Biology**, v. 4, n. 7, p. 1–16, 2012.

DIAS, C. A. O.; GREGIO, A. P. B.; ROSSI, D.; et al. EIF5A interacts functionally with eEF2. **Amino Acids**, v. 42, n. 2–3, p. 697–702, 2012.

DIKIC, I. Proteasomal and Autophagic Degradation Systems. **Annual Review of Biochemistry**, v. 86, n. 1, p. 193–224, 2017.

ELOWITZ, M. B.; LEVINE, A. J.; SIGGIA, E. D.; SWAIN, P. S. Stochastic gene expression in a single cell. **Science**, v. 297, n. 5584, p. 1183–1186, 2002.

EYLER, D. E.; GREEN, R. Distinct response of yeast ribosomes to a miscoding event during translation. **RNA**, v. 17, n. 5, p. 925–932, 2011.

FEHRMANN, S.; PAOLETTI, C.; GOULEV, Y.; et al. Aging yeast cells undergo a sharp entry into senescence unrelated to the loss of mitochondrial membrane potential. **Cell Reports**, v. 5, n. 6, p. 1589–1599, 2013.

FESER, J.; TRUONG, D.; DAS, C.; et al. Elevated Histone Expression Promotes Life Span Extension. **Molecular Cell**, v. 39, n. 5, p. 724–735, 2010.

FIORINO, E.; GIUDICI, M.; FERRARI, A.; et al. Critical Review The Sirtuin Class of Histone Deacetylases: Regulation and Roles in Lipid Metabolism. **IUBMB Life**, v. 66, n. 2, p. 89–99, 2014.

FIRCZUK, H.; KANNAMBATH, S.; PAHLE, J.; et al. An in vivo control map for the eukaryotic mRNA translation machinery. **Molecular Systems Biology**, v. 9, n. 635, p. 1–13, 2013.

FONTANA, L.; PARTRIDGE, L.; LONGO, V. D. Dietary Restriction, Growth Factors and Aging: from yeast to humans. **Science**, v. 328, n. 5976, p. 321–326, 2010.

FRASER, H. B.; HIRSH, A. E.; GIAEVER, G.; KUMM, J.; EISEN, M. B. Noise Minimization in Eukaryotic Gene Expression. **PLoS Biology**, v. 2, n. 6, p. e137, 2004.

FROLOVA, L.; LEGOFF, X.; ZHOURAVLEVA, G.; et al. Eukaryotic polypeptide chain release factor eRF3 is an eRF1- and ribosome-dependent guanosine triphosphatase. **RNA**, v. 2, p. 334–341, 1996.

FROLOVA, L. Y.; TSIVKOVSKII, R. Y.; SIVOLOBOVA, G. F.; et al. Mutations in the highly conserved GGQ motif of class I polypeptide release factors abolish ability of human eRF1 to trigger peptidyl-tRNA hydrolysis. **RNA**, v. 5, n. 8, p. 1014–1020, 1999.

FUKUCHI-SHIMOGORI, T.; ISHII, I.; KASHIWAGI, K.; et al. Malignant transformation by overproduction of translation initiation factor eIF4G. **Cancer research**, v. 57, n. 22, p. 5041–4, 1997.

GEBAUER, F.; HENTZE, M. W. Molecular mechanisms of translational control. **Nature Reviews Molecular Cell Biology**, v. 5, n. 10, p. 827–835, 2004.

GEMS, D.; PARTRIDGE, L. Genetics of Longevity in Model Organisms: Debates and Paradigm Shifts. **Annu Rev Physiol**, v. 75, p. 621–644, 2013.

GIBSON, D. G.; YOUNG, L.; CHUANG, R.-Y.; et al. Enzymatic assembly of DNA molecules up to several hundred kilobases. **Nature methods**, v. 6, n. 5, p. 343–347, 2009.

GIRALT, A.; VILLARROYA, F. SIRT3, a pivotal actor in mitochondrial functions: metabolism, cell death and aging. **Biochemical Journal**, v. 444, n. 1, p. 1–10, 2012.

GONSKIKH, Y.; POLACEK, N. Alterations of the translation apparatus during aging and stress response. **Mechanisms of Ageing and Development**, v. 168, p. 30–36, 2017.

GONZALEZ-SUAREZ, I.; REDWOOD, A. B.; PERKINS, S. M.; et al. Novel roles for A-type lamins in telomere biology and the DNA damage response pathway. **The EMBO Journal**, v. 28, p. 2414–2427, 2009.

GREGIO, A. P. B.; CANO, V. P. S.; AVACA, J. S.; VALENTINI, S. R.; ZANELLI, C. F. eIF5A has a function in the elongation step of translation in yeast. **Biochemical and Biophysical Research Communications**, v. 380, n. 4, p. 785–790, 2009.

GÜLDENER, U.; HECK, S.; FIEDLER, T.; et al. A new efficient gene disruption cassette for repeated use in budding yeast. **Nucleic Acids Research**, v. 24, n. 13, p. 2519–2524, 1996.

HALL, B. G.; ACAR, H.; NANDIPATI, A.; BARLOW, M. Growth rates made easy. **Molecular Biology and Evolution**, v. 31, n. 1, p. 232–238, 2014.

HAN, R.; HUANG, G.; WANG, Y.; et al. Increased gene expression noise in human cancers is correlated with low p53 and immune activities as well as late stage cancer. **Oncotarget**, v. 7, n. 44, p. 72011–72020, 2016.

HANAHAN, D.; JESSEE, J.; BLOOM, F. R. Plasmid Transformation of *E.coli* and Other Bacteria. **Methods in Enzymology**, v. 204, p. 63–113, 1991.

HIGUCHI-SANABRIA, R.; PERNICE, W. M. A.; VEVEA, J. D.; et al. Role of asymmetric cell division in lifespan control in *Saccharomyces cerevisiae*. **FEMS yeast research**, v. 14, n. 8, p. 1133–46, 2014.

HIPKISS, A. R. On why decreasing protein synthesis can increase lifespan. **Mechanisms of Ageing and Development**, v. 128, p. 412–414, 2007.

HOEIJMAKERS, J. H. J. DNA Damage, Aging, and Cancer. **New England Journal of Medicine**, v. 361, p. 1475–1485, 2009.

HOOPES, L. L. M.; BUDD, M.; CHOE, W.; WEITAO, T.; CAMPBELL, J. L. Mutations in DNA Replication Genes Reduce Yeast Life Span. **Molecular and Cellular Biology**, v. 22, n. 12, p. 4136–4146, 2002.

HOWARD, A.; ROGERS, A. N. Role of translation initiation factor 4G in lifespan regulation and age-related health. **Ageing research reviews**, v. 13, p. 115–24, 2014.

HUGHES, A. L.; GOTTSCHLING, D. E. An early age increase in vacuolar pH limits mitochondrial function and lifespan in yeast. **Nature**, v. 492, p. 261–267, 2012.

IOST, I.; DREYFUS, M.; LINDER, P. Ded1p, a DEAD-box protein required for translation initiation in *Saccharomyces cerevisiae*, is an RNA helicase. **The Journal of biological chemistry**, v. 274, n. 25, p. 17677–83, 1999.

JACKSON, R. J.; HELLEN, C. U. T.; PESTOVA, T. V. The mechanism of eukaryotic translation initiation and principles of its regulation. **Nature Reviews Molecular Cell Biology**, v. 11, n. 2, p. 113–127, 2010.

JANES, K. A.; WANG, C.-C.; HOLMBERG, K. J.; CABRAL, K.; BRUGGE, J. S. Identifying single-cell molecular programs by stochastic profiling. **Nature methods**, v. 7, n. 4, p. 311–320, 2010.

JANSSENS, G. E.; MEINEMA, A. C.; GONZÁLEZ, J.; et al. Protein biogenesis machinery is a driver of replicative aging in yeast. **eLife**, v. 4, p. 1–24, 2015.

JANSSENS, G.; VEENHOFF, L. Evidence for the hallmarks of human aging in replicatively aging yeast. **Microbial Cell**, v. 3, n. 7, p. 263–274, 2016.

JANZEN, V.; FORKERT, R.; FLEMING, H. E.; et al. Stem-cell ageing modified by the cyclin-dependent kinase inhibitor p16 INK4a. **Nature**, v. 443, p. 421–426, 2006.

JASKELIOFF, M.; MULLER, F. L.; PAIK, J.-H.; et al. Telomerase reactivation reverses tissue degeneration in aged telomerase deficient mice. **Nature**, v. 469, n. 7328, p. 102–106, 2011.

JIN, C.; LI, J.; GREEN, C. D.; et al. Histone Demethylase UTX-1 Regulates *C. elegans* Life Span by Targeting the Insulin/IGF-1 Signaling Pathway. **Cell Metabolism**, v. 14, n. 2, p. 161–172, 2011.

JO, M. C.; LIU, W.; GU, L.; DANG, W.; QIN, L. High-throughput analysis of yeast replicative aging using a microfluidic system. **Proceedings of the National Academy of Sciences**, v. 112, n. 30, p. 9364–9369, 2015.

KAEBERLEIN, M.; MCVEY, M.; GUARENTE, L. The SIR2/3/4 complex and SIR2 alone promote longevity in *Saccharomyces cerevisiae* by two different mechanisms. **Genes and Development**, v. 13, p. 2570–2580, 1999.

KAEBERLEIN, M.; KENNEDY, B. K. Large-scale identification in yeast of conserved ageing genes. **Mechanisms of Ageing and Development**, v. 126, n. 1, p. 17–21, 2005.

KAEBERLEIN, M. Lessons on longevity from budding yeast. **Nature**, v. 464, p. 513–519, 2010.

KANFI, Y.; NAIMAN, S.; AMIR, G.; et al. The sirtuin SIRT6 regulates lifespan in male mice. **Nature**, v. 483, p. 218–221, 2012.

KAPP, L. D.; LORSCH, J. R. The Molecular Mechanics of Eukaryotic Translation. **Annual Review of Biochemistry**, v. 73, n. 1, p. 657–704, 2004.

KÆRN, M.; ELSTON, T. C.; BLAKE, W. J.; COLLINS, J. J. Stochasticity in gene expression: From theories to phenotypes. **Nature Reviews Genetics**, v. 6, n. 6, p. 451–464, 2005.

KEMPE, H.; SCHWABE, A.; CRÉMAZY, F.; VERSCHURE, P. J.; BRUGGEMAN, F. J. The volumes and transcript counts of single cells reveal concentration homeostasis and capture biological noise. **Molecular Biology of the Cell**, v. 26, p. 797–804, 2014.

KENYON, C. The genetics of ageing. **Nature**, v. 464, p. 504–622, 2010.

KENYON, C. The first long-lived mutants: discovery of the insulin/IGF-1 pathway for ageing. **Philosophical Transactions of the Royal Society B: Biological Sciences**, v. 366, p. 9–16, 2011.

KIPPIN, T. E.; MARTENS, D. J.; VAN DER KOOY, D. p21 loss compromises the relative quiescence of forebrain stem cell proliferation leading to exhaustion of their proliferation capacity. **Genes & development**, v. 19, n. 6, p. 756–67, 2005.

KLINGE, S.; VOIGTS-HOFFMANN, F.; LEIBUNDGUT, M.; ARPAGAUS, S.; BAN, N. Crystal structure of the eukaryotic 60S ribosomal subunit in complex with initiation factor 6. **Science**, v. 334, n. 6058, p. 941–948, 2011.

KNIJNENBURG, T. A.; RODA, O.; WAN, Y.; et al. A regression model approach to enable cell morphology correction in high-throughput flow cytometry. **Molecular systems biology**, v. 7, n. 531, p. 1–19, 2011.

KO, M. S.; NAKAUCHI, H.; TAKAHASHI, N. The dose dependence of glucocorticoid-inducible gene expression results from changes in the number of transcriptionally active templates. **The EMBO journal**, v. 9, n. 9, p. 2835–42, 1990.

KOLITZ, S. E.; LORSCH, J. R. Eukaryotic initiator tRNA: Finely tuned and ready for action. **FEBS Letters**, v. 584, n. 2, p. 396–404, 2010.

KOLOSOV, P.; FROLOVA, L.; SEIT-NEBI, A.; et al. Invariant amino acids essential for decoding function of polypeptide release factor eRF1. **Nucleic Acids Research**, v. 33, n. 19, p. 6418–6425, 2005.

KOLOSOV, P.; FROLOVA, L.; SEIT-NEBI, A.; et al. Invariant amino acids essential for decoding function of polypeptide release factor eRF1. **Nucleic Acids Research**, v. 33, n. 19, p. 6418–6425, 2005.

KOSCHWANEZ, J.; HOLL, M.; CARLSON, R.; et al. Automated lifetime analysis of a single yeast cell. **IEEE International Conference on Automation Science and Engineering**, p.13–18, 2005.

KRISHNAMURTHY, J.; SU, L.; SHARPLESS, N. E.; et al. Ink4a/Arf expression is a biomarker of aging Find the latest version. **The Journal of Clinical Investigation**, v. 114, n. 9, p. 1299–1307, 2004.

KRUEGEL, U.; ROBISON, B.; DANGE, T.; et al. Elevated Proteasome Capacity Extends Replicative Lifespan in *Saccharomyces cerevisiae*. **PLoS Genetics**, v. 7, n. 9, p. 1–16, 2011.

LANE, N.; MARTIN, W. The energetics of genome complexity. **Nature**, v. 467, n. 7318, p. 929–934, 2010.

LARSON, K.; YAN, S.-J.; TSURUMI, A.; LIU, J.; ZHOU, J. Heterochromatin Formation Promotes Longevity and Represses Ribosomal RNA Synthesis. **PLoS Genetics**, v. 8, n. 1, p. 1–10, 2012.

LEE, I. H.; CAO, L.; MOSTOSLAVSKY, R.; et al. A role for the NAD-dependent deacetylase Sirt1 in the regulation of autophagy. **Proceedings of the National Academy of Sciences**, v. 105, n. 9, p. 3374–3379, 2008.

LEE, S. S.; VIZCARRA, I. A.; HUBERTS, D. H. E. W.; LEE, L. P.; HEINEMANN, M. Whole lifespan microscopic observation of budding yeast aging through a microfluidic dissection platform. **Proceedings of the National Academy of Sciences**, v. 109, n. 13, p. 4916–4920, 2012.

LEFEBVRE, A. K.; KORNEEVA, N. L.; TRUTSCHL, M.; et al. Translation initiation factor eIF4G-1 binds to eIF3 through the eIF3e subunit. **Journal of Biological Chemistry**, v. 281, n. 32, p. 22917–22932, 2006.

LEHNER, B. Selection to minimise noise in living systems and its implications for the evolution of gene expression. **Molecular systems biology**, v. 4, n. 170, p. 1–6, 2008.

LI, Z.; LEE, I.; MORADI, E.; et al. Rational extension of the ribosome biogenesis pathway using network-guided genetics. **PLoS Biology**, v. 7, n. 10, p. 1–17, 2009.

LIN, S. S.; MANCHESTER, J. K.; GORDON, J. I. Enhanced gluconeogenesis and increased energy storage as hallmarks of aging in *Saccharomyces cerevisiae*. **The Journal of biological chemistry**, v. 276, n. 38, p. 36000–7, 2001.

LINDER, P. Molecular biology of translation in yeast. **Antonie van Leeuwenhoek**, v. 62, n. 1–2, p. 47–62, 1992.

LINNANE, A.; OZAWA, T.; MARZUKI, S.; TANAKA, M. Mitochondrial DNA mutations as an important contributor to ageing and degenerative diseases. **The Lancet**, v. 333, n. 8639, p. 642–645, 1989.

LIU, S.; WIGGINS, J. F.; SREENATH, T.; et al. Dph3, a Small Protein Required for Diphthamide Biosynthesis, Is Essential in Mouse Development. **Molecular and cellular biology**, v. 26, n. 10, p. 3835–3841, 2006.

LIU, P.; YOUNG, T. Z.; MURRAT, A. Yeast Replicator: A High-Throughput Multiplexed Microfluidics Platform for Automated Measurements of Single-Cell Aging. **Cell Reports**, v. 13, p. 634–644, 2015.

LIU, P.; SONG, R.; ELISON, G. L.; PENG, W.; ACAR, M. Noise reduction as an emergent property of single-cell aging. **Nature Communications**, v. 8, n. 1, p. 1–13, 2017.

LOMBARD, D. B.; ALT, F. W.; CHENG, H.-L.; et al. Mammalian Sir2 Homolog SIRT3 Regulates Global Mitochondrial Lysine Acetylation. **Molecular and Cellular Biology**, v. 27, n. 24, p. 8807–8814, 2007.

LONGO, V. D.; FABRIZIO, P. Chronological Aging in *Saccharomyces cerevisiae*. **Sub-cellular biochemistry**. v. 57, p.101–121, 2011.

LÕOKE, M.; KRISTJUHAN, K.; KRISTJUHAN, A. Extraction of genomic DNA from yeasts for PCR-based applications. **Biotechniques**, v. 50, p. 325–328, 2011.

LÓPEZ-OTÍN, C.; BLASCO, M. A.; PARTRIDGE, L.; SERRANO, M.; KROEMER, G. The Hallmarks of Aging. **Cell**, v. 153, p. 1194–1217, 2013.

MAEGAWA, S.; HINKAL, G.; KIM, H. S.; et al. Widespread and tissue specific age-related DNA methylation changes in mice. **Genome Research**, v. 20, p. 332–340, 2010.

MAJUMDAR, R.; BANDYOPADHYAY, A.; MAITRA, U. Mammalian translation initiation factor eIF1 functions with eIF1A and eIF3 in the formation of a stable 40 S

preinitiation complex. **Journal of Biological Chemistry**, v. 278, n. 8, p. 6580–6587, 2003.

MARTINEZ-JIMENEZ, C. P.; ELING, N.; CHEN, H. C.; et al. Aging increases cell-to-cell transcriptional variability upon immune stimulation. **Science**, v. 355, n. 6332, p. 1433–1436, 2017.

MCCLOY, R. A.; ROGERS, S.; CALDON, C. E.; et al. Partial inhibition of Cdk1 in G2phase overrides the SAC and decouples mitotic events. **Cell Cycle**, v. 13, n. 9, p. 1400–1412, 2014.

MCCORMICK, M. A.; DELANEY, J. R.; TSUCHIYA, M.; et al. A Comprehensive Analysis of Replicative Lifespan in 4,698 Single-Gene Deletion Strains Uncovers Conserved Mechanisms of Aging. **Cell Metabolism**, v. 22, n. 5, p. 895–906, 2015.

MCVEY, M.; KAEBERLEIN, M.; TISSENBAUM, H. A.; GUARENTE, L. The Short Life Span of *Saccharomyces cerevisiae* sgs1 and srs2 Mutants Is a Composite of Normal Aging Processes and Mitotic Arrest Due to Defective Recombination. **Genetics**, v. 157, p. 1531–1542, 2001.

MENG, X.; FIRCZUK, H.; PIETRONI, P.; et al. Minimum-noise production of translation factor eIF4G maps to a mechanistically determined optimal rate control window for protein synthesis. **Nucleic Acids Research**, v. 45, n. 2, p. 1015–1025, 2017.

METHOT, N.; SONG, M. S.; SONENBERG, N. A Region Rich in Aspartic Acid, Arginine, Tyrosine, and Glycine (DRYG) Mediates Eukaryotic Initiation Factor 4B (eIF4B) Self-Association and Interaction with eIF3. **Molecular and cellular biology**, v. 16, n. 10, p. 5328–5334, 1996.

MORROW, G.; SAMSON, M.; MICHAUD, S.; TANGUAY, R. M. Overexpression of the small mitochondrial Hsp22 extends *Drosophila* life span and increases resistance to oxidative stress. **The FASEB Journal**, v. 18, n. 3, p. 598–599, 2004.

MORTIMER, R. K.; JOHNSTON, J. R. Life Span of Individual Yeast Cells. **Nature**, v. 183, n. 4677, p. 1751–1752, 1959.

MURPHY, K. F.; ADAMS, R. M.; WANG, X.; BALÁZSI, G.; COLLINS, J. J. Tuning and controlling gene expression noise in synthetic gene networks. **Nucleic Acids Research**, v. 38, n. 8, p. 2712–2726, 2010.

NAVEAU, M.; LAZENNEC-SCHURDEVIN, C.; PANVERT, M.; MECHULAM, Y.; SCHMITT, E. tRNA binding properties of eukaryotic translation initiation factor 2 from encephalitozoon cuniculi. **Biochemistry**, v. 49, n. 40, p. 8680–8688, 2010.

NEWLANDS, S.; LEVITT, L. K.; ROBINSON, C. S.; et al. Transcription occurs in pulses in muscle fibers. **Genes & development**, v. 12, n. 17, p. 2748–58, 1998.

NEWMAN, J. R. S.; GHAEMMAGHAMI, S.; IHMELS, J.; et al. Single-cell proteomic analysis of S. cerevisiae reveals the architecture of biological noise. **Nature**, v. 441, n. 7095, p. 840–846, 2006.
AARON, N.; WEINER, M. Enzyme induction as an all-or-none phenomenon. **Proceedings of the National Academy of Sciences**, v. 43, n. 7, p. 553–566, 1957

OLIVEIRA, C. C.; HEUVEL, J. J.; MCCARTHY, J. E. G. Inhibition of translational initiation in *Saccharomyces cerevisiae* by secondary structure: the roles of the stability and position of stem-loops in the mRNA leader. **Molecular Microbiology**, v. 9, n. 3, p. 521–532, 1993.

ONKEN, B.; DRISCOLL, M. Metformin Induces a Dietary Restriction–Like State and the Oxidative Stress Response to Extend *C. elegans* Healthspan via AMPK, LKB1, and SKN-1. **PLoS ONE**, v. 5, n. 1, p. 1–13, 2010.

ORTIZ, P. A.; ULLOQUE, R.; KIHARA, G. K.; ZHENG, H.; KINZY, T. G. Translation elongation factor 2 anticodon mimicry domain mutants affect fidelity and diphtheria toxin resistance. **Journal of Biological Chemistry**, v. 281, n. 43, p. 32639–32648, 2006.

PAN, K. Z.; PALTER, J. E.; ROGERS, A. N.; et al. Inhibition of mRNA translation extends lifespan in *Caenorhabditis elegans*. **Aging Cell**, v. 6, p. 111–119, 2007.

PATTERSON, M. N.; MAXWELL, P. H. Combining magnetic sorting of mother cells and fluctuation tests to analyze genome instability during mitotic cell aging in *Saccharomyces cerevisiae*. **Journal of Visualized Experiments**, n. 92, p. 1–13, 2014.

PESTOVA, T. V.; BORUKHOV, S. I.; HELLEN, C. U. T. Eukaryotic ribosomes require initiation factors 1 and 1A to locate initiation codons. **Nature**, v. 394, n. 6696, p. 854–859, 1998.

PISAREV, A. V.; HELLEN, C. U. T.; PESTOVA, T. V. Recycling of Eukaryotic Posttermination Ribosomal Complexes. **Cell**, v. 131, n. 2, p. 286–299, 2007.

PISAREV, A. V; SKABKIN, M. A.; PISAREVA, V. P.; et al. The role of ABCE1 in eukaryotic post-termination ribosomal recycling. **Molecular Cell**, v. 37, n. 2, p. 196–210, 2010.

PISAREVA, V. P.; PISAREV, A. V.; KOMAR, A. A.; HELLEN, C. U. T.; PESTOVA, T. V. Translation Initiation on Mammalian mRNAs with Structured 5′UTRs Requires DExH-Box Protein DHX29. **Cell**, v. 135, n. 7, p. 1237–1250, 2008.

POSTNIKOFF, S. D. L.; MALO, M. E.; WONG, B.; HARKNESS, T. A. A. The Yeast Forkhead Transcription Factors Fkh1 and Fkh2 Regulate Lifespan and Stress Response Together with the Anaphase-Promoting Complex. **PLoS Genet**, v. 8, n. 3, p. 1–13, 2012.

POWERS, E. T.; MORIMOTO, R. I.; DILLIN, A.; KELLY, J. W.; BALCH, W. E. Biological and Chemical Approaches to Diseases of Proteostasis Deficiency. **Annual Review of Biochemistry**, v. 788, p. 959–991, 2009.

RAJ, A.; VAN OUDENAARDEN, A. Nature, Nurture, or Chance: Stochastic Gene Expression and Its Consequences. **Cell**, v. 135, n. 2, p. 216–226, 2008.

RAMÍREZ-VALLE, F.; BRAUNSTEIN, S.; ZAVADIL, J.; FORMENTI, S. C.; SCHNEIDER, R. J. eIF4GI links nutrient sensing by mTOR to cell proliferation and inhibition of autophagy. **The Journal of cell biology**, v. 181, n. 2, p. 293–307, 2008.

RASER, J. M.; O'SHEA, E. K. Noise in Gene Expression: Origins, Consequences, and Control. **Science**, v. 309, n. 5743, p. 2010–2013, 2005.

REA, S. L.; WU, D.; CYPSER, J. R.; VAUPEL, J. W.; JOHNSON, T. E. A stress-sensitive reporter predicts longevity in isogenic populations of *Caenorhabditis elegans*. **Nature Genetics**, v. 37, n. 8, p. 894–898, 2005.

RESSLER, S.; BARTKOVA, J.; NIEDEREGGER, H.; et al. p16 INK4A is a robust in vivo biomarker of cellular aging in human skin. **Aging Cell**, v. 5, p. 379–389, 2006.

RICHTER-COOK, N.; DEVER, T.; HENSOLD, J.; MERRICK, W. Purification and characterization of a new eukaryotic protein translation factor. Eukaryotic initiation factor 4H. **Journal of Biological Chemistry**, v. 273, n. 13, p. 7579–7587, 1998.

ROUX, P. P.; TOPISIROVIC, I. Regulation of mRNA Translation by Signaling Pathways. **Cold Spring Harbor Perspectives in Biology**, v. 4, p. 1–23, 2012.

RUBINSZTEIN, D. C.; MARIÑ, G.; KROEMER, G. Leading Edge Review Autophagy and Aging. **Cell**, v. 146, p. 628–695, 2011.

RUGGERO, D.; MONTANARO, L.; MA, L.; et al. The translation factor eIF-4E promotes tumor formation and cooperates with c-Myc in lymphomagenesis. **Nature Medicine**, v. 10, n. 5, p. 484–486, 2004.

SAARIKANGAS, J.; BARRAL, Y. Protein aggregates are associated with replicative aging without compromising protein quality control. **eLife**, v. 4, p. 1–24, 2015.

SAHIN, E.; DEPINHO, R. A. Linking functional decline of telomeres, mitochondria and stem cells during ageing. **Nature**, v. 464, p. 520–528, 2010.

SAHIN, E.; DEPINHO, R. A. Axis of ageing: telomeres, p53 and mitochondria. **Nature Reviews Molecular Cell Biology**, v. 13, p. 397–404, 2012.

SAINI, P.; EYLER, D. E.; GREEN, R.; DEVER, T. E. Hypusine-containing protein eIF5A promotes translation elongation. **Nature**, v. 459, n. 7243, p. 118–121, 2009.

SARG, B.; KOUTZAMANI, E.; HELLIGER, W.; RUNDQUIST, I.; LINDNER, H. H. Postsynthetic Trimethylation of Histone H4 at Lysine 20 in Mammalian Tissues Is Associated with Aging*. **The Journal of Biological Chemistry**, v. 277, n. 42, p. 39195–39201, 2002.

SARNOSKI, E. A.; SONG, R.; ERTEKIN, E.; KOONCE, N.; ACAR, M. Fundamental Characteristics of Single-Cell Aging in Diploid Yeast. **iScience**, v. 7, p. 96–109, 2018.

SHARPLESS, N. E.; DEPINHO, R. A. How stem cells age and why this makes us grow old. **Nature Reviews Molecular Cell Biology**, v. 8, p. 703–713, 2007.

SHOEMAKER, C. J.; GREEN, R. Kinetic analysis reveals the ordered coupling of translation termination and ribosome recycling in yeast. **Proceedings of the National Academy of Sciences**, v. 108, n. 51, p. E1392–E1398, 2011.

SIMPSON, P. Notch signalling in development: on equivalence groups and asymmetric developmental potential. **Current Opinion in Genetics & Development**, v. 7, n. 4, p. 537–542, 1997.

SONENBERG, N.; HINNEBUSCH, A. G. Regulation of Translation Initiation in Eukaryotes: Mechanisms and Biological Targets. **Cell**, v. 136, n. 4, p. 731–745, 2009.

SONG, H.; MUGNIER, P.; DAS, A. K.; et al. The crystal structure of human eukaryotic release factor eRF1 - Mechanism of stop codon recognition and peptidyl-tRNA hydrolysis. **Cell**, v. 100, n. 3, p. 311–321, 2000.

STEFFEN, K. K.; DILLIN, A. A Ribosomal Perspective on Proteostasis and Aging. **Cell Metabolism**, v. 23, n. 6, p. 1004–1012, 2016.

TAVERNARAKIS, N. Protein Synthesis and Aging: eIF4E and the Soma vs. Germline Distinction. **Cell Cycle**, v. 6, n. 10, p. 1168–1171, 2007.

TAVERNARAKIS, N. Ageing and the regulation of protein synthesis: a balancing act? **Trends in Cell Biology**, v. 18, n. 5, p. 228–235, 2008.

TEIXEIRA, D.; SHETH, U.; VALENCIA-SANCHEZ, M. A.; BRENGUES, M.; PARKER, R. Processing bodies require RNA for assembly and contain nontranslating mRNAs. **RNA**, v. 11, n. 4, p. 371–382, 2005.

THATTAI, M.; OUDENAARDEN, A. Stochastic Gene Expression in Fluctuating Environments. **Genetics**, v. 167, n. 1, p. 523–530, 2004.

TILSTRA, J. S.; NIEDERNHOFER, L. J.; ROBBINS, P. D.; et al. NF-k kB inhibition delays DNA damage-induced senescence and aging in mice. **The Journal of Clinical Investigation**, v. 122, n. 7, p. 2601–2612, 2012.

UCHIDA, N.; HOSHINO, S. ICHI; IMATAKA, H.; SONENBERG, N.; KATADA, T. A novel role of the mammalian GSPT/eRF3 associating with poly(A)-binding protein in cap/poly(A)-dependent translation. **Journal of Biological Chemistry**, v. 277, n. 52, p. 50286–50292, 2002.

VAUX, D. L. Know when your numbers are significant. **Nature**, v. 492, p. 180, 2012.

VERMULST, M.; WANAGAT, J.; KUJOTH, G. C.; et al. DNA deletions and clonal mutations drive premature aging in mitochondrial mutator mice. **Nature genetics**, v. 40, n. 4, p. 392–394, 2008.

WEBB, T. R.; CROSS, S. H.; MCKIE, L.; et al. Diphthamide modification of eEF2 requires a J-domain protein and is essential for normal development. **Journal of Cell Science**, v. 121, n. 19, p. 3140–3145, 2008.

WEINBERGER, L. S.; BURNETT, J. C.; TOETTCHER, J. E.; ARKIN, A. P.; SCHAFFER, D. V. Stochastic gene expression in a lentiviral positive-feedback loop: HIV-1 Tat fluctuations drive phenotypic diversity. **Cell**, v. 122, n. 2, p. 169–82, 2005.

WELLS, S. E.; HILLNER, P. E.; VALE, R. D.; SACHS, A. B. Circularization of mRNA by eukaryotic translation initiation factors. **Molecular Cell**, v. 2, n. 1, p. 135–140, 1998.

WILKINSON, J. E.; BURMEISTER, L.; BROOKS, S. V; et al. Rapamycin slows aging in mice. **Aging Cell**, v. 11, p. 675–682, 2012.

XIE, Z.; ZHANG, Y.; ZOU, K.; et al. Molecular phenotyping of aging in single yeast cells using a novel microfluidic device. **Aging Cell**, v. 11, n. 4, p. 599–606, 2012.

YANG, H.; JIANG, X.; LI, B.; et al. Mechanisms of mTORC1 activation by RHEB and inhibition by PRAS40. **Nature**, v. 552, n. 7685, p. 368–373, 2017.

YANG, J.; MCCORMICK, M. A.; ZHENG, J.; et al. Systematic analysis of asymmetric partitioning of yeast proteome between mother and daughter cells reveals "aging factors" and mechanism of lifespan asymmetry. **Proceedings of the National Academy of Sciences**, v. 112, n. 38, p. 11977–11982, 2015.

YANG, S.-B.; TIEN, A.-C.; BODDUPALLI, G.; et al. Article Rapamycin Ameliorates Age-Dependent Obesity Associated with Increased mTOR Signaling in Hypothalamic POMC Neurons. **Neuron**, v. 75, p. 425–436, 2012.

YILMAZ, O. ¨ M. H.; KATAJISTO, P.; LAMMING, D. W.; et al. mTORC1 in the Paneth cell niche couples intestinal stem-cell function to calorie intake. **Nature**, v. 486, p. 490–496, 2012.

ZHANG, Y.; LUO, C.; ZOU, K.; XIE, Z.; BRANDMAN, O. Single Cell Analysis of Yeast Replicative Aging Using a New Generation of Microfluidic Device. **PLoS ONE**, v. 7, n. 11, p. 48275, 2012.

ZHANG, Z.; QIAN, W.; ZHANG, J. Positive selection for elevated gene expression noise in yeast. **Molecular Systems Biology**, v. 5, n. 299, p. 1–12, 2009. EMBO Press. Disponível em: <http://msb.embopress.org/content/5/1/299.long>. Acesso em: 16/1/2019.

ZHOURAVLEVA, G.; FROLOVA, L.; LE GOFF, X.; et al. Termination of translation in eukaryotes is governed by two interacting polypeptide chain release factors, eRF1 and eRF3. **The EMBO journal**, v. 14, n. 16, p. 4065–72, 1995.

ZID, B. M.; ROGERS, A. N.; KATEWA, S. D.; et al. 4E-BP Extends Lifespan upon Dietary Restriction by Enhancing Mitochondrial Activity in *Drosophila*. **Cell**, v. 139, n. 1, p. 149–160, 2009.

Chapter 10 - Appendices

This chapter contains the following data:

10.1. pNM1-HIS plasmid map

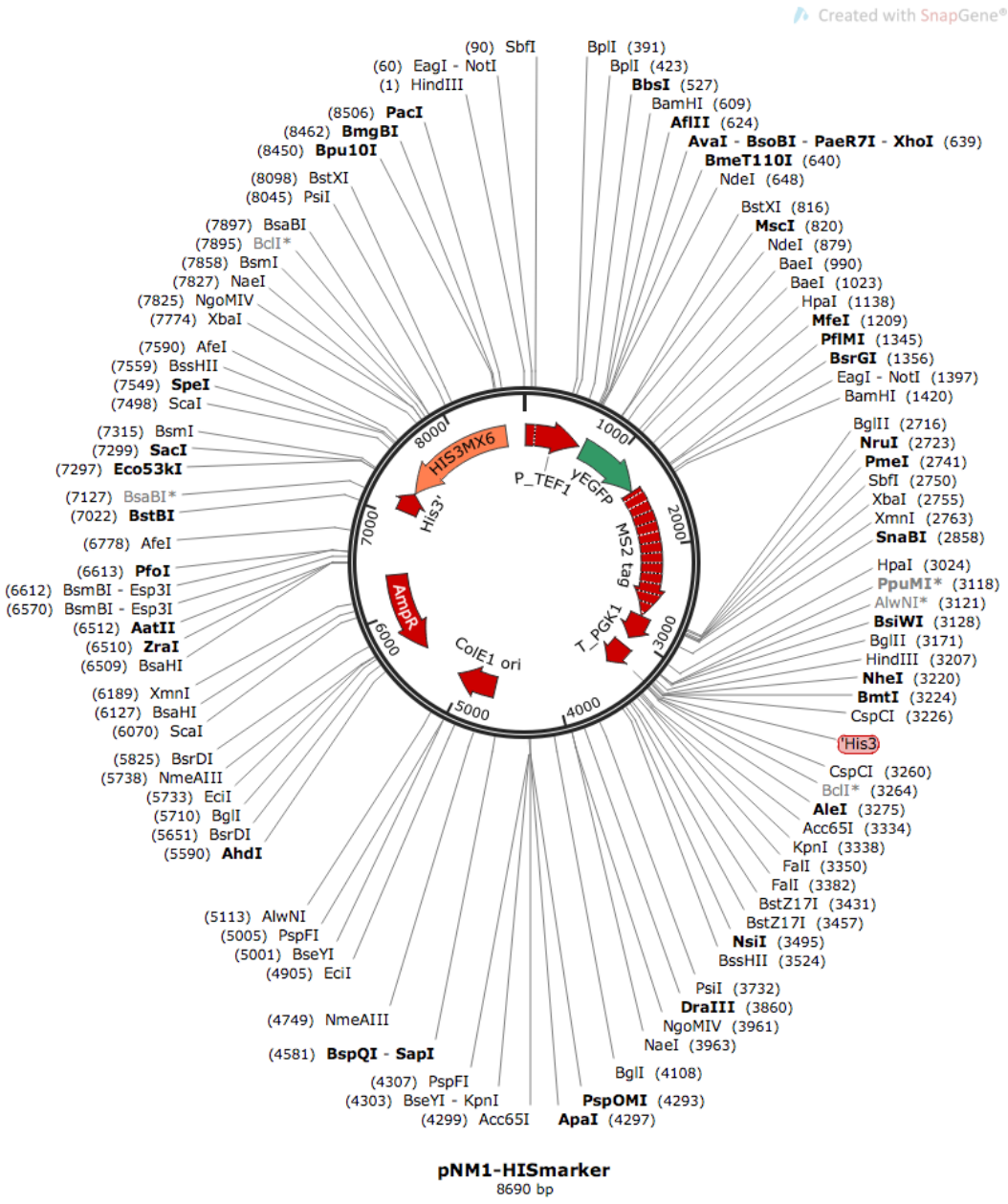

10.2. Gating analysis excludes the influence of cell aggregates on intrinsic noise estimation

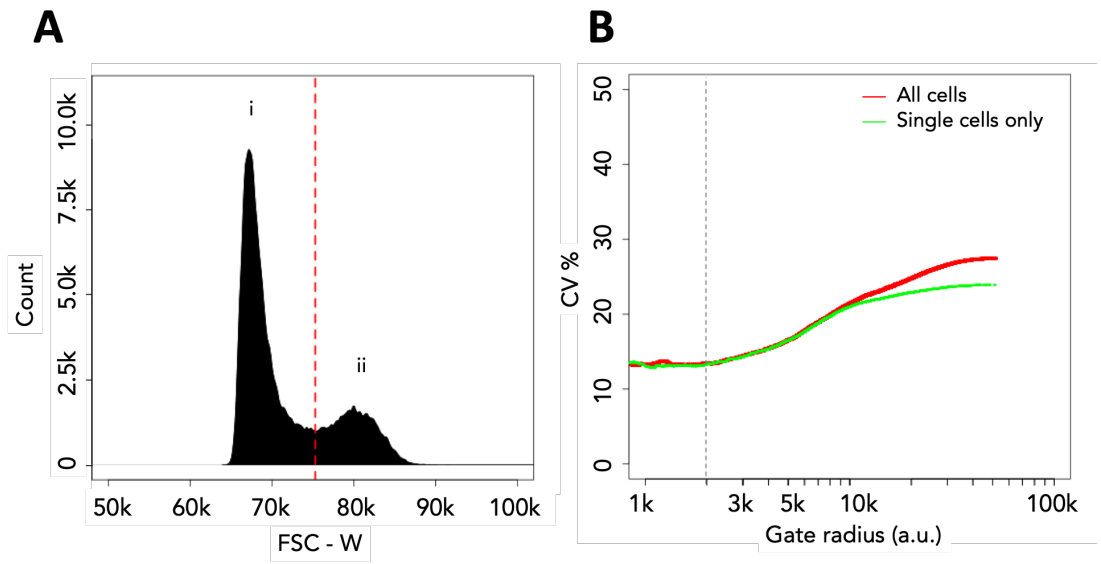

Newman analysis largely excludes the influence of aggregates on estimated intrinsic noise **A:** FSC-W is a common means of distinguishing single cells (i) from aggregates (ii). **B:** Newman analysis was performed including all cells (red curve) and only single cells (green curve), largely excluding the influence of aggregates in the estimated intrinsic noise.

10.3. CV versus gate radius plots for 10 generation old analysis

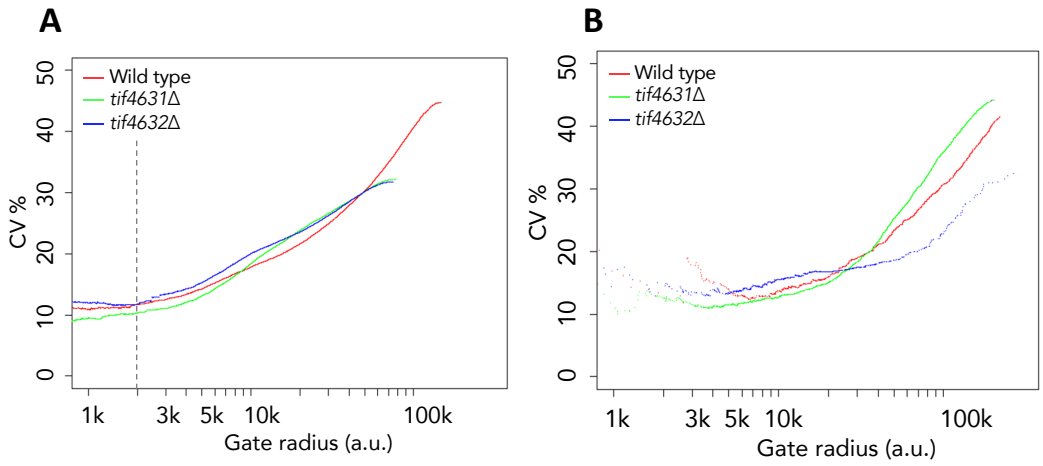

CV versus gate radius – biological repeat 1. A: analysis of young cells. **B:** analysis of 10 generation old cells.

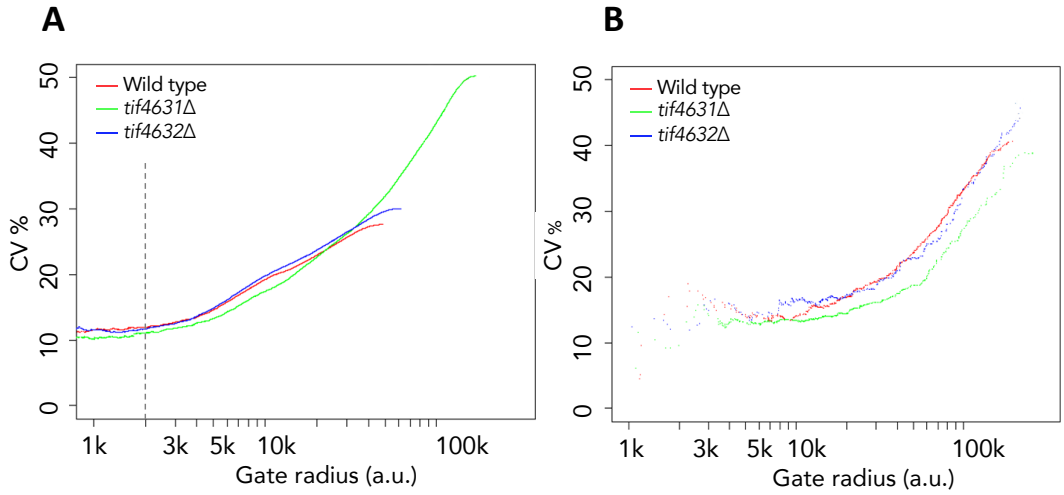

CV versus gate radius – biological repeat 2. A: analysis of young cells. **B:** analysis of 10 generation old cells.

10.4. Summary of genomic yEGFP expression data of 10 generation old analysis (3 biological repeats)

	YOUNG			10 GEN OLD		
	WT	***tif4631Δ***	***tif4632Δ***	**WT**	***tif4631Δ***	***tif4632Δ***
%CV average	12.0	11.0	12.1	14.1	12.6	14.6
%CV St. Dev.	0.4	0.8	0.7	0.7	0.6	0.9
yEGFP average	1205	1408	1093	2738	3038	2303
yEGFP St. Dev	139	154	45	863	781	590
Cell Number average	1289	1331	1385	159	308	159
Cell Number St. Dev	337	398	282	35	138	52

10.5. CV versus gate radius plots of 15 generation old analysis

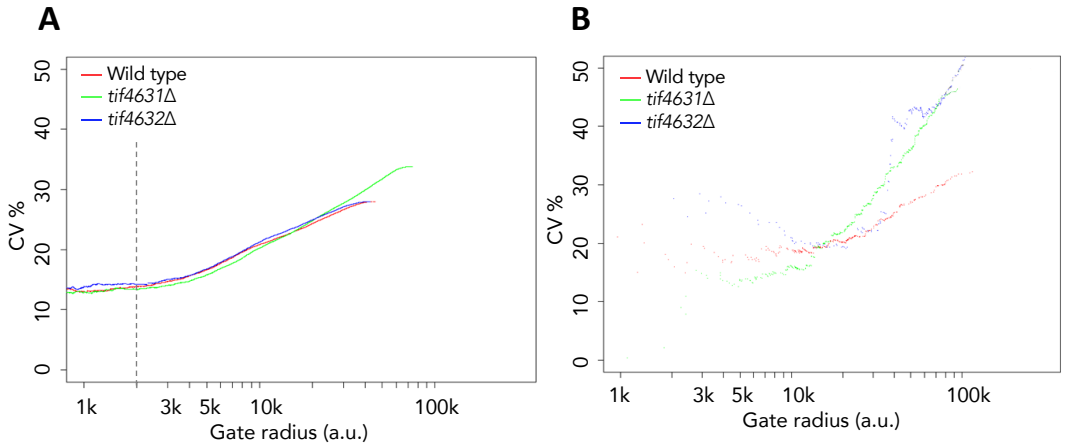

CV versus gate radius – biological repeat 1. A: analysis of young cells. **B:** analysis of 15 generation old cells.

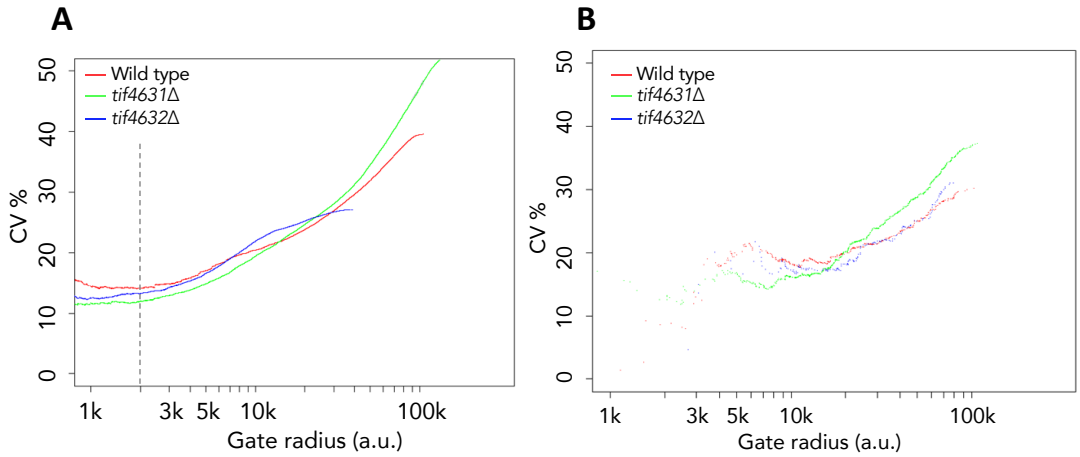

CV versus gate radius – biological repeat 2. A: analysis of young cells. **B:** analysis of 15 generation old cells.

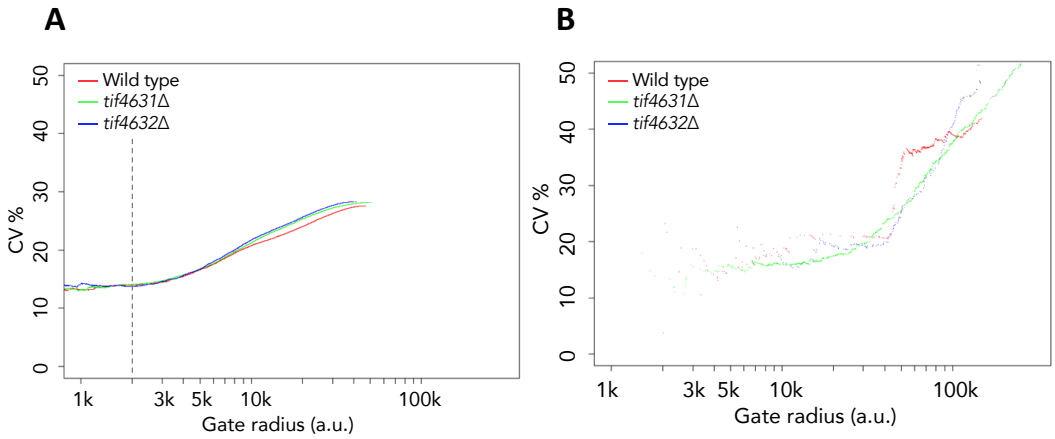

CV versus gate radius – biological repeat 1. A: analysis of young cells. **B:** analysis of 15 generation old cells.

10.6. Summary of genomic yEGFP expression data of 15 generation old analysis (4 biological repeats)

	YOUNG			15 GEN OLD		
	WT	***tif4631Δ***	***tif4632Δ***	**WT**	***tif4631Δ***	***tif4632Δ***
%CV average	13.8	12.9	13.5	19.3	16.1	19.6
%CV St. Dev.	0.3	0.8	0.6	1.6	0.6	1.6
yEGFP average	926	1103	913	2059	3049	2214
yEGFP St. Dev	68	105	9	653	448	1040
Cell number average	1682	1588	1830	146	135	90
Cell number St. Dev	387	318	225	43	26	31

10.7. R code for analysis of young population data

```
###
rm(list=ls(all=TRUE))
graphics.off()
gc()

###
library(flowCore)
library(flowViz)
library(flowDensity)
library(ggplot2)
library(beepr)

###
fs <- read.flowSet(pattern='.fcs')
sampleNames(fs)
colnames(fs)
filename <- substr(sampleNames(fs),1,nchar(sampleNames(fs))-8)
GFPset <- 'B488-530/30-A'

###
xyplot(`SSC-A`~`FSC-A`,data=fs[[1]],main=sampleNames(fs)[1],smooth=FALSE,pch=20)

###
#-fs[[1]]
data1 <- fs[[1]]
#-data1
time.value <- exprs(data1)['Time']
time.post <- which(exprs(data1)['Time'] > 100 & exprs(data1)['Time'] < (max(time.value)-20))
fs.time <- data1[time.post]
plot(data1,c('FSC-A','SSC-A'),main=sampleNames(fs)[1],ylim=c(0,200000),col='red',smooth=FALSE)
par(new=TRUE)
plot(fs.time,c('FSC-A','SSC-
A'),main=sampleNames(fs)[1],ylim=c(0,200000),col='lightgreen',smooth=FALSE)
#=fs.time

############################################################ trim FSC-SSC data
#-fs.time
data2 <- fs.time
#-data2
max.FSCremove = 2.5 #in %, that will be removed
min.FSCremove = 2.5 #in %, that will be removed
max.SSCremove = 2.5 #in %, that will be removed
```

```
min.SSCremove = 2.5 #in %, that will be removed
fsca.value <- exprs(data2)[,'FSC-A']
decrease.post<- order(fsca.value,decreasing=TRUE)
fsca.mid90post <- decrease.post[(nrow(data2)*(max.FSCremove/100)+1):(nrow(data2)*(1-min.FSCremove/100))]
ssca.value <- exprs(data2)[,'SSC-A']
decrease.post <- order(ssca.value,decreasing=TRUE)
ssca.mid90post <- decrease.post[(nrow(data2)*(max.SSCremove/100)+1):(nrow(data2)*(1-min.SSCremove/100))]
combine.mid90post <- intersect(fsca.mid90post,ssca.mid90post)
fs.mid90 <- data2[combine.mid90post]
total.removed <- (1-nrow(fs.mid90)/nrow(data2))*100
plot(data2,c('FSC-A','SSC-A'),main=sampleNames(fs)[1],ylim=c(0,200000),col='red',smooth=FALSE)
par(new=TRUE)
plot(fs.mid90,c('FSC-A','SSC-A'),main=sampleNames(fs)[1],ylim=c(0,200000),col='lightgreen',smooth=FALSE)
text(100000,190000,sprintf('max.FSC: %1.1f%%, min.FSC: %1.1f%%\nmax.SSC: %1.1f%%, min.SSC: %1.1f%%\nTotal: %1.1f%%',-max.FSCremove,-min.FSCremove,-max.SSCremove,-min.SSCremove,-total.removed),col='blue',cex=1)
#=fs.mid90

###
#-fs.mid90
data3 <- fs.mid90
#-data3
df <- data.frame(exprs(data3)[,'FSC-A'],exprs(data3)[,'SSC-A'])
p <- ggplot(df, aes(x=exprs(data3)[,'FSC-A'], y=exprs(data3)[,'SSC-A'])) +
   geom_point(alpha=0.2,size=0.1) +
   geom_density_2d(size=0.5,colour='red')
gb <- ggplot_build(p)
min <- max(gb$data[[2]][,4])
min1 <- which(gb$data[[2]][,4] == min-1)
center.x <- mean(gb$data[[2]][min1,2])
center.y <- mean(gb$data[[2]][min1,3])
plot(data3,c('FSC-A','SSC-A'),main=sampleNames(fs)[1],smooth=T)
points(gb$data[[2]][,2],gb$data[[2]][,3],pch='.',cex=1.5,col='yellow')
points(center.x,center.y,col='red',pch='.',cex=3)
text(35000,250000,sprintf("center.x= %1.2f\ncenter.y= %1.2f", center.x,center.y),col='red',cex=1)
interval <- 1
#=fs.mid90, center.x, center.y

###
#-fs.mid90, center.x, center.y
data4 <- fs.mid90
```

```
#-data4
cell.list <- matrix(1,nrow(data4),8,dimnames=list(c(), c('No.k', 'distance','GFP','FSC-axis','SSC-axis','center.x','center.y','interval')))
FSC <- seq(from = 1, to = nrow(data4), by = 1)
SSC <- seq(from = 1, to = nrow(data4), by = 1)
GFP <- seq(from = 1, to = nrow(data4), by = 1)
r <- seq(from = 1, to = nrow(data4), by = 1)
for (k in 1:nrow(data4)){
 FSC[k] <- exprs(data4)[,'FSC-A'][k]
 SSC[k] <- exprs(data4)[,'SSC-A'][k]
 GFP[k] <- exprs(data4)[,GFPset][k]
 r[k] <- sqrt((FSC[k]-center.x)^2+(SSC[k]-center.y)^2)
 cell.list[k,1] <- k
 cell.list[k,2] <- r[k]
 cell.list[k,3] <- GFP[k]
 cell.list[k,4] <- FSC[k]
 cell.list[k,5] <- SSC[k]
 cat(floor(k/nrow(data4)*100),'%','|||')
 if ((k)%%2==0){
   cat('\f')
 }
}
#write.csv(cell.list,file = 'cell-list.csv',row.names = FALSE)
#=cell.list
#-cell.list
decrease.post<- order(cell.list[,2],decreasing=FALSE)
decrease.post[1:10]
cell.list[decrease.post[1:10],]
order.list <- cell.list[decrease.post,]
order.list[,6] <- center.x
order.list[,7] <- center.y
order.list[,8] <- interval
#write.csv(order.list,file = 'order-list.csv',row.names = FALSE)
#=order.list

### trim GFP data
#-order.list
data5 <- order.list
#-data5
trimGFP.max = 0.5 #in %, that will be removed
trimGFP.min = 0.5 #in %, that will be removed
orderGFP.post <- order(data5[,3],decreasing=FALSE)
trimGFP.post <- orderGFP.post[((nrow(data5)*(trimGFP.min/100))+1):(nrow(data5)*(1-trimGFP.max/100))]
```

```
trimGFP.list <- data5[trimGFP.post,]
#=trimGFP.list
#-trimGFP.list
distance.post<- order(trimGFP.list[,2],decreasing=FALSE)
trimGFP.list <- trimGFP.list[distance.post,]
plot(density(na.omit(log10(trimGFP.list[,3]))),adjust=0.6),xlim=c(0,6),ylim=c(0,4),col='green',xlab='GFP
intensity')
write.csv(trimGFP.list,file=paste('trimGFP=',filename,'.csv',sep=''),row.names = FALSE)
###
trimGFP.list <- read.csv(file = paste("trimGFP=", filename, ".csv", sep = ""), header = TRUE)
#=trimGFP.list

###
#-trimGFP.list
data6 <- trimGFP.list
#-data6
table <- matrix(1,(nrow(data6)-1),10,dimnames=list(c(), c('cell number', 'max distance','GFP
mean','cv%','Fano factor','max FSC','min FSC','max SSC','min SSC','min distance')))
for (t in 1:(nrow(data6)-1)){
 cv <- (sd(data6[1:(t+1),3])/mean(data6[1:(t+1),3]))*100
 Fano <- (sd(data6[1:(t+1),3])^2)/mean(data6[1:(t+1),3])
 table[t,1] <- t+1
 table[t,2] <- max(data6[1:(t+1),2])
 table[t,3] <- mean(data6[1:(t+1),3])
 table[t,4] <- cv
 table[t,5] <- Fano
 table[t,6] <- max(data6[1:(t+1),4])
 table[t,7] <- min(data6[1:(t+1),4])
 table[t,8] <- max(data6[1:(t+1),5])
 table[t,9] <- min(data6[1:(t+1),5])
 table[t,10] <- min(data6[1:(t+1),2])
 cat(floor(t/(nrow(data6)-1)*100),'%','|||')
 if ((t+1)%%2==0){
  cat('\f')
 }
}
write.csv(table,file=paste('table=',filename,'.csv',sep=''),row.names = FALSE)
#=table
plot(table[,2],table[,4],main=sampleNames(fs)[1],col='red',pch='.',cex=5,
   xlab='Gate radius (a.u.)',ylab='CV%',
   xlim=c(1000,100000),ylim=c(0,50),log='x',xaxt='n',
   cex.axis=1.5,font=2,cex.lab=1.5,font.lab=2,
   las=1)
axis(1,at=c(1000,2000,3000,4000,5000,6000,7000,8000,9000,10000,100000),
```

```
    labels=c('1k','','','','5k','','','','','10k','100k'),
    cex.axis=1.5,font=2)
axis(1,at=c(3000,5000,10000),
    labels=c('3k','5k','10k'),
    cex.axis=1.5,font=2)
axis(1,at=c(seq(20000,100000,10000)),
    labels=FALSE)
```

10.8. R code for analysis of old population data

```
###
rm(list=ls(all=TRUE))
graphics.off()
gc()

###
library(flowCore)
library(flowViz)
library(flowDensity)
library(ggplot2)
library(ggExtra)
library(beepr)

###
fs <- read.flowSet(pattern='.fcs')
sampleNames(fs)
colnames(fs)
filename <- substr(sampleNames(fs),1,nchar(sampleNames(fs))-8)
GFPset <- 'B488-530/30-A'
Cy3set <- 'YG561-586/15-A'

###
xyplot(`SSC-A`~`FSC-A`,data=fs[[1]],main=sampleNames(fs)[1],smooth=FALSE,pch=20)

###
#-fs[[1]]
data1 <- fs[[1]]
#-data1
time.value <- exprs(data1)[,'Time']
length(time.value)
time.post <- which(exprs(data1)[,'Time'] > 100 & exprs(data1)[,'Time'] < (max(time.value)-20))
length(time.post)
fs.time <- data1[time.post]
nrow(fs.time)
plot(data1,c('FSC-A','SSC-A'),main=sampleNames(fs)[1],ylim=c(0,200000),col='red',smooth=FALSE)
par(new=TRUE)
plot(fs.time,c('FSC-A','SSC-
A'),main=sampleNames(fs)[1],ylim=c(0,200000),col='lightgreen',smooth=FALSE)
#=fs.time

### remove 5% of FSC and SSC
```

```
#-fs.time
data2 <- fs.time
#-data2
max.FSCremove = 0.25 #in %, that will be removed
min.FSCremove = 3.0 #in %, that will be removed
max.SSCremove = 0.25 #in %, that will be removed
min.SSCremove = 3.0 #in %, that will be removed
fsca.value <- exprs(data2)[,'FSC-A']
decrease.post<- order(fsca.value,decreasing=TRUE)
fsca.mid90post <- decrease.post[(nrow(data2)*(max.FSCremove/100)+1):(nrow(data2)*(1-
min.FSCremove/100))]
length(fsca.mid90post)
ssca.value <- exprs(data2)[,'SSC-A']
decrease.post <- order(ssca.value,decreasing=TRUE)
ssca.mid90post <- decrease.post[(nrow(data2)*(max.SSCremove/100)+1):(nrow(data2)*(1-
min.SSCremove/100))]
length(ssca.mid90post)
combine.mid90post <- intersect(fsca.mid90post,ssca.mid90post)
length(combine.mid90post)
fs.mid90 <- data2[combine.mid90post]
total.removed <- (1-nrow(fs.mid90)/nrow(data2))*100
plot(data2,c('FSC-A','SSC-A'),main=sampleNames(fs)[1],ylim=c(0,200000),col='red',smooth=FALSE)
par(new=TRUE)
plot(fs.mid90,c('FSC-A','SSC-
A'),main=sampleNames(fs)[1],ylim=c(0,200000),col='lightgreen',smooth=FALSE)
text(100000,190000,sprintf('max.FSC: %1.1f%%, min.FSC: %1.1f%%\nmax.SSC: %1.1f%%, min.SSC:
%1.1f%%\nTotal: %1.1f%%',-max.FSCremove,-min.FSCremove,-max.SSCremove,-min.SSCremove,-
total.removed),col='blue',cex=1)
xyplot(`SSC-A`~`FSC-A`,data=fs.mid90,main=sampleNames(fs)[1],smooth=FALSE,pch=20)
text(100000,160000,sprintf('max.FSC: %1.1f%%, min.FSC: %1.1f%%\nmax.SSC: %1.1f%%, min.SSC:
%1.1f%%\nTotal: %1.1f%%',-max.FSCremove,-min.FSCremove,-max.SSCremove,-min.SSCremove,-
total.removed),col='blue',cex=1)
#=fs.mid90

###
#-fs.mid90
data22 <- fs.mid90
#the next line need Cy3 channel's name! double check it!
fs.mid90logCy3 <- transform(data22,log.Cy3=log10(`YG561-586/15-A`))
red.post <- which(exprs(fs.mid90logCy3)[,'log.Cy3'] > 1)
fs.mid90logCy3 <- fs.mid90logCy3[red.post]
#density.gate <- deGate(fs.mid90logCy3, channel='log.Cy3', graphs=TRUE, adjust.dens=0.6)
density.gate <- 3
text(4.6,0.8,sprintf('line: %1.3f',density.gate),col='blue',cex=1.5)
```

```
oldcell.post <- which(log10(exprs(data22[,Cy3set])) > density.gate)
percent <- length(oldcell.post)/nrow(data22)*100
fs.mid90old <- data22[oldcell.post]
plot(density(na.omit(log10(exprs(fs.mid90old[,Cy3set])))),adjust=0.6),xlim=c(0,6),ylim=c(0,5),col='darkred')
plot(density(na.omit(log10(exprs(fs.mid90old[,GFPset])))),adjust=0.6),xlim=c(0,6),ylim=c(0,5),col='darkgreen')
#
x1 <- log10(exprs(data22[,Cy3set]))
y1 <- log10(exprs(data22[,GFPset]))
df <- data.frame(x1,y1)
p1 <- ggplot(df, aes(x=x1,y=y1)) +
    geom_point(shape=20, size=1, alpha=0.05) +
    geom_vline(xintercept=density.gate, col='blue',lty=2,lwd=1) +
    xlim(1,6) + ylim(1,4) +
    xlab('log_Cy3') + ylab('log_GFP') +
    annotate('text',x=Inf,y=Inf,label=sprintf('old                                                                cells: %1.1f%%',percent),hjust=1,vjust=1,colour='red',size=6)
ggMarginal(p1, type=c("density"), col='green', size=5, xparams=list(col='red'))
#
x2 <- log10(exprs(fs.mid90old[,Cy3set]))
y2 <- log10(exprs(fs.mid90old[,GFPset]))
df <- data.frame(x2,y2)
p2 <- ggplot(df, aes(x=x2,y=y2)) +
    geom_point(shape=20, size=1, alpha=0.05) +
    xlim(1,6) + ylim(1,4) +
    xlab('log_Cy3') + ylab('log_GFP')
ggMarginal(p2, type=c("density"), col='green', size=5, xparams=list(col='red'))
#
plot(data22,c('FSC-A','SSC-A'),main=sampleNames(fs)[1],ylim=c(0,200000),smooth=FALSE,col='darkgray')
points(exprs(fs.mid90old)[,c('FSC-A','SSC-A')],pch='.',col='red',cex=1)
text(39000,195000,sprintf('old cells: %1.1f%%',percent),col='red',cex=1)
#=fs.mid90old

###
#-fs.mid90old
data3 <- fs.mid90old
#-data3
df <- data.frame(exprs(data3)['FSC-A'],exprs(data3)['SSC-A'])
p <- ggplot(df, aes(x=exprs(data3)['FSC-A'], y=exprs(data3)['SSC-A'])) +
 geom_point(alpha=0.2,size=0.1) +
 geom_density_2d(size=0.5,colour='red')
gb <- ggplot_build(p)
```

```
min <- max(gb$data[[2]][,4])-1
#if the selected circle is wrong, min number needs to -1 for adjusting
min1 <- which(gb$data[[2]][,4] == min)
center.x <- mean(gb$data[[2]][min1,2])
center.y <- mean(gb$data[[2]][min1,3])
plot(fs[[1]],c('FSC-A','SSC-A'),main=sampleNames(fs)[1],xlim=c(0,250000),ylim=c(0,200000),smooth=T)
points(gb$data[[2]][,2],gb$data[[2]][,3],pch='.',cex=1.5,col='yellow')
points(center.x,center.y,col='red',pch='.',cex=3)
text(50000,190000,sprintf("center.x= %1.2f\ncenter.y= %1.2f", center.x,center.y),col='red',cex=1)
interval <- 1
#=fs.mid90old, center.x, center.y

###
#-fs.mid90old, center.x, center.y
data4 <- fs.mid90old


#-data4
cell.list <- matrix(1,nrow(data4),8,dimnames=list(c(), c('No.k', 'distance','GFP','FSC-axis','SSC-
axis','center.x','center.y','interval')))
FSC <- seq(from = 1, to = nrow(data4), by = 1)
SSC <- seq(from = 1, to = nrow(data4), by = 1)
GFP <- seq(from = 1, to = nrow(data4), by = 1)
r <- seq(from = 1, to = nrow(data4), by = 1)
nrow(data4)
for (k in 1:nrow(data4)){
 FSC[k] <- exprs(data4)[,'FSC-A'][k]
 SSC[k] <- exprs(data4)[,'SSC-A'][k]
 GFP[k] <- exprs(data4)[,GFPset][k]
 r[k] <- sqrt((FSC[k]-center.x)^2+(SSC[k]-center.y)^2)
 cell.list[k,1] <- k
 cell.list[k,2] <- r[k]
 cell.list[k,3] <- GFP[k]
 cell.list[k,4] <- FSC[k]
 cell.list[k,5] <- SSC[k]
 cat(floor(k/nrow(data4)*100),'%','|||')
 if ((k)%%2==0){
  cat('\f')
 }
}
#write.csv(cell.list,file='cell-list.csv',row.names=FALSE)
#=cell.list
#-cell.list
decrease.post<- order(cell.list[,2],decreasing=FALSE)
```

```
order.list <- cell.list[decrease.post,]
order.list[,6] <- center.x
order.list[,7] <- center.y
order.list[,8] <- interval
#write.csv(order.list,file='order-list.csv',row.names=FALSE)
#=order.list

### remove top and bottom total 5% of the GFP data
#-order.list
data5 <- order.list

#-data5
trimGFP.max = 1.5 #in %, that will be removed
trimGFP.min = 1.5 #in %, that will be removed
orderGFP.post <- order(data5[,3],decreasing=FALSE)
length(orderGFP.post)
trimGFP.post <- orderGFP.post[((nrow(data5)*(trimGFP.min/100))+1):(nrow(data5)*(1-
trimGFP.max/100))]
length(trimGFP.post)
trimGFP.list <- data5[trimGFP.post,]
nrow(trimGFP.list)
#=trimGFP.list
#-trimGFP.list;
distance.post<- order(trimGFP.list[,2],decreasing=FALSE)
trimGFP.list <- trimGFP.list[distance.post,]
plot(density(na.omit(log10(trimGFP.list[,3]))),adjust=0.3),col='green',lwd=2)
write.csv(trimGFP.list,file=paste('trimGFP=',filename,'.csv',sep=''),row.names = FALSE)
#######
##########################################################################
################################################
#######
trimGFP.list <- read.csv(file = paste("trimGFP=", filename, ".csv", sep = ""), header = TRUE)
#=trimGFP.listtrimGFP.list
######
###
#-trimGFP.list
data6 <- trimGFP.list
#-data6
table <- matrix(1,(nrow(data6)-1),10,dimnames=list(c(), c('cell number', 'max distance','GFP
mean','cv%','Fano factor','max FSC','min FSC','max SSC','min SSC','min distance')))
for (t in 1:(nrow(data6)-1)){
 cv <- (sd(data6[1:(t+1),3])/mean(data6[1:(t+1),3]))*100
 Fano <- (sd(data6[1:(t+1),3])^2)/mean(data6[1:(t+1),3])
 table[t,1] <- t+1
```

```
 table[t,2] <- max(data6[1:(t+1),2])
 table[t,3] <- mean(data6[1:(t+1),3])
 table[t,4] <- cv
 table[t,5] <- Fano
 table[t,6] <- max(data6[1:(t+1),4])
 table[t,7] <- min(data6[1:(t+1),4])
 table[t,8] <- max(data6[1:(t+1),5])
 table[t,9] <- min(data6[1:(t+1),5])
 table[t,10] <- min(data6[1:(t+1),2])
 cat(floor(t/(nrow(data6)-1)*100),'%','|||')
 if ((t+1)%%2==0){
  cat('\f')
 }
}
write.csv(table,file=paste('table=',filename,'.csv',sep=''),row.names = FALSE)
#=table

plot(table[,2],table[,4],main=sampleNames(fs)[1],col='green',pch='.',cex=5,
   xlab='Gate radius (a.u.)',ylab='CV%',
   xlim=c(1000,100000),ylim=c(0,50),log='x',xaxt='n',
   cex.axis=1.5,font=2,cex.lab=1.5,font.lab=2,
   las=1)
axis(1,at=c(1000,2000,3000,4000,5000,6000,7000,8000,9000,10000,100000),
   labels=c('1k','','','','5k','','','','','10k','100k'),
   cex.axis=1.5,font=2)
axis(1,at=c(3000,5000,10000),
   labels=c('3k','5k','10k'),
   cex.axis=1.5,font=2)
axis(1,at=c(seq(20000,100000,10000)),
   labels=FALSE)
beep(1)
```